Title

Morphological diversification and functional maturation of human astrocytes in glia-enriched cortical organoid transplanted in mouse brain

Authors

Wang, Meiyan
Zhang, Lei
Novak, Sammy Weiser
et al.

Publication Date

2024-02-28

DOI

10.1038/s41587-024-02157-8

Morphological diversification and functional maturation of human astrocytes in glia-enriched cortical organoids transplanted in the mouse brain

Meiyan Wang[1,#], Lei Zhang[1,#], Sammy Weiser Novak[2], Jingting Yu[3], Iryna S. Gallina[1], Lynne L. Xu[1], Christina K. Lim[1,5], Sarah Fernandes[1,5], Maxim N. Shokhirev[3], April E. Williams[3], Monisha D. Saxena[1], Shashank Coorapati[1], Sarah L. Parylak[1], Cristian Quintero[4], Elsa Molina[4], Leonardo R. Andrade[2], Uri Manor[2,6] and Fred H. Gage[1,*]

1. Laboratory of Genetics, The Salk Institute for Biological Studies, La Jolla, California, 92037, USA
2. Waitt Advanced Biophotonics Core, The Salk Institute for Biological Studies, La Jolla, California, 92037, USA
3. Integrative Genomics and Bioinformatics Core, The Salk Institute for Biological Studies, La Jolla, California, 92037, USA
4. Next Generation Sequencing Core, The Salk Institute for Biological Studies, La Jolla, California, 92037, USA
5. Division of Biological Sciences, University of California, San Diego, La Jolla, California, 92093, USA
6. Present address: Division of Biological Sciences, University of California, San Diego, La Jolla, California, 92093, USA

# These authors contributed equally

* Correspondence: gage@salk.edu

Abstract

Astrocytes, the most abundant glial cell type in the brain, are underrepresented in traditional cortical organoid models due to the delayed onset of cortical gliogenesis. Here, we introduce a novel glia-enriched cortical organoid model that exhibits accelerated astrogliogenesis. We demonstrated that induction of a gliogenic switch in a subset of progenitors enabled rapid derivation of astroglial cells, which account for 25-31% of the cell population within eight to ten weeks of differentiation. Intracerebral transplantation of these organoids reliably generated a diverse repertoire of cortical neurons and anatomical subclasses of human astrocytes. Spatial transcriptome profiling identified layer-specific expression patterns among distinct subclasses of astrocytes within the organoid transplants. Using an *in vivo* acute neuroinflammation model, we identified a subpopulation of astrocytes that rapidly activates proinflammatory pathways upon cytokine stimulation. Additionally, we demonstrated that CD38

signaling plays a crucial role in mediating metabolic and mitochondrial stress in reactive astrocytes. This model provides a robust platform for investigating human astrocyte function.

Main text

Astrocytes comprise the most abundant glial cell type in the human brain, and their dysfunction has been implicated in numerous neurological disorders [1]. However, our ability to elucidate the roles of astrocytes in brain development and in the pathogenesis of brain disorders has been limited by the scarcity of accessible human astrocytes in a brain environment. Brain organoid models have emerged as valuable tools for investigating human brain development and disorders, as they exhibit self-organized properties that recapitulate certain aspects of the developing human brain [2-6]. Nonetheless, current cortical brain organoid systems have limitations in efficiently generating astrocytes [7,8], mainly due to the extended time required for the progenitor cells to acquire glial competency [9]. In human cortical organoid systems, astrogliogenesis begins gradually at three months of differentiation and undergoes a maturation process lasting over a year [7]. Attempts to accelerate astrocyte differentiation from human induced pluripotent stem cells (hiPSCs) have shown promise either by transiently overexpressing a critical gliogenic factor [10,11] or by triggering a gliogenic switch with a specific set of patterning factors [12,13]. However, it remains unclear whether these patterning factors can be successfully applied to a cortical organoid patterning paradigm to generate glia-enriched cortical organoids.

Cells or organoids cultured *in vitro* also lack the blood circulation and the cortical organization of the brain. The brain is a highly vascularized organ that is connected with the systemic circulation. Astrocyte projections form glia limitans surrounding the vessels, regulating the communication between brain and circulation, and maintaining brain homeostasis [14,15]. Transplantation of human brain organoids into rodent brains enables the successful survival, integration, and formation of functional circuits of the human brain organoids *in vivo* [16-22].

In this study, we present a glia-enriched cortical organoid model that facilitates accelerated astrogliogenesis. By triggering a gliogenic switch in 28-33% of the cells in the organoids at three weeks of differentiation, we achieved efficient derivation of astroglia comprising 25-31% of the cell population by eight to ten weeks of differentiation. To investigate astrocyte function in a brain environment, we employed an intracerebral transplantation method [16] that yielded highly vascularized *in vivo* brain organoids. The organoid transplants displayed robust integration into the host brain and developed anatomically defined morphological subclasses of human astrocytes. Spatial genomics further revealed layer-specific molecular signatures among different subclasses of human astrocytes. Moreover, we observed the formation of perivascular astrocytic endfeet ensheathing the vessels within the transplants. Using single nucleus RNA-sequencing (snRNA-seq), we found advanced maturation of astrocytes in our organoid transplants compared to cortical organoid transplants. Additionally, we showed that differentially expressed genes (DEGs) associated with

acute reactivity exhibited significant heterogeneity across astrocyte subpopulations in an *in vivo* model of acute neuroinflammation. Notably, we demonstrated that the metabolic and mitochondrial stresses in reactive astrocytes were mediated through CD38 signaling and that treatment with a potent CD38 inhibitor effectively alleviated a wide range of stresses induced by inflammation in astrocytes.

Rapid astrogliogenesis in glia-enriched cortical organoids

Astrocytes, like neurons and oligodendrocytes, originate from the radial glial cells in the subventricular zone (SVZ). Because astrogliogenesis occurs late during development [9], most brain organoid models do not develop astrocytes until a very late stage. We hypothesized that triggering an early gliogenic switch in a subset of progenitors during neuroectoderm specification would enable rapid derivation of glial cells in a human cortical brain organoid model (Fig.1a and Extended Data Fig.1a). To induce an early gliogenic switch, we supplemented the neuroectoderm induction media with the previously reported gliogenic agent platelet-derived growth factor (PDGF-AA) and cultured the organoids in astrocyte medium [12,13] (Fig.1a). Organoids cultured under the gliogenic condition demonstrated robust upregulation of gliogenic factor NFIA at three weeks of differentiation (Fig.1b,c and Extended Data Fig.1b), indicating early glial patterning in a subset of progenitor cells, whereas forebrain organoids cultured under published methods [23,24] had almost no detectable NFIA expression at the same time point (Fig.1b,c). As early as eight weeks of differentiation, glia-enriched cortical organoids had substantially greater gliogenesis compared to the forebrain organoids, supported by the upregulation of astrocyte markers GFAP and HepaCAM (Fig.1d-g and Extended Data Fig.1c). In addition to astrocytes, robust neurogenesis was observed at eight weeks of differentiation (Extended Data Fig.1d). Compared to organoids cultured in a serum-free condition, glia-enriched cortical organoids cultured in differentiation media containing fetal bovine serum (FBS) displayed the most efficient derivation of astrocytes at three months of differentiation (Extended Data Fig.1e,f).

To identify cell-type diversity in glia-enriched cortical organoids, we carried out snRNA-seq on nuclei isolated from 10-week-old organoids generated from two pluripotent stem cell lines. We first applied uniform manifold approximation and projection (UMAP) dimensionality reduction and Louvain clustering to the snRNA-seq datasets, identifying multiple neuronal and glial subpopulations (Fig.1h, Extended Data Fig.2a-c, Supplementary Table 1). The majority of excitatory neurons were committed to a cortical identity, characterized by the expression of cortical neuronal markers (e.g. CTIP2, CUX2, and SATB2) (Extended Data Fig.1d and 2b-c). Astroglia comprised 25-31% of the total population; 5-8% of these were proliferating progenitor cells and 20-23% were astrocytes (Extended Data Fig. 2a-c). To contextualize early neurogenesis and gliogenesis in a systems-level framework, we applied a single-cell weighted gene coexpression network

analysis (WGCNA) [25,26]. By computing the average expression of 50 neighboring cells from each major cell type, we constructed co-expression networks for the astrocytes from the snRNA-seq dataset and identified two astrocyte gene modules (Fig.1i,j, Extended Data Fig.2d,e, Supplementary Table 2). The hub genes of astrocyte module M12 consisted of genes that function in cell-cell adhesion (TJP1, ID3, and FGFR1), and the hub genes of module M14 consisted of many known glial markers, including transcriptional factors ZBTB20 and GLI3 and glutamate transporter SLC1A3 (Fig.1k). Similarly, we constructed co-expression networks for the cortical excitatory neurons and identified four co-expression gene modules highly expressed in these cells (Extended Data Fig.2f-j, Supplementary Table 3). Collectively, transcriptomic analysis of 10-week-old glia-enriched cortical organoids confirmed robust neurogenesis and astrogliogenesis.

Protoplasmic astrocytes are the most abundant astrocyte subtypes in the gray matter and exhibit highly ramified processes [27]. Astrocyte morphogenesis depends on direct interaction with neuronal processes [28]. We hypothesized that our organoid model supports robust astrocyte morphogenesis. To study the morphological characteristics of astrocytes during organoid differentiation, we transduced glia-enriched cortical organoids with GFAP::GFP adeno associated virus (AAV) and carried out Sholl analysis and morphological analyses of virus-labeled astrocytes (Fig.1l-n). Astrocytes exhibited process-bearing morphology at three months of differentiation and displayed robustly increased branch complexity over time, such as an increased number of primary processes, number of branches, and total length of the processes (Fig.1l-n). Immunostaining confirmed that AAV-transduced astrocytes expressed many mature astrocyte markers, and their processes were closely associated with synapses (Extended Data Fig.3a-e). Furthermore, AAV-transduced astrocytes were capable of glutamate uptake (Extended Data Fig.3f). Taken together, these data indicate successful generation of functional astrocytes *in vitro*.

Formation of astrocyte morphological subclasses *in vivo*

To better mimic the endogenous microenvironment, we performed intracerebral transplantation of 8- to 10-week-old glia-enriched cortical organoids into a cavity made in the retrosplenial cortex of immunodeficient (NOD.Cg-*Prkdc*^{scid} *Il2rg*^{tm1Wjl}/SzJ or NSG) mice (Fig.2a). Glia-enriched cortical organoids exhibited robust integration into the lesion cavity (Fig.2b,c and Extended Data Fig.4a-d). Immunostaining confirmed that nearly all NeuN and GFAP expression in the transplants coincided with HuNuclei expression and human GFAP (hGFAP) expression, respectively (Extended Data Fig.4a,b), indicating that neurons and astrocytes in the transplants were derived nearly exclusively from the human organoids. Human astrocytes exhibit a notably intricate morphology in contrast to their rodent counterparts [29]. Stereotactic viral labeling of

astrocytes with GFAP::GFP AAV revealed that human astrocytes in the transplants differed from the host astrocytes in that the human protoplasmic astrocytes were far more elaborate and larger (Fig.2d,e). In addition, human protoplasmic astrocytes extended long processes to the vasculature whereas the rodent astrocytes formed rosette-like structures around the vasculature (Fig.2f). Collectively, these results suggest that human protoplasmic astrocytes maintain their characteristic species-specific features in the transplants.

Studies revealed intrinsic differences between human astrocytes and those of lower mammals [30,31], including anatomically defined subclasses of human astrocytes that are absent in rodents [29]. Besides the predominant protoplasmic astrocytes, at least three additional major morphological subclasses of $GFAP^+$ astrocytes have been identified in the adult human temporal lobe, including interlaminar astrocytes, fibrous astrocytes, and varicose projection astrocytes [29]. We identified primate-specific interlaminar astrocytes at the pial surface of the transplant-forming fibers that both contributed to the glial limitans at the pial surface and penetrated deeper layers of the transplants; we also observed abundant ramified protoplasmic astrocytes in cortical layers of the transplants and fibrous astrocytes in deep layers of the transplants adjacent to white matter (WM), with relatively unbranched, straight $GFAP^+$ processes (Fig.2c and Extended Data Fig.4e). Notably, the formation of morphological subclasses of astrocytes in the transplants was accompanied by differential expression of CD44 and S100B (Extended Data Fig.4f,g). To further explore the morphological subclasses of $GFAP^+$ astrocytes, we used GFAP::tdTomato lentiviral transduced organoids for transplantation. Viral labeling enabled the identification of far more astrocytic processes than immunohistochemistry for GFAP (Fig.2g). Viral labeling also revealed human- and higher-order primate-specific varicose projection astrocytes, characterized by long fibers with prominent varicosities (Fig.2g). Together, these results show that intracerebral transplantation creates a permissive environment for the specification of anatomically defined human astrocyte subclasses.

To decipher the molecular signatures of astrocytes across transplant layers, we next spatially profiled the expression of human protein-coding genes on formalin-fixed paraffin-embedded (FFPE) sections using the NanoString GeoMx human whole-transcriptome atlas (WTA; > 18,000 genes) assay[32] (Fig.2h). We first selected the regions of interest (ROIs) across different transplant layers (i.e., pial, cortex, and WM) and then performed segmentation of astrocytes within each ROI according to $SOX9^+$ staining (Fig.2i,j and Extended Data Fig.5a). Utilizing Principal Component Analysis (PCA), we observed separations in the gene expression profiles between layer-specific astrocytes (Fig.2k). Comparative transcriptomic analysis revealed that expression levels of many established astrocyte markers varied according to their specific locations (Fig.2l,m, Extended Data Fig.5b, and Supplementary Table 4-6). Pial interlaminar astrocytes demonstrated elevated expression levels of astrocyte markers such as Glial Fibrillary Acidic Protein

(GFAP), Aquaporin 4 (AQP4), and transcriptional repressors ID1 and ID3 (Fig.2l,m). Meanwhile, fibrous astrocytes within the WM displayed increased expression of Thrombospondin 4 (THBS4) and transcription factor HES2, and cortical gray matter (predominantly protoplasmic) astrocytes demonstrated elevated expression of Solute Carrier Family 1 Member 2 (SLC1A2), ATPase Na^+/K^+ Transporting Subunit Alpha 2 (ATP1A2), Sterol Regulatory Element Binding Transcription Factor 2 (SREBF2), and Neuroglycan C (CSPG5) (Fig.2l,m). We then carried out gene set enrichment analysis (GSEA) and identified that cortical (predominantly protoplasmic) astrocytes exhibited enrichment in genes associated with steroid metabolism, cholesterol biosynthesis, neurotransmitter release cycle, and nervous system development, highlighting their close interaction with neurons (Extended Data Fig.5c). To further explore the interactions between astrocytes and neurons, we confirmed the expression of glutamate transporter EAAT2 (gene name SLC1A2) and synaptogenic proteins HEVIN (gene name SPARCL1) in human protoplasmic astrocytes by immunostaining (Extended Data Fig.6a,b). Electron microscopy (EM) revealed the presence of multi-synaptic boutons (Extended Data Fig.6c), indicating neuronal maturation in the transplants. To investigate the physical proximity of synapses and astrocytes in the transplants, we employed serial-sectioning EM and reconstructed a dendrite with spines (Extended Data Fig.6d). We observed that the astrocytic processes were surrounding the synapse (Extended Data Fig.6e), indicating a close association of human astrocytes with synapses *in vivo*. Collectively, these findings demonstrated functional diversification of astrocyte subclasses at the molecular level.

Human astrocytes form perivascular astrocytic endfeet

In the brain, astrocytes are uniquely positioned to interact with both neurons and the vasculature. We observed an extensive host vascular network and microglia infiltrating into the transplants (Extended Data Fig.6f-i). Unlike the *in vitro* astrocytes, protoplasmic astrocytes in the transplants established spatial territory (Fig.3a,b). Astrocytic processes interact with blood vessels through cap-like cytoplasmic processes called astrocytic endfeet. Specific channels and transporters, for example AQP4 and Kir4.1, are targeted to astrocyte endfeet to control water and ion homeostasis at the vessel-neuron interface [15]. Immunostaining for the water channel protein AQP4 demonstrated polarized expression at the endfeet of the human astrocytes in the transplants, in sharp contrast to the *in vitro* astrocytes (Fig.3c). This finding was further confirmed by the expression of the inward-rectifier potassium channel Kir4.1 at the perivascular astrocyte endfeet processes and of the glucose transporter Glut-1 at the astrocyte-vessel interface (Extended Data Fig.6j,k). These results provide evidence that the *in vivo* environment facilitates formation of astrocytic endfeet structure.

We next carried out EM to transplants derived from the GFP-transduced H9 hESC line to investigate the interaction between human astrocytes and host vasculature. Blood vessels were directly labeled by trans-cardiac perfusion with a fluorescent lipophilic carbocyanine dye that incorporates into endothelial cell membranes upon contact [33] (Extended Data Fig.6l). The structure of the blood vessels was well maintained when examined under scanning EM, where tight junctions and marginal folds were clearly visible between endothelial cells (Fig.3d). Glycogen granules and intermediate filament were also found in the astrocytes surrounding the vessels (Fig.3e). We next reconstructed elements of a blood vessel and perivascular astrocytes from a three-µm segment of a capillary found near the center of the transplant using serial section EM (Fig.3f,g and Supplementary Video 1). Tight junctions were visible between endothelial cells in the electron micrograph (Extended Data Fig.6m). Astrocytic processes wrapped around the vessel and apparently covered the entire surface, suggesting the formation of glia limitans surrounding the vasculature. Together, these results demonstrate the close coupling of human astrocytes to the host vasculature.

Enhanced cell maturation in engrafted organoids

To systematically investigate neuronal and glial development and maturation, we carried out snRNA-seq on five-month-old *in vitro* organoids, five-month-old transplants, six-month-old transplants, and eight-month-old transplants from two pluripotent stem cell lines (Fig.4a). We first performed batch-correction integration and UMAP dimensionality reduction, identifying subpopulations of neuronal and glial cells (Fig.4b,c, Extended Data Fig.7a-c, and Supplementary Table 7). We next leveraged a transfer learning strategy to integrate our dataset into a published atlas of postmortem prefrontal cortex samples from individuals spanning fetal, neonatal, infancy, childhood, adolescence, and adult stages of development [34], and we estimated the cell states and their developmental stages in our organoid nuclei (Extended Data Fig.7d-g). Most organoid nuclei from five-month-old organoids aligned with fetal populations of the reference dataset (Fig.4d). Notably, with transplantation and increasing organoid age, more nuclei displayed characteristics of postnatal cells (Fig.4d), in particular upper-layer (UL) excitatory neurons, with 6.1% of ULs for the five-month organoids aligned to postnatal stages, compared with 30.2% for the five-month transplants and 94.5% for the eight-month transplants (Extended Data Fig.7h).

To determine the genes involved in astrocyte development and function, we constructed co-expression networks using astrocytes from the integrated snRNA-seq data and identified an astrocyte gene module (M5) containing genes associated with glutamate transport (Fig.4e,f, Extended Data Fig.8a,b, and Supplementary Table 8). Analysis of the harmonized module score of gene module M5 in astrocytes revealed increased expression of the module genes in the transplants compared to the *in vitro* organoids

(Fig.4g). We next curated the top 50 expressed genes from the upregulated gene list in mature human astrocytes versus fetal human astrocytes as reported in Zhang et al., 2016 [30], and we identified elevated expression of the mature human astrocyte genes in the transplants compared to the *in vitro* organoids (Fig.4h,i). To further uncover glial heterogeneity and maturity, we performed pseudotime trajectory analysis using monocle 3[35] on the integrated snRNA-seq data in glia (Fig.4j). Setting progenitors as the starting time point for astrocytes, pseudotime trajectory analysis revealed more cells towards the end point of the trajectory in the transplants, progressing from glial progenitors to astrocytes (Fig.4j). Similarly, WGCNA and pseudotime analyses of immature and mature UL excitatory neurons revealed more advanced excitatory neuronal maturation *in vivo* (Extended Data Fig.8c-g and Supplementary Table 9). Collectively, these results provide evidence that transplantation facilitates organoid maturation.

To compare the cell states of our organoid transplants with previously reported cortical organoid transplants[21], we integrated snRNA-seq data from the cortical organoid transplants into our dataset and conducted a cell-type prediction analysis. The analysis confirmed a high degree of similarity in cell-type identity between our eight-month-old organoid transplants and the eight-month-old cortical organoid transplants[21] (Fig.4k,l). We then focused on examining the distribution of astrocyte nuclei ages using the age-prediction analysis. Our differentiation paradigm supported enhanced astrocyte maturation, with 75.8% of the nuclei aligned to postnatal cells over the age of 301 days, as estimated through molecular equivalence using the brain reference dataset, compared to 56.2% of nuclei in previously reported cortical organoid transplants (Fig.4m). Overall, these data suggest that our differentiation paradigm enhances astrocyte maturation.

Characterization of proinflammatory pathways in astrocytes

Reactive astrocytes are induced by CNS injuries and diseases [36], as characterized by upregulation of genes that can modulate CNS inflammation [1,37] and formation of a glial scar after CNS trauma [38]. Despite significant progress in our understanding of this pronounced transformation process, our knowledge of astrocyte reactivity has been predominantly based on rodent cells. To investigate the reactive transformation of human astrocytes *in vivo*, we performed stereotaxic injections of either saline or recombinant human tumor necrosis factor alpha (TNFα), an inflammatory cytokine known to induce reactive astrogliosis [1,37], into the transplants, and performed fluorescence activated cell sorting to purify glial cells for single-cell RNA-seq five hours post injection (Fig.5a-c, Extended Data Fig.9a,b, and Supplementary Table 10). We found that differentially expressed genes (DEGs) associated with acute reactivity exhibited significant heterogeneity across astrocyte subpopulations (Fig.5d,e and Extended Data Fig.9c,d). Following TNFα

treatment, we observed a significant expansion of cluster 2 astrocytes, which were identified by their expression of CD44, CD38, and GFAP (Fig.5c,f). These reactive astrocytes were characterized by genes that have been previously linked to proinflammatory pathways and astrocyte pathogenic activities in neurotoxicity, such as the activation of NF-κB and interferon pathways (Fig.5g and Extended Data Fig.9e). We also observed downregulation of genes involved in oxidative phosphorylation, NADH dehydrogenase complex assembly, and mitochondrial respiratory chain complex assembly in cluster 2 astrocytes following TNFα treatment (Fig.5g and Extended Data Fig.9f). Taken together, our findings indicate that there is significant reactive heterogeneity across different human astrocyte subpopulations *in vivo*.

CD38 mediates inflammation-induced stresses in astrocytes

To gain further insights into the cellular changes that occur during human astrocyte reactivity, we treated glia-enriched cortical organoids with TNFα for 24 hours and examined the inflammatory processes following the treatment (Fig.6a,b and Extended Data Fig.10a,b). Our results confirmed a rapid upregulation of pro-inflammatory cytokines, interferon signaling, and the NF-κB signaling pathway (Fig.6b and Extended Data Fig.10a,b). We also observed NF-κB nuclear translocation in astrocytes (Fig.6c). These results demonstrate that *in vitro* astrocytes can recapitulate the molecular changes *in vivo*.

Transcriptomics suggests dysregulation of metabolism and mitochondrial function in reactive astrocytes (Fig.5g and Extended Data Fig.9f). To investigate changes in NAD^+ metabolism and mitochondrial function in reactive astrocytes, we purified GFAP::tdTomato$^+$ astrocytes from *in vitro* organoids (Fig.6d and Extended Data Fig.10c). Our analysis revealed reduced NAD^+/NADH ratio (Fig.6e) and glutathione (reduced to oxidized or GSH/GSSH) ratio (Fig.6f) in astrocytes following TNFα treatment, suggesting metabolic stress and oxidative stress in reactive astrocytes. CD38 is a major regulator of NAD^+ levels and a gradual increase in CD38 has been implicated in the decline of NAD^+ with age [39]. We observed significant upregulation of CD38 in reactive astrocytes (Extended Data Fig.10d). We next investigated whether CD38 mediated the reductive metabolic stress and oxidative stress. After treating human astrocytes with TNFα and a potent CD38 inhibitor 78c, we found significantly reduced metabolic and oxidative stress (Fig.6e,f). Cellular stress and metabolic cues can cause the mitochondrial network to fragment, which then promotes mitophagy and is associated with cell death [40]. Reactive astrocytes showed significant increases in mitochondrial fragmentation, which was markedly reduced by 78c (Fig.6g,h). These results suggest a mechanism by which a major NADase CD38 mediates metabolic and mitochondrial dysregulation in reactive astrocytes.

Discussion

While brain organoid models have been useful for studying human neurodevelopment and neurological disorders, studies of astrocyte function in such models have remained limited. This is partly due to the late onset of gliogenesis in humans, which is recapitulated in cortical organoid models [7]. Prolonged culture of neural progenitor cells in media containing gliogenic factors [12,13] or repeated passaging [41,42] confers gliogenic competency but eliminates neurogenic potentials. In this study, we demonstrate that induction of a gliogenic switch by addition of a gliogenic factor PDGF-AA and astrocyte-supporting medium for three weeks successfully enables accelerated astrogliogenesis in a substantial portion of cells while retaining neurogenic potential for the majority of cells. In this context, our organoid model not only efficiently generates astrocytes in a time window comparable to previously reported 2D astrocyte differentiation protocols[10-13] but also gives rise to other brain cell types, including cortical excitatory neurons, inhibitory neurons, and OPCs (Supplementary Fig.1). Additionally, transcriptomic analysis revealed that astrocytes generated in our model exhibit enhanced maturation compared to those derived from cortical organoids [21] when transplanted into rodent cortices. Therefore, our organoid model provides an opportunity to study human astrocyte function in neurodevelopment and neurological diseases.

Human astrocytic complexity correlates with the increased functional competence of the adult human brain [29,31]. In the human brain, astrocytes display a remarkable morphological diversity according to cortical layers and form anatomically defined subclasses [29,31]. While neonatal engraftment of human glial progenitor cells has allowed the progressive expansion of human glial cells in the host brain [43-45], to the best of our knowledge, it is still limited in fully reproducing the morphological complexity observed in the human brain. Notably, our model is capable of producing hominid-specific varicose astrocytes, a feature that was not observed in previous models. Our study has also uncovered the diversification of layer-specific expression patterns in astrocytes by spatial transcriptome profiling. Pial interlaminar astrocytes within the transplants expressed many astrocyte markers, including GFAP, S100B, CD44, and AQP4, and showed increased expression of GFAP, AQP4, ID1, and ID3 compared to cortical astrocytes, resembling the expression profiles of subpial astrocytes observed in mice [46,47] and interlaminar astrocytes reported in humans [48,49]. In contrast, cortical protoplasmic astrocytes displayed an upregulation of genes involved in regulating cholesterol biosynthesis, synapse formation, and synaptic activity, while fibrous astrocytes expressed genes involved in initiation of myelination. These findings contribute to our understanding of the unique molecular processes governing the spatial organization of astrocytes within the cortical architecture. Of note, the NanoString GeoMx platform used in this study did not permit discrete identification of gene expression variations at single cell resolution. This lack of single cell resolution represents a notable

constraint in our analysis, where regions of interest, although enriched for SOX9, encompass various astrocytic types, thereby limiting our capacity to delineate transcriptional distinctions at a more refined morphological level.

Our model also provides a platform to study astrocyte function during neuroinflammation and disease progression. The previous notion of astrocyte reactivity being a uniform response to tissue damage has been challenged by accumulating evidence suggesting that astrocytes are a diverse population of cells [36,50]. Our findings show that transcriptional changes associated with acute astrocyte reactivity *in vivo* are highly heterogeneous among human astrocyte subpopulations. We also demonstrate that metabolic and mitochondrial stresses induced by inflammation can be alleviated through inhibiting cyclase/hydrolase activity of CD38, a major NADase expressed in a subset of astrocytes and upregulated in response to TNFα treatment. This model thus presents a platform to interrogate cellular function under physiological conditions that is otherwise difficult to investigate in other models and for drug discovery to treat human brain diseases.

Acknowledgments

We thank A.Mansour for providing the pCSC-CAG-GFP lentiviral labeled H9 ESC line, N. Hah for technical assistance with snRNA-seq, and R.Garg for assistance with EM segmentation. We also thank M.L. Gage for editorial comments, and A. Cao and T. Bartol for their help with 3DEM visualization. This work was supported by the American Heart Association and the Paul G. Allen Frontiers Group Grant #19PABHI34610000/TEAM LEADER: Fred H. Gage/2019, JPB Foundation, Annette C. Merle-Smith, Lynn and Edward Streim, the Milky Way Foundation, the Ray and Dagmar Dolby Family Fund, and NIH R37 AG072502-03, P30 AG062429-05, P30 AG068635-04, R01 AG070154-04, AG056306-07, P01 AG051449-08. This work was also supported by the NGS Core Facility, the GT3 Core Facility, the Razavi Newman Integrative Genomics and Bioinformatics Core Facility, and the Waitt Advanced Biophotonics Core Facility of the Salk Institute with funding from NIH-NCI CCSG: P30 014195, the Chapman Foundation, NINDS R24 Core Grant, and funding from NEI, and the Waitt Foundation. M.W. is supported by a NARSAD Young Investigator Grant from Brain & Behavior Research Foundation (BBRFNARSAD) and a Pioneer Fund Postdoctoral Scholar Award from the Salk Institute. Fig.2a, 2h, 4a, 5a, 6a and 6d were created with BioRender.com.

Author Contributions Statement

M.W., L.Z., and F.H.G. conceived the study and wrote the manuscript; M.W., L.Z., C.K.L. and S.F. performed cell culture and organoid differentiation; M.W., L.Z., C.K.L. and I.S.G. performed surgeries; S.L.P. assisted in surgeries; M.W. and I.S.G. performed single nucleus RNA-seq and single cell RNA-seq; M.W., C.Q., and E.M. performed NanoString GeoMx DSP; M.W., M.S., J.Y., and A.W. performed bioinformatics analyses; M.W. and L.Z. performed imaging analysis with assistance from L.L.X., C.K.L., S.C. and M.D.S.; L.Z., S.W.N. and L.A. performed sample processing for scanning electron microscopy; S.W.N. and L.A. performed electron microscopic image analysis under the supervision of M.W., L.Z. and U.M.; F.H.G. provided funding.

Competing interests Statement

The authors declare no competing interests.

Figure Legends

Figure 1. Enhanced astrogliogenesis in glia-enriched cortical organoids.

a. Differentiation protocol schematic: astrocyte medium (AstroM); fetal bovine serum (FBS). **b.** Immunostaining for glial progenitors (NFIA, magenta) and stem cells (SOX2, green). Scale bars, 20 μm. **c.** Quantification of $NFIA^+$ cells in forebrain (gray bars; Hues6 n=9; iPSC822 n=7) or glia-enriched cortical organoids (red bars; Hues6 n=7; iPSC822 n=6) from two batches of differentiation. Each dot represents one organoid. Mean ± s.e.m. Two-sided t-test with Welch's correction. ***$p < 0.001$. **d.** Immunostaining for astrocytes (GFAP, magenta) and progenitor cells (SOX2, green). Scale bars, 20 μm. **e.** $GFAP^+$ area quantified in forebrain (gray bars; Hues6 n=10; iPSC822 n= 9) and glia-enriched cortical organoids (red bars; Hues6 n=9; iPSC822 n= 8) from two batches of differentiation. Each dot represents one organoid. Mean ± s.e.m. Two-sided t-test with Welch's correction. ***$p < 0.001$, **$p < 0.01$. **f.** Immunostaining for astrocytes (HepaCAM, magenta; GFAP, green). Scale bars, 20 μm. **g.** $HepaCAM^+$ area quantified in forebrain (gray bars; Hues6 n=5; iPSC822 n= 6) and glia-enriched cortical organoids (red bars; Hues6 n=6; iPSC822 n= 7) from two batches of differentiation. Each dot represents one organoid. Mean ± s.e.m. Two-sided t-test with Welch's correction. **$p < 0.01$. **h.** UMAP plot displaying snRNA-seq data (n= 15,287 nuclei) from 10-week-old organoids from two lines after batch correction. APC (astrocyte progenitor cell), Ast (astrocyte), IPC (intermediate progenitor cell), In (inhibitory neuron), Cortical Ex (cortical excitatory neuron), and Ex (excitatory neuron). **i.** Dendrogram from WGCNA of astrocyte gene modules. **j.** UMAP plot of module hub gene expression score for astrocyte gene modules M12 and M14. **k.** Coexpression plots of the top 25 module genes for astrocyte gene modules M12 and M14. **l.** Confocal images of the GFAP::GFP AAV-transduced astrocytes and traces of processes. Top, three-month-old organoids. Bottom, five-month-old organoids. Scale bars, 20 μm. **m.** Sholl analysis of astrocytes (three-month-old, 33 astrocytes; five-month-old, 59 astrocytes). Mean ± s.e.m. **n.** Bar plots illustrating the number of primary processes, number of branches, and total process length (three-month-old, 33 astrocytes; five-month-old, 59 astrocytes). Mean ± s.e.m. Two-sided t-test with Welch's correction. ****$p < 0.0001$.

Figure 2. Human astrocytes form anatomically defined morphological subclasses *in vivo*.

a. Illustration depicting the experimental procedure. **b.** Immunostaining for H9-GFP-derived transplant (GFP, green) and nuclei (DAPI, blue). **c.** Immunostaining of six-month-old transplants: astrocytes (GFAP, green), human nuclear antigen (HuNu, magenta). Top inset, interlaminar astrocytes; Middle inset, protoplasmic astrocytes; Bottom inset, fibrous astrocytes. Scale bars, 100 μm (left panel), 50 μm (right panels). **d.** Immunostaining of GFAP::GFP AAV-transduced astrocytes: human nuclear antigen (HuNu, cyan), astrocytes (GFAP, magenta). Top, human astrocytes; Bottom, mouse astrocytes. Scale bars, 20 μm. **e.** Maximal diameter comparison of GFAP::GFP AAV-transduced human and mouse cortical astrocytes.

Mouse, n = 30 from three mice; human, n = 46 from three transplants. Mean ± s.e.m. Two-sided t-test with Welch's correction. ****$p < 0.0001$. **f.** Immunostaining for human [top; $hGFAP^+$ (magenta) and $GFAP^+$ (green)] and mouse astrocytes [bottom; $hGFAP^-$ (magenta) and $GFAP^+$ (green)] and blood vessels (Ly6C, cyan). Scale bars, 20 μm. **g.** GFAP::tdTomato lentivirus-labeled human astrocytes in transplants (tdTomato, magenta). Arrowheads: varicosities in astrocyte processes. Scale bars, 20 μm. **h.** Overview of the GeoMx Digital Spatial Profiler (DSP) workflow. **i.** Immunofluorescent staining image of one brain section with overlying selected Regions of Interest (ROIs). Scale bar, 750 μm. 38 ROIs (pial = 10, cortex = 16, WM = 12) from 4 sections were analyzed. **j.** Top: immunofluorescent staining: hGFAP (yellow), SOX9 (magenta), SYTO-13 (blue); bottom: cell segmentation of $SOX9^+$/$CYTO\text{-}13^+$ cells within ROI. Scale bar, 100 μm. **k.** PCA plot of GeoMx DSP gene expression data. Points: segmented $SOX9^+$/$CYTO\text{-}13^+$ cells per ROI, colored by location. **l.** Volcano plots of differentially expressed genes (DEGs) between astrocyte groups. Dashed lines: adjusted p value < 0.05 (linear mixed effect model with Benjamini-Hochberg multiple correction) and fold change (FC) >1.5. **m.** Box plots depicting the normalized expression levels of selected genes in each group (pial = 10, cortex = 16, WM = 12). Center line, median; box limits, upper and lower quartiles; whiskers, 1.5x interquartile range; points, outliers.

Figure 3. Human astrocytes form perivascular endfeet *in vivo*.

a. Confocal images comparing *in vitro* glia-enriched cortical organoids (top, six-month-old) and organoid transplants (bottom, six-month-old). Immunostaining for human astrocytes (hGFAP, green). Scale bars, 100 μm. **b.** Quantification of the number of $hGFAP^+$ cells per mm^2 in glia-enriched cortical organoids *in vitro* (left) and transplants *in vivo* (right). n = 6 organoids *in vitro* and n = 4 transplants (*in vivo*). Two-sided t-test with Welch's correction, *** $P < 0.001$. Bars, mean ± s.e.m. **c.** Confocal images comparing glia-enriched cortical organoids *in vitro* (left panels, six-month-old) and transplants *in vivo* (right panels, six-month-old). Immunostaining for human astrocytes (hGFAP, green) and water channel Aquaporin 4 (AQP4, magenta). Scale bars, 20 μm. **d.** Electron micrograph of the lumen of a blood vessel in an eight-month-old transplant captured using a scanning electron microscope. Top panel: endothelial cells (purple), basement membrane (blue), and intercellular leaflets (yellow). Bottom panel: enlarged view from the top panel. Scale bars, 4 μm. **e.** Electron micrograph of a capillary in the transplant. Boxes show astrocyte processes. Top right, arrowheads indicate glycogen granules. Bottom right, an arrowhead indicates glia filaments (GFAP). M, mitochondria. Scale bars, 1 μm. **f-g.** Electron micrograph of a capillary consists of endothelial cells (purple), tight junctions (yellow), pericytes (brown), and basement membrane (blue). The vessel was wrapped by astrocytic processes (green). Astrocyte soma (light green). 3D reconstruction of segmented data from serial section EM (**f**). Pseudocolored 2D image (**g**). Scale bars, 2 μm.

Figure 4. Advanced maturation of astrocytes in engrafted organoids revealed by snRNA-seq analyses. **a.** Schematic representation of snRNA-seq and related analyses. **b.** UMAP plot of snRNA-seq data (n= 65,743 nuclei) from five-month-old glia-enriched cortical organoids (5m_Org, n= 17,490 nuclei), 5-month-old transplants (5m_T, n= 15,936 nuclei), six-month-old transplants (6m_T, n= 15,607 nuclei), and eight-month-old transplants (8m_T, n= 16,710 nuclei) from two lines after batch correction. Ast, astrocyte; OPC, oligodendrocyte progenitor cell; In, inhibitory neuron; Immature, immature excitatory neuron; DL, deep layer cortical excitatory neuron; UL, upper layer cortical excitatory neuron. **c.** UMAP plots of snRNA-seq data separated by individual samples. **d.** Ridge plot of predicted nuclei ages separated by time point. Wilcoxon test (two-sided, ****, $p < 0.0001$; reference group, 5m_Org). **e.** Coexpression plot of top 25 module hub genes. **f.** UMAP plot of module hub gene expression score for astrocyte modules M5. **g.** Violin plot of harmonized module score of astrocyte module M5 in astrocytes across different time points. Wilcoxon test (two-sided, ****, $p < 0.0001$; reference group, 5m_Org). Center line, median; box limits, upper and lower quartiles; whiskers, 1.5x interquartile range; points, outliers. **h.** Module expression score of mature astrocyte genes curated from Zhang et al., 2016 in astrocytes separated by each time point. Each dot represents median value per cell line. Wilcoxon test (two-sided, ****, $p < 0.0001$; reference group, 5m_Org). **i.** Dot plot showing the expression of selected mature astrocyte genes reported in Zhang et al., 2016. **j.** UMAP dimensionality reduction of astrocytes from the integrated snRNA-seq. Each cell is colored by its pseudotime trajectory assignment. Pseudotime analysis separated by time point. One-sided Kolmogorov–Smirnov test (****, $p < 2.2e-16$; reference group, 5m_Org). **k.** Projection of cortical organoid transplants snRNA-seq nuclei (Revah et al., 2022 right) onto the reference of nuclei (8m_T, left). **l.** Heatmap of predicted cell type of cortical organoid transplants (Revah et al., 2022) on to the reference nuclei (8m_T). **m.** Ridge plot of predicted ages of astrocyte nuclei from eight-month-old glia-enriched cortical organoid transplants (8m_T) and cortical organoid transplants (Revah et al., 2022). Wilcoxon test (two-sided, ****, P value = 2.613246e-75).

Figure 5. Transcriptome profiling reveals rapid activation of proinflammatory pathways in a subpopulation of astrocytes *in vivo*.

a. Schematic representation of the experimental design. **b.** UMAP plot of scRNA-seq data from saline-treated transplants (n = 7404 cells) and TNFα-treated transplants (n = 5835 cells) after batch correction. **c.** UMAP plot displaying all Seurat clusters (left) and the number of cluster 2 astrocytes in each condition. UpSetR plots showing the upregulated DEGs (**d**) and downregulated DEGs (**e**) that are unique to or shared between astrocyte clusters 1-4. **f.** Violin plot illustrating the expression of selected genes in astrocyte clusters 1-4. **g.** GSEA comparing TNFα-treated and saline-treated cluster 2 astrocytes. Hallmark gene sets are shown. FDR, false discovery rate; NES, normalized enrichment score.

Figure 6. CD38 mediates inflammation-induced metabolic and mitochondrial stresses in human astrocytes.

a. Schematic representation of the experimental design. **b.** Confocal images of *in vitro* six-month-old glia-enriched cortical organoids at different time points (day 0, day 1, and day 2) post TNFα treatment. Immunostaining for astrocytes (GFAP, green) and monocyte chemoattractant protein-1 (CCL2, magenta). Scale bars, 200 μm. **c.** Quantification of the percentage of astrocytes with nuclear translocation of NF-κB (three organoids per group). Each dot represents one organoid. Bars, mean ± SD. Two-sided t-test, **$p < 0.01$, ****$p < 0.0001$. **d.** Schematic representation of astrocyte purification process from organoids. **e.** Dot plot showing the ratio of NAD^+ to NADH (n = 8 independent experiments per group). Each dot represents one independent experiment. Bars, mean ± SD. Two-sided t-test, ****$p < 0.0001$. **f.** Dot plot showing the ratio of GSSH to GSSG (n = 6 independent experiments per group). Each dot represents one independent experiment. Bars, mean ± SD. Two-sided t-test, ****$p < 0.0001$. **g.** Confocal images of astrocytes treated with saline, TNFα, and TNFα together with CD38 inhibitor 78c. Immunostaining for astrocytes (GFAP::tdTomato, magenta) and mitochondria (mitoGFP, green). Scale bars, 10 μm. **h.** Percentage of astrocytes with fragmented mitochondria (CTRL = 150 cells examined over three independent experiments; TNFα1d = 150 cells examined over three independent experiments; TNFα2d = 150 cells examined over three independent experiments; TNFα2d + CD38i = 200 cells examined over four independent experiments). Each dot represents one independent experiment. Bars, mean ± SD. Two-sided t-test, **$p < 0.01$, ****$p < 0.0001$.

References

1 Liddelow, S. A. *et al.* Neurotoxic reactive astrocytes are induced by activated microglia. *Nature* **541**, 481-487, doi:10.1038/nature21029 (2017).

2 Qian, X., Song, H. & Ming, G. L. Brain organoids: advances, applications and challenges. *Development* **146**, doi:10.1242/dev.166074 (2019).

3 Wang, M., Zhang, L. & Gage, F. H. Modeling neuropsychiatric disorders using human induced pluripotent stem cells. *Protein Cell* **11**, 45-59, doi:10.1007/s13238-019-0638-8 (2020).

4 Lancaster, M. A. *et al.* Cerebral organoids model human brain development and microcephaly. *Nature* **501**, 373-379, doi:10.1038/nature12517 (2013).

5 Kim, J., Koo, B. K. & Knoblich, J. A. Human organoids: model systems for human biology and medicine. *Nat Rev Mol Cell Biol* **21**, 571-584, doi:10.1038/s41580-020-0259-3 (2020).

6 Velasco, S. *et al.* Individual brain organoids reproducibly form cell diversity of the human cerebral cortex. *Nature* **570**, 523-527, doi:10.1038/s41586-019-1289-x (2019).

7 Sloan, S. A. *et al.* Human Astrocyte Maturation Captured in 3D Cerebral Cortical Spheroids Derived from Pluripotent Stem Cells. *Neuron* **95**, 779-790 e776, doi:10.1016/j.neuron.2017.07.035 (2017).

8 Qian, X. *et al.* Sliced Human Cortical Organoids for Modeling Distinct Cortical Layer Formation. *Cell Stem Cell* **26**, 766-781 e769, doi:10.1016/j.stem.2020.02.002 (2020).

9 Molofsky, A. V. *et al.* Astrocytes and disease: a neurodevelopmental perspective. *Genes Dev* **26**, 891-907, doi:10.1101/gad.188326.112 (2012).

10 Tchieu, J. *et al.* NFIA is a gliogenic switch enabling rapid derivation of functional human astrocytes from pluripotent stem cells. *Nat Biotechnol* **37**, 267-275, doi:10.1038/s41587-019-0035-0 (2019).

11 Canals, I. *et al.* Rapid and efficient induction of functional astrocytes from human pluripotent stem cells. *Nat Methods* **15**, 693-696, doi:10.1038/s41592-018-0103-2 (2018).

12 Santos, R. *et al.* Differentiation of Inflammation-Responsive Astrocytes from Glial Progenitors Generated from Human Induced Pluripotent Stem Cells. *Stem Cell Reports* **8**, 1757-1769, doi:10.1016/j.stemcr.2017.05.011 (2017).

13 Barbar, L. *et al.* CD49f Is a Novel Marker of Functional and Reactive Human iPSC-Derived Astrocytes. *Neuron* **107**, 436-453 e412, doi:10.1016/j.neuron.2020.05.014 (2020).

14 Zhang, J. & Liu, Q. Cholesterol metabolism and homeostasis in the brain. *Protein Cell* **6**, 254-264, doi:10.1007/s13238-014-0131-3 (2015).

15 Daneman, R. & Prat, A. The blood-brain barrier. *Cold Spring Harb Perspect Biol* **7**, a020412, doi:10.1101/cshperspect.a020412 (2015).

16 Mansour, A. A. *et al.* An in vivo model of functional and vascularized human brain organoids. *Nat Biotechnol* **36**, 432-441, doi:10.1038/nbt.4127 (2018).

17 Bao, Z. *et al.* Human Cerebral Organoid Implantation Alleviated the Neurological Deficits of Traumatic Brain Injury in Mice. *Oxid Med Cell Longev* **2021**, 6338722, doi:10.1155/2021/6338722 (2021).

18 Daviaud, N., Friedel, R. H. & Zou, H. Vascularization and Engraftment of Transplanted Human Cerebral Organoids in Mouse Cortex. *eNeuro* **5**, doi:10.1523/ENEURO.0219-18.2018 (2018).

19 Kitahara, T. *et al.* Axonal Extensions along Corticospinal Tracts from Transplanted Human Cerebral Organoids. *Stem Cell Reports* **15**, 467-481, doi:10.1016/j.stemcr.2020.06.016 (2020).

20 Shi, Y. *et al.* Vascularized human cortical organoids (vOrganoids) model cortical development in vivo. *PLoS Biol* **18**, e3000705, doi:10.1371/journal.pbio.3000705 (2020).

21 Revah, O. *et al.* Maturation and circuit integration of transplanted human cortical organoids. *Nature* **610**, 319-326, doi:10.1038/s41586-022-05277-w (2022).

22 Jgamadze, D. *et al.* Structural and functional integration of human forebrain organoids with the injured adult rat visual system. *Cell Stem Cell* **30**, 137-152 e137, doi:10.1016/j.stem.2023.01.004 (2023).

23 Qian, X. *et al.* Generation of human brain region-specific organoids using a miniaturized spinning bioreactor. *Nat Protoc* **13**, 565-580, doi:10.1038/nprot.2017.152 (2018).
24 Qian, X. *et al.* Brain-Region-Specific Organoids Using Mini-bioreactors for Modeling ZIKV Exposure. *Cell* **165**, 1238-1254, doi:10.1016/j.cell.2016.04.032 (2016).
25 Langfelder, P. & Horvath, S. WGCNA: an R package for weighted correlation network analysis. *BMC Bioinformatics* **9**, 559, doi:10.1186/1471-2105-9-559 (2008).
26 Morabito, S. *et al.* Single-nucleus chromatin accessibility and transcriptomic characterization of Alzheimer's disease. *Nat Genet* **53**, 1143-1155, doi:10.1038/s41588-021-00894-z (2021).
27 Allen, N. J. & Eroglu, C. Cell Biology of Astrocyte-Synapse Interactions. *Neuron* **96**, 697-708, doi:10.1016/j.neuron.2017.09.056 (2017).
28 Stogsdill, J. A. *et al.* Astrocytic neuroligins control astrocyte morphogenesis and synaptogenesis. *Nature* **551**, 192-197, doi:10.1038/nature24638 (2017).
29 Oberheim, N. A. *et al.* Uniquely hominid features of adult human astrocytes. *J Neurosci* **29**, 3276-3287, doi:10.1523/JNEUROSCI.4707-08.2009 (2009).
30 Zhang, Y. *et al.* Purification and Characterization of Progenitor and Mature Human Astrocytes Reveals Transcriptional and Functional Differences with Mouse. *Neuron* **89**, 37-53, doi:10.1016/j.neuron.2015.11.013 (2016).
31 Oberheim, N. A., Wang, X., Goldman, S. & Nedergaard, M. Astrocytic complexity distinguishes the human brain. *Trends Neurosci* **29**, 547-553, doi:10.1016/j.tins.2006.08.004 (2006).
32 Merritt, C. R. *et al.* Multiplex digital spatial profiling of proteins and RNA in fixed tissue. *Nat Biotechnol* **38**, 586-599, doi:10.1038/s41587-020-0472-9 (2020).
33 Li, Y. *et al.* Direct labeling and visualization of blood vessels with lipophilic carbocyanine dye DiI. *Nat Protoc* **3**, 1703-1708, doi:10.1038/nprot.2008.172 (2008).
34 Herring, C. A. *et al.* Human prefrontal cortex gene regulatory dynamics from gestation to adulthood at single-cell resolution. *Cell* **185**, 4428-4447 e4428, doi:10.1016/j.cell.2022.09.039 (2022).
35 Cao, J. *et al.* The single-cell transcriptional landscape of mammalian organogenesis. *Nature* **566**, 496-502, doi:10.1038/s41586-019-0969-x (2019).
36 Sofroniew, M. V. & Vinters, H. V. Astrocytes: biology and pathology. *Acta Neuropathol* **119**, 7-35, doi:10.1007/s00401-009-0619-8 (2010).
37 Zamanian, J. L. *et al.* Genomic analysis of reactive astrogliosis. *J Neurosci* **32**, 6391-6410, doi:10.1523/JNEUROSCI.6221-11.2012 (2012).
38 Anderson, M. A. *et al.* Astrocyte scar formation aids central nervous system axon regeneration. *Nature* **532**, 195-200, doi:10.1038/nature17623 (2016).
39 Tarrago, M. G. *et al.* A Potent and Specific CD38 Inhibitor Ameliorates Age-Related Metabolic Dysfunction by Reversing Tissue NAD(+) Decline. *Cell Metab* **27**, 1081-1095 e1010, doi:10.1016/j.cmet.2018.03.016 (2018).
40 Sprenger, H. G. & Langer, T. The Good and the Bad of Mitochondrial Breakups. *Trends Cell Biol* **29**, 888-900, doi:10.1016/j.tcb.2019.08.003 (2019).
41 Krencik, R. & Zhang, S. C. Directed differentiation of functional astroglial subtypes from human pluripotent stem cells. *Nat Protoc* **6**, 1710-1717, doi:10.1038/nprot.2011.405 (2011).
42 Palm, T. *et al.* Rapid and robust generation of long-term self-renewing human neural stem cells with the ability to generate mature astroglia. *Sci Rep* **5**, 16321, doi:10.1038/srep16321 (2015).
43 Han, X. *et al.* Forebrain engraftment by human glial progenitor cells enhances synaptic plasticity and learning in adult mice. *Cell Stem Cell* **12**, 342-353, doi:10.1016/j.stem.2012.12.015 (2013).
44 Windrem, M. S. *et al.* A competitive advantage by neonatally engrafted human glial progenitors yields mice whose brains are chimeric for human glia. *J Neurosci* **34**, 16153-16161, doi:10.1523/JNEUROSCI.1510-14.2014 (2014).
45 Mariani, J. N., Zou, L. & Goldman, S. A. Human Glial Chimeric Mice to Define the Role of Glial Pathology in Human Disease. *Methods Mol Biol* **1936**, 311-331, doi:10.1007/978-1-4939-9072-6_18 (2019).

46 Zeisel, A. *et al.* Brain structure. Cell types in the mouse cortex and hippocampus revealed by single-cell RNA-seq. *Science* **347**, 1138-1142, doi:10.1126/science.aaa1934 (2015).
47 Bayraktar, O. A. *et al.* Astrocyte layers in the mammalian cerebral cortex revealed by a single-cell in situ transcriptomic map. *Nat Neurosci* **23**, 500-509, doi:10.1038/s41593-020-0602-1 (2020).
48 Hodge, R. D. *et al.* Conserved cell types with divergent features in human versus mouse cortex. *Nature* **573**, 61-68, doi:10.1038/s41586-019-1506-7 (2019).
49 Jorstad, N. L. *et al.* Transcriptomic cytoarchitecture reveals principles of human neocortex organization. *Science* **382**, eadf6812, doi:10.1126/science.adf6812 (2023).
50 Burda, J. E. *et al.* Divergent transcriptional regulation of astrocyte reactivity across disorders. *Nature* **606**, 557-564, doi:10.1038/s41586-022-04739-5 (2022).

Methods

Human pluripotent stem cells

Human embryonic stem cells (hESCs) Hues6 (NIH approved ESC line, obtained from HSCI iPS Core) [51], H9 (Wisconsin International Stem Cell (WISC) bank, WiCell research Institute, WA09 cells) [52] and human induced pluripotent cells (hiPSCs) 822 were used in the current study. H9 cells were transduced with pCSC-CAG-GFP lentiviruses and GFP-expressing cells were FACS-sorted as previously described [16]. Protocols were previously approved by the Salk Institutional Review Board and informed consent was obtained from the subjects.

Mice

All animal experiments described in the current study were approved by the Institutional Animal Care and Use Committee (IACUC) at the Salk Institute for Biological Studies (12-00022) and were conducted in compliance with the National Institute of Health's Guide for the Care and Use of Laboratory Animals. Immune-deficient mice NOD.Cg-*Prkdc*^{scid} *Il2rg*^{tm1Wjl}/SzJ (Jackson Laboratory, stock number 005557) were generated in our lab by breeding and kept on a 12h light/dark cycle in a housing group of two to five mice in each cage. Male and female mice 6-12 weeks of age were randomly used in this study.

Human pluripotent stem cell culture

Human pluripotent stem cells (PSCs) were cultured as previously described [16,53]. PSC colonies were maintained on Matrigel-coated six-well plates (Matrigel, Corning, 354277, hESC-Qualified) using mTeSR Plus (Stemcell Technologies, 85850) and were incubated in a 5% CO_2 humidified atmosphere at 37°C. PSC colonies were passaged at a ratio of 1:6 every three to six days using ReLeSR (Stemcell technologies, 5872). All human PSCs were maintained in feeder-free culture condition for 20-40 generations and confirmed negative for mycoplasma. Cells were confirmed normal with karyotyping. All experiments involving cells from human subjects were performed in compliance with the institutional Embryonic Stem Cell Research Oversight (ESCRO) committee.

Generation of glia-enriched cortical organoids

To generate embryoid bodies (EBs), intact PSC colonies were treated with 1 mg/ml Collagenase type IV (Invitrogen, 17104-019) for 20-45 minutes at 37 °C and mechanically detached with a cell scraper. Dissociated colonies were maintained in an ultra-low-attachment dish (Nunc) under stationary conditions for two days and were fed with mTeSR Plus supplemented with 10mM ROCK inhibitor Y-27632 (Tocris, 1254). From day 1, cells were maintained in Astrocyte medium (AM) (ScienCell, 1800) supplemented with

Astrocyte Growth Supplement (AGS, Sciencell, 1800), 2% Fetal Bovine Serum, 500 ng/ml Noggin (R&D Systems, 6057-NG), 10 ng/mL PDGFAA (Proteintech, HZ-1215) and 1x 2-Mercaptoethanol (Gibco, 21985032) until day 14. On day 15, organoids (10-12 organoids in each well of six-well ultra-low-attachment plates) were transferred on to an orbital shaker (75 r.p.m.) and maintained in AM supplemented with AGS, 10 ng/ml PDGFAA, and 1x 2-Mercaptoethanol for an additional week. From day 22, organoids were maintained on orbital shaker (75 r.p.m.) in medium consisting of DMEM/F-12 with Glutamax (Thermo Fisher Scientific, 10565018), 1 x N2 supplement (Thermo Fisher Scientific, 17502-048), 1x B27 (without RA) (Thermo Fisher Scientific, 12587010), 1x MEM-NEAA (Thermo Fisher Scientific, 11140050), 10% Fetal Bovine Serum (Omega Scientific Cat#FB-01; Lot#991851), and 1x 2-Mercaptoethanol. Organoids cultured beyond day 60 were additionally supplemented with 20 ng/ml BDNF (R&D Systems, 248-BDB), 20 ng/ml GDNF (R&D Systems, 212-GD), 0.2 mM Ascorbic Acid (Stemcell Technologies, 72132), 0.5 mM cAMP (Tocris, 1141). All media changes were done every other day. All organoids for transplantation experiments were pre-selected for development of organized neuroepithelium budding and absence of cyst formation. In addition, organoids from the same culture batch were examined by immunostaining for verification of neuronal and glial differentiation.

Intracerebral implantation of glia-enriched cortical organoids

Organoid implantations were performed as previously described [16]. Glia-enriched organoids were cultured *in vitro* for 8 to 10 weeks prior to implantation. Mice were anesthetized with 3-5% isoflurane inhalation for induction and 1-2% isoflurane for maintenance. Each animal was fixed onto a stereotaxic frame for the duration of all surgical procedures with body temperatures maintained at 37 °C using a water-circulation heating pad (Gaymar Industries). Dexamethasone (2.5 mg/kg) was injected subcutaneously to minimize edema. Upon the removal of the skin above the scalp, a ~3mm diameter craniotomy was performed by drilling into the skull. The underlying dura mater was subsequently removed with forceps. A unilateral lesion was created in the region of the retrosplenial cortex through aspiration with a blunt-tip needle attached to a vacuum line. The brain tissue overlying the anterior colliculus was removed and the vascular bed of the choroidal fissure was exposed. Sterile saline and a piece of Gelfoam (Pfizer) were used to prevent excessive bleeding. The organoid transplant was placed on the pial vessels overlying the collicles caudal to the hippocampus. Upon transplantation, the organoid was sealed with a 5-mm glass coverslip using adhesive glue and the wound was secured with dental cement (Stoelting) [54]. Upon completion of the surgery, carprofen (5 mg/kg, i.p., 100 µl of 1 mg/ml) and Buprenorphine SR-Lab (1.0 mg/kg, subcutaneous) were administered to minimize inflammation and pain. The mice were then returned to their home cages for recovery on a heating pad.

Stereotaxic injection

Mice were anesthetized with 3-5% isoflurane via inhalation for induction and 1-2% isoflurane for maintenance. Each mouse was fixed onto a stereotaxic frame for the duration of all surgical procedures with body temperatures maintained at 37 °C using a water-circulation heating pad (Gaymar Industries). For direct TNFα injection into brain organoids, the preexisting dental cement and cranial window were removed first, followed by injection of 1µl of 250 ng of recombinant human TNFα (Sino Biological Inc, 10602-HNAE) or saline at a speed of 1µl per minute using a Hamilton syringe. The 1µl injection volume was split across two different Z locations. After the injection was completed, the needle was retracted at a rate of 0.2–0.5 mm per minute. A new cranial window was placed using adhesive glue and secured with dental cement (Stoelting). Buprenorphine SR-Lab (1.0 mg/kg, subcutaneous) was administered to minimize postoperative pain. The mice were immediately placed on a warm heating pad until recovery.

Virus transduction

pBOB-GFAP-tdTomato lentiviral vector was obtained from the lab of Dr. Inder Verma at the Salk Institute. Lentiviruses were produced by the virus core in Salk Institute. To transduce organoids, 1 µl of lentivirus (titer was10^12 GC/ml) was added in each well of a six-well plate containing 3 ml medium and four to six organoids. Virus-containing medium was completely changed after two days.

pAAV.GFAP.eGFP.WPRE.hGH AAV5 viral prep was a gift from James M. Wilson (Addgene viral prep # 105549-AAV5; RRID:Addgene_105549 with a titer of 10^13 GC/ml. AAV particles were injected into the mouse brain to visualize human and mouse astrocytes. Briefly, a mouse with organoid implant was anesthetized with isoflurane (5% for induction and 2% for maintenance). The mouse was fixed on the stereotaxic instrument and the glass coverslip covering the implant was drilled through. One µl AAV5 virus was slowly injected into the organoid transplant for a duration of 5 min. The mice were allowed to recover on a heating pad and returned to their home cages.

Histological processing

In vitro cultured organoids were fixed in 4% paraformaldehyde (PFA) for 45-60 minutes followed by three washings with PBS. Organoids were then transferred to 30% sucrose solution at 4°C overnight. Four to six organoids were transferred into blocks in tissue-freezing medium, frozen on dry ice, and stored at -80°C.

To obtain brain tissues containing organoid implants, the mice were first deeply anesthetized with Ketamine/xylazine (130 mg/kg, 15 mg/kg; i.p.) and then subjected to transcardial perfusion of 15ml ice saline followed by 15 ml 4% PFA. The brains were subsequently dissected out and transferred into 15-ml conical tubes containing 4% PFA for post-fixation overnight at 4°C. Brains were cryoprotected for 48-72

hr in 30% sucrose with 0.05% NaN3 at 4°C. Each brain was trimmed coronally and embedded in tissue-freezing medium (GeneralData).

All blocks were left to equilibrate to the temperature of the cryostat ~30 min prior to sectioning. Thirty 40-µm cryosections of organoids were obtained using a cryostat (Leica), mounted on Superfrost plus slides (Thermo Scientific, Menzel-Glaser), dried at RT for 30 min and stored at -20°C. For each section set, one section was collected onto a slide to obtain a total of 20 slides and this collection method was repeated until tissue was exhausted.

Immunohistochemistry and imaging acquisition

Immunofluorescence staining was performed with thawed slides, with the tissue area and slide edges outlined using a hydrophobic PAP pen. The slides were washed three times with PBS and blocked and permeabilized in blocking solution (5% normal donkey serum, 0.1% Triton X-100 in PBS) in a humidified chamber for 1h at RT. Organoid slides were incubated with primary antibodies diluted in the blocking solution at 4°C overnight. Primary antibodies used were anti-NFIA (rabbit, ab41851, Abcam; 1:250), anti-SOX2 (rat, 14-9811-82, clone#Btjce, Invitrogen; 1:400), anti-GFAP (rabbit, Z0334, Dako; 1:500), anti-GFAP (chicken, AB5541, EMD Millipore; 1:1000), anti-GFP (chicken, GFP-1020, Aves lab;1:1000), anti-hGFAP (mouse, Y40420, clone# not provided by vendor, TaKaRa; 1:500), anti-Human Nuclear Antigen (HuNu) (mouse, ab215755, clone#235-1, Abcam; 1:250), anti-NeuN (rabbit, ABN78, EMD Millipore; 1:250), anti-Ly6C (rat, ab15627,Clone# ER-MP20, Abcam; 1:500), anti-Aquaporin 4 (AQP4) (rabbit, AQP-004, Alomone Labs; 1:400), anti-Kir4.1 (rabbit, APC-035, Alomone Labs; 1:250), anti-glucose transporter GLUT1 (rabbit, ab115730, Abcam; 1:100), anti-tdTomato (rabbit, 600-401-379, Rockland; 1:500), anti-Laminin (rabbit, NB300-144SS, Novus a biotechne brand; 1:500), anti-hHepaCAM (mouse, MAB4108, clone#419305, R&D Systems; 1:400), anti-S100B (rabbit, ab52642, Abcam; 1:1000), anti-TBR2/Eomes (rabbit, ab275960, Abcam; 1:250), anti-CTIP2 (rat, ab18465, clone# 25B6, Abcam; 1:200), anti-SATB2 (rabbit, ab92446, Abcam;1:100), anti-HOPX (mouse, sc-398703, clone# E-1, Santa Cruz; 1:200), anti-NG2 (rabbit, AB5320, EMD Millipore; 1:200), anti-CD31 (goat, AF3628, R&D Systems; 1:500), anti-IBA1 (rabbit, 019-19741, Wako; 1:400), anti-IBA1 (goat, ab48004, Abcam; 1:400), anti-SV2 (mouse, SV2-c, clone# not provided by vendor, DSHB; 1:500), anti-PSD95 (rabbit, 51-6900, Invitrogen; 1:250), anti-Myelin Basic protein (MBP) (rabbit, ab218011, Abcam; 1:400), anti-CD44 (rat, MAB6127, clone # IM7.8.1R, R&D Systems; 1:500), anti-EAAT2 (mouse, sc-365634, clone# E-1, Santa Cruz; 1:250), anti-hSPARC-like 1 (HEVIN) (goat, AF2728, R&D Systems; 1:50), anti-PDGFRa (rabbit, ab203491, Abcam; 1:200), anti-hCD38 (mouse, MAB2404, clone# 240742, R&D Systems; 1:200), anti-CXCL10/IP10 (rabbit, MA5-32674, Invitrogen; 1:200), anti-CCL2/MCP-1 (rabbit, NBP1-07035, Novus a biotechne brand; 1:100), and anti-Connexin 43 (rabbit, 3512S, Cell Signaling Technology; 1:200). After

three washes with PBS, slides were incubated with the appropriate fluorochrome-conjugated secondary antibodies diluted in blocking solution at RT for 1h in the dark. Alexa Fluor secondary antibodies (Jackson ImmunoResearch) diluted in blocking solution at 1:250 were used. Finally, all slides were counterstained with DAPI (1 μg/ml, D9542; Sigma) for 5 min, rinsed three times in PBS before mounting with mounting solution (ProLong gold, Thermo Fisher Scientific) and left to dry for at least 48 hours at RT before imaging acquisition. Slides were stored at 4°C.

All images were acquired on a Zeiss LSM880 confocal microscope, Olympus VS-120 Virtual Slide Scanning Microscope (Olympus), or Revolve (ECHO), and processed with Zen software (Zeiss) and ImageJ software (NIH).

NanoString GeoMx Digital Spatial Profiler

Formalin-fixed paraffin-embedded (FFPE) tissue from a mouse brain with human organoid transplant was sectioned at 5μm and mounted onto positively charged slides with four sections per slide; subsequently it was profiled utilizing a NanoString GeoMx Digital Spatial Profiler (NanoString Technologies) as previously described[32]. The NanoString commercial Human Whole Transcriptome Atlas (GeoMx WTA) panel (>18,000 protein-coding genes) was selected. Tissue morphology was visualized using fluorescent-conjugated hGFAP Alexa-Fluor-594 (STEM123, TaKaRa, conjugated using Lightning-Link Rapid Alexa Fluor 594 Antibody Labeling Kit, 8μg/ml), SOX9 Alexa Fluor-647 (clone EPR14335, ab196184, abcam, 8μg/ml), and SYTO-13 to detect nucleic acids. The slide was scanned on a NanoString GeoMx DSP platform and individual regions of interest (ROIs) with a maximum diameter of 660μm were created. Once each ROI was compartmentalized, cell segmentation was performed to identify $SOX9^{+}$/$CYTO\text{-}13^{+}$ cells for subsequent ultraviolet-cleaved indexing oligonucleotides collection into a 96-well plate. Libraries were prepared according to the manufacturer's instructions (protocol MAN-10153-03). Samples were sequenced on the Illumina MiniSeq platform (MiniSeq High Output Kit PE 75 cycles) and reads were digitally quantified and normalized using GeoMx DSP Data Analysis Suite 3.0 (NanoString Technologies) following the manufacturer's instructions [32]. Target filtering was applied to retain gene targets with read counts above the limit of quantification [LOQ; defined as geomean (NegProbe) × geoSD $(\text{NegProbe})^2$ for each ROI] in at least 10% of ROIs. Q3 normalization was applied to the filtered ROIs and gene targets. The ROIs were categorized according to the spatial groups for subsequent analysis. Differential gene expression across groups was analyzed using a linear mixed effect model followed by the Benjamini-Hochberg multiple correction test. Differentially expressed genes (DEGs) were defined as fold-change > 1.5 or < -1.5, and adjusted $p < 0.05$. The parameters chosen for Gene Set Enrichment Analysis included a minimum coverage

of 20% of genes within the pathway and a pathway size between 15 and 500 genes, employing Reactome Version Build 78 + NCBI_08122021.

Cytokine Stimulation *in vitro*

Organoids or purified astrocytes were treated with 50 ng/mL recombinant human TNFα (Sino Biological Inc, 10602-HNAE) or PBS (vehicle) for 24 hours in maturation media. After washing with PBS, the samples were changed to fresh maturation media. To assess the effect of CD38 inhibition, samples were treated with 0.5 µM 78c (Tocris Bioscience, 6391) and 50 ng/mL TNFα for 24 hours in maturation media, followed by 0.5µM 78c for an additional 24 hours.

Mitochondrial Morphological Analysis

Purified astrocytes were transduced with a lentiviral vector encoding MitoEGFP under the CAG promoter. Cells were fixed in 4% paraformaldehyde for 10 minutes and washed for three times with PBS and subjected to immunohistochemistry and imaging acquisition. The EGFP signal (MitoEGFP) was used to analyze the mitochondrial shape in Image J (NIH).

Functional Assays

Reduced (GSH) and oxidized (GSSG) glutathione contents were assessed in astrocytes using the GSH/GSSG-Glo assay kit (Promega, V6611). The results are expressed as GSH/GSSG ratio. The NAD^+/NADH ratio was assessed in cultured astrocytes using the NAD-Glo assay kit (Promega, G9071).

Glutamate Uptake Assay

Astrocytes purified from three iPSC lines of five-month-old organoids and cultured neural progenitor cells (NPCs) were incubated in Hank's balanced salt solution (HBSS) buffer without calcium and magnesium (GIBCO) for 30 minutes, followed by incubation for 2 hours in HBSS containing calcium and magnesium (GIBCO) supplemented with 100 µM glutamate. After 2 hours, the media were collected and analyzed using a bioluminescent assay kit (Promega, Glutamate-Glo™ Assay, J7021) according to the manufacturer's instructions. Six to eight technical replicates per line were utilized.

Sholl analysis

GFAP::GFP AAV transduced astrocytes from three-month-old and five-month-old glia-enriched cortical organoids were stained with an antibody against GFP and imaged using a Zeiss LSM880 confocal microscope at 63x magnification with z-stack images. Images were opened in ImageJ and a maximum

intensity projection was performed. Astrocyte tracing was done manually using Simple Neurite Tracer tool [55]. Sholl analysis was carried out through Simple Neurite Tracer with radial intervals of 1.26732 µm.

Quantitative polymerase chain reaction

Total RNA was purified from organoids or astrocytes with a Direct-zol RNA Purification Kit (Zymo Research, R2061), according to the manufacturer's instructions. cDNA was synthesized using SuperScript III First-Strand Synthesis System (Invitrogen). Quantitative PCR was performed using SYBR Green PCR Master Mix (Applied Biosystems) on a BioRad CFX384 thermal cycler. The relative mRNA abundance of target genes was normalized to that of GAPDH mRNA obtained in the same sample. The primer sequences are shown in Supplementary Table 11.

Electron microscopy

A mouse with an implanted organoid was perfused and processed for electron microscopy as described elsewhere [56] with some modifications. The mouse was first anesthetized with ketamine/xylazine (130 mg/kg, 15 mg/kg; i.p.) and perfused with a 25 mL of warm oxygenated Ringers solution, followed by 15 mL of warm buffered fixative (2.5% glutaraldehyde, 2% paraformaldehyde, 3 mM $CaCl_2$, 0.15 M sodium cacodylate) with DiI added to the solution to fluorescently label vasculature as previously described [33]. The brain was carefully extracted from the skull and stored overnight at 4°C in fresh fixative solution. The following day, the brain was thoroughly rinsed with buffer (3 mM $CaCl_2$, 0.15 M sodium cacodylate) and 120-µm thick sections containing the organoid were collected using a vibrating blade microtome (Leica VT1000 S) with a bath of ice-cold buffer. Brain sections were serially rinsed with ice-cold buffer, followed by a rinse with ice-cold buffer containing 50 mM glycine. Sections were immersed in a shallow dish filled with ice-cold buffer and photographed using a dissecting microscope equipped with a camera (Olympus). Low resolution confocal imaging was performed for GFP and DiI. A small rectangle was microdissected from the center of the organoid for serial section scanning electron microscopy (S3EM). Sections used for scanning electron microscopy (SEM) were left intact for processing. Samples were processed for high contrast with heavy metals as described elsewhere [57]. Briefly, sections were immersed in buffered reduced osmium (1.5% osmium tetroxide, 1.5% potassium ferrocyanide, 3 mM $CaCl_2$, 0.15 M sodium cacodylate) for 45 minutes in the dark at RT. Samples were then serially rinsed with ice-cold distilled water before 30 minutes of treatment with filtered 1% aqueous thiocarbohydrazide that was prepared at 60°C for an hour before use. Samples were serially rinsed with ice-cold distilled water before amplifying staining with 1.5% aqueous osmium tetroxide for 45 minutes in the dark at RT. Sections to be imaged by SEM were set aside at this point for serial dehydration and critical point drying (Leica CPD300). The remaining microdissected samples were serially rinsed with ice-cold water before staining overnight with 1% uranyl acetate at 4°C.

The next day, samples were thoroughly rinsed with RT distilled water and stained with Walton's lead aspartate for 30 min at 60°C. Samples were rinsed again with RT distilled water and serially dehydrated in ice-cold ethanol. Samples were then rinsed three times in anhydrous ethanol prior to serial infiltration with Eponate 12 resin (hard formulation) over the course of two days and finally embedded in capsules (TAAB) for polymerization in a small oven for three days at 60°C.

A ribbon of approximately 100 serial ultrathin sections was collected, and each section of approximate dimensions of 150 µm-400 µm-70 nm (x-y-z) was collected onto a silicon chip using Diatome diamond knives mounted on a Leica UC7 ultramicrotome as described elsewhere [58]. The chip was mounted on an aluminum stub using carbon sticky tape and loaded into a Zeiss Sigma VP scanning EM equipped with a Gatan backscattered electron detector and both SmartSEM (Zeiss) and Atlas5 (Fibics) control software. A region of interest (ROI) near the center of the organoid implant was identified and images were acquired with an accelerating voltage of 1.5 kV, a 20-µm aperture, at a working distance of 9 mm. A multi-resolution map of a central section was acquired, identifying candidate blood vessels for further 3D analysis. Contiguous high-resolution images (8-8-70 nm/voxels x-y-z) of a representative ROI containing a blood vessel were assembled into a series of 8-bit tiff files. Serial images were aligned using AlignEM-SWiFT to form a continuous 3D representation of the tissue volume.

Endothelial cell processes, a pericyte, and astrocyte processes contacting the blood vessel as well as tight junctions and basement membrane were identified by their ultrastructural characteristics and annotated using VAST Lite software. Cells and nuclei were exported using the VAST Lite Matlab toolkit as .obj files, which were imported into Blender software equipped with GAMer and Neuromorph add-ons. Object meshes were processed with GAMer to optimize geometry for visualization, before superimposition with 3DEM data using Neuromorph. In this fashion, data were interrogated and rendered scenes and animations were produced using Blender. For video figures, rendered scenes were assembled into .avi files using ImageJ, post-processed using After Effects (Adobe), and compressed using Handbrake (https://handbrake.fr/).

Dissociation of brain organoids and single nucleus RNA-seq

Nuclei extraction from fresh dissected *in vivo* brain organoids was performed according to a demonstrated protocol CG000124 (Rev E, nuclei isolation from cell suspensions and tissues for single cell RNA sequencing) from 10x Genomics with minor modification. Briefly, freshly dissected *in vivo* brain organoids were pooled and lysed using a Dounce homogenizer in 1 ml of freshly prepared cold lysis buffer (TrisHCl pH 7.4 10 mM, NaCl 10 mM, $MgCl_2$ 3 mM, NP-40 0.1% in nucleus free water). Nuclei were centrifuged

at 500 g for 8 min and supernatant was discarded. Nuclei were then resuspended in freshly prepared cold nuclei wash & resuspension buffer (PBS, 1%BSA, Rnase inhibitor 0.2 U/μl) and filtered through a 35-μm strainer (Corning). Nuclei were centrifuged at 500 g for 5 minutes and resuspended again in nuclei wash and resuspension buffer for a total of two washes. After the second wash, nuclei were resuspended in ice-cold nuclei wash and resuspension buffer at a concentration of 800-1,200 cells/μl, and approximately 17,400 cells per channel (to give estimated recovery of 10,000 cells per channel) were loaded onto a Chromium Next GEM Chip G (10x Genomics) and processed through the Chromium controller to generate single-cell gel beads in emulsion (GEMs). snRNA-seq libraries were prepared with the Chromium NextGEM Single Cell 3′ GEM Library & Gel Bead Kit v.3.1 (10x Genomics) as per manufacturer’s instruction. Libraries from different samples were pooled and 20,000 reads per nucleus were sequenced on a NovaSeq6000 (Illumina) or a NextSeq (Illumina) with 28 bases for read 1, 91 bases for read 2 and 8 bases for index 1.

Dissociation of organoid transplants and single cell RNA-seq

Single cell dissociation from fresh dissected *in vivo* brain organoids was performed using Neural Tissue Dissociation Kit (Miltenyi Biotec, 130-092-628) as per manufacturer’s instruction. Red blood cells were lysed with Red Blood Cell Lysis Solution (Miltenyi Biotec, 130-094-183) for 3 min and washed with 0.1% BSA in 1× PBS and prepared for downstream applications. Cells were stained with PE anti GLAST antibody (Miltenyi Biotec, 130-118-483, 1:50) for 30–40 min in the dark on ice and washed with PBS and resuspended in 0.1% BSA in 1× PBS. Cells were incubated with DAPI prior to sorting. After sorting, cells were resuspended in ice-cold PBS at a concentration of 500-1,200 cells/μl and subjected to Single Cell Sequencing (10x Genomics) as described above.

Single-nucleus and Single-cell RNA-seq data analysis

The Cell Ranger 6.0.1 pipeline (10x Genomics) was used to align reads from RNA-seq to the 10x hg19 human reference genome v1.2.0 and 10x mm10 mouse reference genome v1.2.0 and produce the associated cell-by-gene count matrix for the organoid transplants. The Cell Ranger 6.0.1 pipeline (10x Genomics) was used to align reads from RNA-seq to the 10x hg19 human reference genome v1.2.0 and produce the associated cell-by-gene count matrix for the *in vitro* organoids. Default parameters were used, except for -include-introns argument for nuclei samples. Unique molecular identifier (UMI) counts were analyzed using the Seurat R package v.4.0.1[59]. Human cells or nuclei (defined as nuclei with >95% genes mapped to hg19) were kept for subsequent analysis. Nuclei with <1% of mitochondrial contamination and between 500 and 6,000 expressed genes were retained for further analysis. Cells with <20% of mitochondrial contamination and between 500 and 6,000 expressed genes were retained for further analysis. To prepare

for integration, SCTransform was performed, and the top 3000 features were used to find integration anchors. Integration was performed using the SCT normalized method. Principal component analysis (PCA) was performed on the scaled data for the variable genes and the top 30 principal components were implemented for the unsupervised clustering. Cells were clustered in PCA space using the FindNeighbors function (top 30 principal components) and FindClusters function. Variation in the cells was visualized by UMAP.

Differentially expressed genes (DEGs) were defined as genes significantly expressed (P adjusted for multiple comparisons < 0.05) in $\geqslant$25% of cell populations with >0.25-fold difference (log scale) between groups of nuclei. DEGs between clusters of astrocytes before and post TNFα treatment were identified as genes significantly expressed (P adjusted for multiple comparisons < 0.05) with >0.25-fold difference (log scale). Visualization of intersecting genes was plotted using UpSetR (v1.4.0)[60]. Gene Ontology (GO) terms of DEGs were represented using a maximum of 100 genes (Wilcoxon test, $p < 0.05$, logFC >0.25) using the Enrichr [61] database "GO_Biological_Process_2021".

Cluster correlation

For both eight-month-old organoid transplant and integrated snRNA-seq datasets, marker genes in each cluster were identified using FindAllMarkers() in Seurat, requiring to be detected in at least 25% of cells with log fold-change larger than 0.25. The top 50 marker genes from each cluster were selected by fold-change expression for the correlation analysis. The expression of top markers was averaged across cells within each cluster of our dataset and each annotated cell type in reference human brain dataset across six cortical areas from Allen Brain Atlas[48]. Pearson correlation coefficient between our dataset the reference was calculated across clusters and presented in heatmap.

Module expression analysis

To calculate differential expression of modules, the AddModuleScore function from Seurat was applied using the top 50 expressed genes from the upregulated mature astrocyte gene list curated from Zhang et al. 2016. Two-sided wilcoxon test was applied comparing the module scores in astrocytes from different time point, using the stats R package.

Weight gene coexpression network analysis

To learn patterns of coordinated gene regulation across the cells, we applied scWGCNA v0.0.0.9000 [26] to several dataset. We selected genes expressed in at least 5% of cells for downstream analysis. To construct metacell gene expression matrix, the K-Nearest Neighbors algorithm was used to identify groups of similar

cells, and then the average expression of these cells was computed using the MetacellsByGroups function. For 10-week-old organoids and eight-month-old transplants, during metacell computation, we pooled 50 cells within the same cell type per cell line to retain the metadata for scWGCNA. For the integrated datasets, we pooled 25 cells within the same cell type for each time point. We then set up the expression matrix for the cell type of interest. To pick an adequate power for each dataset, we used the TestSoftPowers function to test values from 1 to 30. We next constructed a co-expression network with the selected soft power. To compute the harmonized module eigengenes, ScaleData function was performed to regress variable features including "nFeature_RNA" and "percent.mt", and module eigengenes were calculated using the ModuleEigengenes function. Default parameter was used to compute module connectivity. To compute hub gene signature score, the top 25 hub genes by eigengene-based connectivity were used. GO terms of each module were analyzed using the top 100 hub genes using the Enrichr [61] database "GO_Biological_Process_2021".

Pseudotime analysis

To prepare cells for pseudotime analysis, the unknown cluster was first removed, and the samples were re-integrated using the SCT method in Seurat. PCA was then calculated, and the top 30 principal components was used for UMAP visualization. Pseudotime analysis was performed using the Monocle3 v.1.0.0 software package [35] with the default parameters. The cells were subset to contain an equal amount from different time points. A starting point for the trajectory was chosen manually by finding an endpoint for the earliest developmental cell type. To test cell distribution along the trajectory, a one-sided Kolmogorov–Smirnov test was applied comparing the distribution of pseudotime values of cells from different time point, using the stats R package.

Cell type and age prediction

Cell type prediction was carried out with Seurat package (v4.2.0), with the published integrated dataset as reference[59]. The reference dataset was projected onto our query data based on the anchors identified by the FindTransferAnchors function, and the label of the cell type was predicted using the TransferData function. Cells that were not assigned with any reference labels were defined as "Undetermined". The original annotation and prediction labels were presented in original UMAP space. The concordance between the original annotation and prediction was measured by calculating the assignment percentage of every type of annotated cells to the reference labels, which were then displayed in a heatmap.

For age prediction, our data were integrated with the reference age dataset [34] using CCA merge method in Seurat [59]. Within the integrated UMAP space, a KNN regression was carried out using the knn.reg function

from FNN R package (v1.1.3) with 10 nearest neighbors. Cell ages were estimated from the arcsinh transformation of the reference ages, taking the mean of its neighbors. The age distribution among different groups was compared using the Wilcoxon rank-sum test.

Enrichment analyses

Gene set enrichment analyses of Hallmark gene sets and GO terms were performed with WebGestaltR package (v0.4.4) with an FDR <0.05 as the significance threshold, protein coding genes as the reference list, a minimum number of genes in a category of 5, permutation time of 1000 [62]. To prepare the input ranked gene list for GSEA, differential expression analyses was performed between two conditions using the FindMarkers function from Seurat. Genes were scored and ordered by the resulting P values and fold changes.

Data availability

Single nucleus RNA-seq data is available in GEO under the accession number GSE185472. The following public datasets were used for snRNA-seq analysis: Allen Brain Institute human adult snRNA-seq data from multiple cortical areas (https://portal.brain-map.org/atlases-and-data/rnaseq/human-multiple-cortical-areas-smart-seq; accessed October 2022), snRNA-seq data from broad temporal coverage from fetal to adulthood stages of the Brodmann area 8, 9, 10, and 46 prefrontal cortex regions (Gene Expression Omnibus accession number GSE168408), and snRNA-seq from eight-month-old cortical organoid transplants (Gene Expression Omnibus accession number GSE190815). For single-nucleus analysis, we used hg19 human reference genome v1.2.0 and mm10 mouse reference genome v1.2.0 provided by 10X. The sequences and gene files used to build the references can be achieved at ftp://ftp.ensembl.org/pub/grch37/release-84/fasta/homo_sapiens/dna/ and ftp://ftp.ensembl.org/pub/grch37/release-84/gtf/homo_sapiens/ (for human hg19 genome); ftp://ftp.ensembl.org/pub/release-84/fasta/mus_musculus/dna/ and ftp://ftp.ensembl.org/pub/release-84/gtf/mus_musculus/ (for mouse mm10 genome). All other raw data used for plotting in the figures are provided as Source Data.

Statistics and Reproducibility

Statistical analyses were conducted using GraphPad Prism 9 and R (v4.1.2). The specific methods employed to determine significance are detailed in the figure legends. Exact statistical values are presented in the figures and the Source Data. The data presented from representative experiments were independently replicated at least three times with similar outcomes, unless explicitly indicated by the sample size noted in each figure or Method section. This includes all microscopy data and quantitative PCR data.

Methods-only References

16 Mansour, A. A. *et al.* An in vivo model of functional and vascularized human brain organoids. *Nat Biotechnol* **36**, 432-441, doi:10.1038/nbt.4127 (2018).

26 Morabito, S. *et al.* Single-nucleus chromatin accessibility and transcriptomic characterization of Alzheimer's disease. *Nat Genet* **53**, 1143-1155, doi:10.1038/s41588-021-00894-z (2021).

32 Merritt, C. R. *et al.* Multiplex digital spatial profiling of proteins and RNA in fixed tissue. *Nat Biotechnol* **38**, 586-599, doi:10.1038/s41587-020-0472-9 (2020).

33 Li, Y. *et al.* Direct labeling and visualization of blood vessels with lipophilic carbocyanine dye DiI. *Nat Protoc* **3**, 1703-1708, doi:10.1038/nprot.2008.172 (2008).

34 Herring, C. A. *et al.* Human prefrontal cortex gene regulatory dynamics from gestation to adulthood at single-cell resolution. *Cell* **185**, 4428-4447 e4428, doi:10.1016/j.cell.2022.09.039 (2022).

35 Cao, J. *et al.* The single-cell transcriptional landscape of mammalian organogenesis. *Nature* **566**, 496-502, doi:10.1038/s41586-019-0969-x (2019).

48 Hodge, R. D. *et al.* Conserved cell types with divergent features in human versus mouse cortex. *Nature* **573**, 61-68, doi:10.1038/s41586-019-1506-7 (2019).

51 Cowan, C. A. *et al.* Derivation of embryonic stem-cell lines from human blastocysts. *The New England journal of medicine* **350**, 1353-1356, doi:10.1056/NEJMsr040330 (2004).

52 Thomson, J. A. *et al.* Embryonic stem cell lines derived from human blastocysts. *Science* **282**, 1145-1147, doi:10.1126/science.282.5391.1145 (1998).

53 Mertens, J. *et al.* Differential responses to lithium in hyperexcitable neurons from patients with bipolar disorder. *Nature* **527**, 95-99, doi:10.1038/nature15526 (2015).

54 Goncalves, J. T. *et al.* In vivo imaging of dendritic pruning in dentate granule cells. *Nature neuroscience* **19**, 788-791, doi:10.1038/nn.4301 (2016).

55 Longair, M. H., Baker, D. A. & Armstrong, J. D. Simple Neurite Tracer: open source software for reconstruction, visualization and analysis of neuronal processes. *Bioinformatics* **27**, 2453-2454, doi:10.1093/bioinformatics/btr390 (2011).

56 Kuwajima, M., Mendenhall, J. M. & Harris, K. M. Large-volume reconstruction of brain tissue from high-resolution serial section images acquired by SEM-based scanning transmission electron microscopy. *Methods Mol Biol* **950**, 253-273, doi:10.1007/978-1-62703-137-0_15 (2013).

57 Deerinck, T. J., Bushong, E. A., Thor, A. & Ellisman, M. H. NCMIR methods for 3D EM: a new protocol for preparation of biological specimens for serial block face scanning electron microscopy. *Microscopy* **1**, 6-8 (2010).

58 Horstmann, H., Korber, C., Satzler, K., Aydin, D. & Kuner, T. Serial section scanning electron microscopy (S3EM) on silicon wafers for ultra-structural volume imaging of cells and tissues. *PLoS One* **7**, e35172, doi:10.1371/journal.pone.0035172 (2012).

59 Hao, Y. *et al.* Integrated analysis of multimodal single-cell data. *Cell* **184**, 3573-3587 e3529, doi:10.1016/j.cell.2021.04.048 (2021).

60 Conway, J. R., Lex, A. & Gehlenborg, N. UpSetR: an R package for the visualization of intersecting sets and their properties. *Bioinformatics* **33**, 2938-2940, doi:10.1093/bioinformatics/btx364 (2017).

61 Kuleshov, M. V. *et al.* Enrichr: a comprehensive gene set enrichment analysis web server 2016 update. *Nucleic Acids Res* **44**, W90-97, doi:10.1093/nar/gkw377 (2016).

62 Liao, Y., Wang, J., Jaehnig, E. J., Shi, Z. & Zhang, B. WebGestalt 2019: gene set analysis toolkit with revamped UIs and APIs. *Nucleic Acids Res* **47**, W199-W205, doi:10.1093/nar/gkz401 (2019).

Morphological diversification and functional maturation of human astrocytes in glia-enriched cortical organoids transplanted in the mouse brain

Meiyan Wang[1,#], Lei Zhang[1,#], Sammy Weiser Novak[2], Jingting Yu[3], Iryna S. Gallina[1], Lynne L. Xu[1], Christina K. Lim[1,5], Sarah Fernandes[1,5], Maxim N. Shokhirev[3], April E. Williams[3], Monisha D. Saxena[1], Shashank Coorapati[1], Sarah L. Parylak[1], Cristian Quintero[4], Elsa Molina[4], Leonardo R. Andrade[2], Uri Manor[2,6] and Fred H. Gage[1,*]

1. Laboratory of Genetics, The Salk Institute for Biological Studies, La Jolla, California, 92037, USA
2. Waitt Advanced Biophotonics Core, The Salk Institute for Biological Studies, La Jolla, California, 92037, USA
3. Integrative Genomics and Bioinformatics Core, The Salk Institute for Biological Studies, La Jolla, California, 92037, USA
4. Next Generation Sequencing Core, The Salk Institute for Biological Studies, La Jolla, California, 92037, USA
5. Division of Biological Sciences, University of California, San Diego, La Jolla, California, 92093, USA
6. Present address: Division of Biological Sciences, University of California, San Diego, La Jolla, California, 92093, USA

# These authors contributed equally

* Correspondence: gage@salk.edu

Abstract

Astrocytes, the most abundant glial cell type in the brain, are underrepresented in traditional cortical organoid models due to the delayed onset of cortical gliogenesis. Here, we introduce a novel glia-enriched cortical organoid model that exhibits accelerated astrogliogenesis. We demonstrated that induction of a gliogenic switch in a subset of progenitors enabled rapid derivation of astroglial cells, which account for 25-31% of the cell population within eight to ten weeks of differentiation. Intracerebral transplantation of these organoids reliably generated a diverse repertoire of cortical neurons and anatomical subclasses of human astrocytes. Spatial transcriptome profiling identified layer-specific expression patterns among distinct subclasses of astrocytes within the organoid transplants. Using an *in vivo* acute neuroinflammation model, we identified a subpopulation of astrocytes that rapidly activates proinflammatory pathways upon cytokine stimulation. Additionally, we demonstrated that CD38

signaling plays a crucial role in mediating metabolic and mitochondrial stress in reactive astrocytes. This model provides a robust platform for investigating human astrocyte function.

Main text

Astrocytes comprise the most abundant glial cell type in the human brain, and their dysfunction has been implicated in numerous neurological disorders [1]. However, our ability to elucidate the roles of astrocytes in brain development and in the pathogenesis of brain disorders has been limited by the scarcity of accessible human astrocytes in a brain environment. Brain organoid models have emerged as valuable tools for investigating human brain development and disorders, as they exhibit self-organized properties that recapitulate certain aspects of the developing human brain [2-6]. Nonetheless, current cortical brain organoid systems have limitations in efficiently generating astrocytes [7,8], mainly due to the extended time required for the progenitor cells to acquire glial competency [9]. In human cortical organoid systems, astrogliogenesis begins gradually at three months of differentiation and undergoes a maturation process lasting over a year [7]. Attempts to accelerate astrocyte differentiation from human induced pluripotent stem cells (hiPSCs) have shown promise either by transiently overexpressing a critical gliogenic factor [10,11] or by triggering a gliogenic switch with a specific set of patterning factors [12,13]. However, it remains unclear whether these patterning factors can be successfully applied to a cortical organoid patterning paradigm to generate glia-enriched cortical organoids.

Cells or organoids cultured *in vitro* also lack the blood circulation and the cortical organization of the brain. The brain is a highly vascularized organ that is connected with the systemic circulation. Astrocyte projections form glia limitans surrounding the vessels, regulating the communication between brain and circulation, and maintaining brain homeostasis [14,15]. Transplantation of human brain organoids into rodent brains enables the successful survival, integration, and formation of functional circuits of the human brain organoids *in vivo* [16-22].

In this study, we present a glia-enriched cortical organoid model that facilitates accelerated astrogliogenesis. By triggering a gliogenic switch in 28-33% of the cells in the organoids at three weeks of differentiation, we achieved efficient derivation of astroglia comprising 25-31% of the cell population by eight to ten weeks of differentiation. To investigate astrocyte function in a brain environment, we employed an intracerebral transplantation method [16] that yielded highly vascularized *in vivo* brain organoids. The organoid transplants displayed robust integration into the host brain and developed anatomically defined morphological subclasses of human astrocytes. Spatial genomics further revealed layer-specific molecular signatures among different subclasses of human astrocytes. Moreover, we observed the formation of perivascular astrocytic endfeet ensheathing the vessels within the transplants. Using single nucleus RNA-sequencing (snRNA-seq), we found advanced maturation of astrocytes in our organoid transplants compared to cortical organoid transplants. Additionally, we showed that differentially expressed genes (DEGs) associated with

acute reactivity exhibited significant heterogeneity across astrocyte subpopulations in an *in vivo* model of acute neuroinflammation. Notably, we demonstrated that the metabolic and mitochondrial stresses in reactive astrocytes were mediated through CD38 signaling and that treatment with a potent CD38 inhibitor effectively alleviated a wide range of stresses induced by inflammation in astrocytes.

Rapid astrogliogenesis in glia-enriched cortical organoids

Astrocytes, like neurons and oligodendrocytes, originate from the radial glial cells in the subventricular zone (SVZ). Because astrogliogenesis occurs late during development [9], most brain organoid models do not develop astrocytes until a very late stage. We hypothesized that triggering an early gliogenic switch in a subset of progenitors during neuroectoderm specification would enable rapid derivation of glial cells in a human cortical brain organoid model (Fig.1a and Extended Data Fig.1a). To induce an early gliogenic switch, we supplemented the neuroectoderm induction media with the previously reported gliogenic agent platelet-derived growth factor (PDGF-AA) and cultured the organoids in astrocyte medium [12,13] (Fig.1a). Organoids cultured under the gliogenic condition demonstrated robust upregulation of gliogenic factor NFIA at three weeks of differentiation (Fig.1b,c and Extended Data Fig.1b), indicating early glial patterning in a subset of progenitor cells, whereas forebrain organoids cultured under published methods [23,24] had almost no detectable NFIA expression at the same time point (Fig.1b,c). As early as eight weeks of differentiation, glia-enriched cortical organoids had substantially greater gliogenesis compared to the forebrain organoids, supported by the upregulation of astrocyte markers GFAP and HepaCAM (Fig.1d-g and Extended Data Fig.1c). In addition to astrocytes, robust neurogenesis was observed at eight weeks of differentiation (Extended Data Fig.1d). Compared to organoids cultured in a serum-free condition, glia-enriched cortical organoids cultured in differentiation media containing fetal bovine serum (FBS) displayed the most efficient derivation of astrocytes at three months of differentiation (Extended Data Fig.1e,f).

To identify cell-type diversity in glia-enriched cortical organoids, we carried out snRNA-seq on nuclei isolated from 10-week-old organoids generated from two pluripotent stem cell lines. We first applied uniform manifold approximation and projection (UMAP) dimensionality reduction and Louvain clustering to the snRNA-seq datasets, identifying multiple neuronal and glial subpopulations (Fig.1h, Extended Data Fig.2a-c, Supplementary Table 1). The majority of excitatory neurons were committed to a cortical identity, characterized by the expression of cortical neuronal markers (e.g. CTIP2, CUX2, and SATB2) (Extended Data Fig.1d and 2b-c). Astroglia comprised 25-31% of the total population; 5-8% of these were proliferating progenitor cells and 20-23% were astrocytes (Extended Data Fig. 2a-c). To contextualize early neurogenesis and gliogenesis in a systems-level framework, we applied a single-cell weighted gene coexpression network

analysis (WGCNA) [25,26]. By computing the average expression of 50 neighboring cells from each major cell type, we constructed co-expression networks for the astrocytes from the snRNA-seq dataset and identified two astrocyte gene modules (Fig.1i,j, Extended Data Fig.2d,e, Supplementary Table 2). The hub genes of astrocyte module M12 consisted of genes that function in cell-cell adhesion (TJP1, ID3, and FGFR1), and the hub genes of module M14 consisted of many known glial markers, including transcriptional factors ZBTB20 and GLI3 and glutamate transporter SLC1A3 (Fig.1k). Similarly, we constructed co-expression networks for the cortical excitatory neurons and identified four co-expression gene modules highly expressed in these cells (Extended Data Fig.2f-j, Supplementary Table 3). Collectively, transcriptomic analysis of 10-week-old glia-enriched cortical organoids confirmed robust neurogenesis and astrogliogenesis.

Protoplasmic astrocytes are the most abundant astrocyte subtypes in the gray matter and exhibit highly ramified processes [27]. Astrocyte morphogenesis depends on direct interaction with neuronal processes [28]. We hypothesized that our organoid model supports robust astrocyte morphogenesis. To study the morphological characteristics of astrocytes during organoid differentiation, we transduced glia-enriched cortical organoids with GFAP::GFP adeno associated virus (AAV) and carried out Sholl analysis and morphological analyses of virus-labeled astrocytes (Fig.1l-n). Astrocytes exhibited process-bearing morphology at three months of differentiation and displayed robustly increased branch complexity over time, such as an increased number of primary processes, number of branches, and total length of the processes (Fig.1l-n). Immunostaining confirmed that AAV-transduced astrocytes expressed many mature astrocyte markers, and their processes were closely associated with synapses (Extended Data Fig.3a-e). Furthermore, AAV-transduced astrocytes were capable of glutamate uptake (Extended Data Fig.3f). Taken together, these data indicate successful generation of functional astrocytes *in vitro*.

Formation of astrocyte morphological subclasses *in vivo*

To better mimic the endogenous microenvironment, we performed intracerebral transplantation of 8- to 10-week-old glia-enriched cortical organoids into a cavity made in the retrosplenial cortex of immunodeficient (NOD.Cg-*Prkdc*^{scid} *Il2rg*^{tm1Wjl}/SzJ or NSG) mice (Fig.2a). Glia-enriched cortical organoids exhibited robust integration into the lesion cavity (Fig.2b,c and Extended Data Fig.4a-d). Immunostaining confirmed that nearly all NeuN and GFAP expression in the transplants coincided with HuNuclei expression and human GFAP (hGFAP) expression, respectively (Extended Data Fig.4a,b), indicating that neurons and astrocytes in the transplants were derived nearly exclusively from the human organoids. Human astrocytes exhibit a notably intricate morphology in contrast to their rodent counterparts [29]. Stereotactic viral labeling of

astrocytes with GFAP::GFP AAV revealed that human astrocytes in the transplants differed from the host astrocytes in that the human protoplasmic astrocytes were far more elaborate and larger (Fig.2d,e). In addition, human protoplasmic astrocytes extended long processes to the vasculature whereas the rodent astrocytes formed rosette-like structures around the vasculature (Fig.2f). Collectively, these results suggest that human protoplasmic astrocytes maintain their characteristic species-specific features in the transplants.

Studies revealed intrinsic differences between human astrocytes and those of lower mammals [30,31], including anatomically defined subclasses of human astrocytes that are absent in rodents [29]. Besides the predominant protoplasmic astrocytes, at least three additional major morphological subclasses of $GFAP^+$ astrocytes have been identified in the adult human temporal lobe, including interlaminar astrocytes, fibrous astrocytes, and varicose projection astrocytes [29]. We identified primate-specific interlaminar astrocytes at the pial surface of the transplant-forming fibers that both contributed to the glial limitans at the pial surface and penetrated deeper layers of the transplants; we also observed abundant ramified protoplasmic astrocytes in cortical layers of the transplants and fibrous astrocytes in deep layers of the transplants adjacent to white matter (WM), with relatively unbranched, straight $GFAP^+$ processes (Fig.2c and Extended Data Fig.4e). Notably, the formation of morphological subclasses of astrocytes in the transplants was accompanied by differential expression of CD44 and S100B (Extended Data Fig.4f,g). To further explore the morphological subclasses of $GFAP^+$ astrocytes, we used GFAP::tdTomato lentiviral transduced organoids for transplantation. Viral labeling enabled the identification of far more astrocytic processes than immunohistochemistry for GFAP (Fig.2g). Viral labeling also revealed human- and higher-order primate-specific varicose projection astrocytes, characterized by long fibers with prominent varicosities (Fig.2g). Together, these results show that intracerebral transplantation creates a permissive environment for the specification of anatomically defined human astrocyte subclasses.

To decipher the molecular signatures of astrocytes across transplant layers, we next spatially profiled the expression of human protein-coding genes on formalin-fixed paraffin-embedded (FFPE) sections using the NanoString GeoMx human whole-transcriptome atlas (WTA; > 18,000 genes) assay[32] (Fig.2h). We first selected the regions of interest (ROIs) across different transplant layers (i.e., pial, cortex, and WM) and then performed segmentation of astrocytes within each ROI according to $SOX9^+$ staining (Fig.2i,j and Extended Data Fig.5a). Utilizing Principal Component Analysis (PCA), we observed separations in the gene expression profiles between layer-specific astrocytes (Fig.2k). Comparative transcriptomic analysis revealed that expression levels of many established astrocyte markers varied according to their specific locations (Fig.2l,m, Extended Data Fig.5b, and Supplementary Table 4-6). Pial interlaminar astrocytes demonstrated elevated expression levels of astrocyte markers such as Glial Fibrillary Acidic Protein

(GFAP), Aquaporin 4 (AQP4), and transcriptional repressors ID1 and ID3 (Fig.2l,m). Meanwhile, fibrous astrocytes within the WM displayed increased expression of Thrombospondin 4 (THBS4) and transcription factor HES2, and cortical gray matter (predominantly protoplasmic) astrocytes demonstrated elevated expression of Solute Carrier Family 1 Member 2 (SLC1A2), ATPase Na^+/K^+ Transporting Subunit Alpha 2 (ATP1A2), Sterol Regulatory Element Binding Transcription Factor 2 (SREBF2), and Neuroglycan C (CSPG5) (Fig.2l,m). We then carried out gene set enrichment analysis (GSEA) and identified that cortical (predominantly protoplasmic) astrocytes exhibited enrichment in genes associated with steroid metabolism, cholesterol biosynthesis, neurotransmitter release cycle, and nervous system development, highlighting their close interaction with neurons (Extended Data Fig.5c). To further explore the interactions between astrocytes and neurons, we confirmed the expression of glutamate transporter EAAT2 (gene name SLC1A2) and synaptogenic proteins HEVIN (gene name SPARCL1) in human protoplasmic astrocytes by immunostaining (Extended Data Fig.6a,b). Electron microscopy (EM) revealed the presence of multi-synaptic boutons (Extended Data Fig.6c), indicating neuronal maturation in the transplants. To investigate the physical proximity of synapses and astrocytes in the transplants, we employed serial-sectioning EM and reconstructed a dendrite with spines (Extended Data Fig.6d). We observed that the astrocytic processes were surrounding the synapse (Extended Data Fig.6e), indicating a close association of human astrocytes with synapses *in vivo*. Collectively, these findings demonstrated functional diversification of astrocyte subclasses at the molecular level.

Human astrocytes form perivascular astrocytic endfeet

In the brain, astrocytes are uniquely positioned to interact with both neurons and the vasculature. We observed an extensive host vascular network and microglia infiltrating into the transplants (Extended Data Fig.6f-i). Unlike the *in vitro* astrocytes, protoplasmic astrocytes in the transplants established spatial territory (Fig.3a,b). Astrocytic processes interact with blood vessels through cap-like cytoplasmic processes called astrocytic endfeet. Specific channels and transporters, for example AQP4 and Kir4.1, are targeted to astrocyte endfeet to control water and ion homeostasis at the vessel-neuron interface [15]. Immunostaining for the water channel protein AQP4 demonstrated polarized expression at the endfeet of the human astrocytes in the transplants, in sharp contrast to the *in vitro* astrocytes (Fig.3c). This finding was further confirmed by the expression of the inward-rectifier potassium channel Kir4.1 at the perivascular astrocyte endfeet processes and of the glucose transporter Glut-1 at the astrocyte-vessel interface (Extended Data Fig.6j,k). These results provide evidence that the *in vivo* environment facilitates formation of astrocytic endfeet structure.

We next carried out EM to transplants derived from the GFP-transduced H9 hESC line to investigate the interaction between human astrocytes and host vasculature. Blood vessels were directly labeled by trans-cardiac perfusion with a fluorescent lipophilic carbocyanine dye that incorporates into endothelial cell membranes upon contact [33] (Extended Data Fig.6l). The structure of the blood vessels was well maintained when examined under scanning EM, where tight junctions and marginal folds were clearly visible between endothelial cells (Fig.3d). Glycogen granules and intermediate filament were also found in the astrocytes surrounding the vessels (Fig.3e). We next reconstructed elements of a blood vessel and perivascular astrocytes from a three-µm segment of a capillary found near the center of the transplant using serial section EM (Fig.3f,g and Supplementary Video 1). Tight junctions were visible between endothelial cells in the electron micrograph (Extended Data Fig.6m). Astrocytic processes wrapped around the vessel and apparently covered the entire surface, suggesting the formation of glia limitans surrounding the vasculature. Together, these results demonstrate the close coupling of human astrocytes to the host vasculature.

Enhanced cell maturation in engrafted organoids

To systematically investigate neuronal and glial development and maturation, we carried out snRNA-seq on five-month-old *in vitro* organoids, five-month-old transplants, six-month-old transplants, and eight-month-old transplants from two pluripotent stem cell lines (Fig.4a). We first performed batch-correction integration and UMAP dimensionality reduction, identifying subpopulations of neuronal and glial cells (Fig.4b,c, Extended Data Fig.7a-c, and Supplementary Table 7). We next leveraged a transfer learning strategy to integrate our dataset into a published atlas of postmortem prefrontal cortex samples from individuals spanning fetal, neonatal, infancy, childhood, adolescence, and adult stages of development [34], and we estimated the cell states and their developmental stages in our organoid nuclei (Extended Data Fig.7d-g). Most organoid nuclei from five-month-old organoids aligned with fetal populations of the reference dataset (Fig.4d). Notably, with transplantation and increasing organoid age, more nuclei displayed characteristics of postnatal cells (Fig.4d), in particular upper-layer (UL) excitatory neurons, with 6.1% of ULs for the five-month organoids aligned to postnatal stages, compared with 30.2% for the five-month transplants and 94.5% for the eight-month transplants (Extended Data Fig.7h).

To determine the genes involved in astrocyte development and function, we constructed co-expression networks using astrocytes from the integrated snRNA-seq data and identified an astrocyte gene module (M5) containing genes associated with glutamate transport (Fig.4e,f, Extended Data Fig.8a,b, and Supplementary Table 8). Analysis of the harmonized module score of gene module M5 in astrocytes revealed increased expression of the module genes in the transplants compared to the *in vitro* organoids

(Fig.4g). We next curated the top 50 expressed genes from the upregulated gene list in mature human astrocytes versus fetal human astrocytes as reported in Zhang et al., 2016 [30], and we identified elevated expression of the mature human astrocyte genes in the transplants compared to the *in vitro* organoids (Fig.4h,i). To further uncover glial heterogeneity and maturity, we performed pseudotime trajectory analysis using monocle 3[35] on the integrated snRNA-seq data in glia (Fig.4j). Setting progenitors as the starting time point for astrocytes, pseudotime trajectory analysis revealed more cells towards the end point of the trajectory in the transplants, progressing from glial progenitors to astrocytes (Fig.4j). Similarly, WGCNA and pseudotime analyses of immature and mature UL excitatory neurons revealed more advanced excitatory neuronal maturation *in vivo* (Extended Data Fig.8c-g and Supplementary Table 9). Collectively, these results provide evidence that transplantation facilitates organoid maturation.

To compare the cell states of our organoid transplants with previously reported cortical organoid transplants[21], we integrated snRNA-seq data from the cortical organoid transplants into our dataset and conducted a cell-type prediction analysis. The analysis confirmed a high degree of similarity in cell-type identity between our eight-month-old organoid transplants and the eight-month-old cortical organoid transplants[21] (Fig.4k,l). We then focused on examining the distribution of astrocyte nuclei ages using the age-prediction analysis. Our differentiation paradigm supported enhanced astrocyte maturation, with 75.8% of the nuclei aligned to postnatal cells over the age of 301 days, as estimated through molecular equivalence using the brain reference dataset, compared to 56.2% of nuclei in previously reported cortical organoid transplants (Fig.4m). Overall, these data suggest that our differentiation paradigm enhances astrocyte maturation.

Characterization of proinflammatory pathways in astrocytes

Reactive astrocytes are induced by CNS injuries and diseases [36], as characterized by upregulation of genes that can modulate CNS inflammation [1,37] and formation of a glial scar after CNS trauma [38]. Despite significant progress in our understanding of this pronounced transformation process, our knowledge of astrocyte reactivity has been predominantly based on rodent cells. To investigate the reactive transformation of human astrocytes *in vivo*, we performed stereotaxic injections of either saline or recombinant human tumor necrosis factor alpha (TNFα), an inflammatory cytokine known to induce reactive astrogliosis [1,37], into the transplants, and performed fluorescence activated cell sorting to purify glial cells for single-cell RNA-seq five hours post injection (Fig.5a-c, Extended Data Fig.9a,b, and Supplementary Table 10). We found that differentially expressed genes (DEGs) associated with acute reactivity exhibited significant heterogeneity across astrocyte subpopulations (Fig.5d,e and Extended Data Fig.9c,d). Following TNFα

treatment, we observed a significant expansion of cluster 2 astrocytes, which were identified by their expression of CD44, CD38, and GFAP (Fig.5c,f). These reactive astrocytes were characterized by genes that have been previously linked to proinflammatory pathways and astrocyte pathogenic activities in neurotoxicity, such as the activation of NF-κB and interferon pathways (Fig.5g and Extended Data Fig.9e). We also observed downregulation of genes involved in oxidative phosphorylation, NADH dehydrogenase complex assembly, and mitochondrial respiratory chain complex assembly in cluster 2 astrocytes following TNFα treatment (Fig.5g and Extended Data Fig.9f). Taken together, our findings indicate that there is significant reactive heterogeneity across different human astrocyte subpopulations *in vivo*.

CD38 mediates inflammation-induced stresses in astrocytes

To gain further insights into the cellular changes that occur during human astrocyte reactivity, we treated glia-enriched cortical organoids with TNFα for 24 hours and examined the inflammatory processes following the treatment (Fig.6a,b and Extended Data Fig.10a,b). Our results confirmed a rapid upregulation of pro-inflammatory cytokines, interferon signaling, and the NF-κB signaling pathway (Fig.6b and Extended Data Fig.10a,b). We also observed NF-κB nuclear translocation in astrocytes (Fig.6c). These results demonstrate that *in vitro* astrocytes can recapitulate the molecular changes *in vivo*.

Transcriptomics suggests dysregulation of metabolism and mitochondrial function in reactive astrocytes (Fig.5g and Extended Data Fig.9f). To investigate changes in NAD^+ metabolism and mitochondrial function in reactive astrocytes, we purified GFAP::tdTomato$^+$ astrocytes from *in vitro* organoids (Fig.6d and Extended Data Fig.10c). Our analysis revealed reduced NAD^+/NADH ratio (Fig.6e) and glutathione (reduced to oxidized or GSH/GSSH) ratio (Fig.6f) in astrocytes following TNFα treatment, suggesting metabolic stress and oxidative stress in reactive astrocytes. CD38 is a major regulator of NAD^+ levels and a gradual increase in CD38 has been implicated in the decline of NAD^+ with age [39]. We observed significant upregulation of CD38 in reactive astrocytes (Extended Data Fig.10d). We next investigated whether CD38 mediated the reductive metabolic stress and oxidative stress. After treating human astrocytes with TNFα and a potent CD38 inhibitor 78c, we found significantly reduced metabolic and oxidative stress (Fig.6e,f). Cellular stress and metabolic cues can cause the mitochondrial network to fragment, which then promotes mitophagy and is associated with cell death [40]. Reactive astrocytes showed significant increases in mitochondrial fragmentation, which was markedly reduced by 78c (Fig.6g,h). These results suggest a mechanism by which a major NADase CD38 mediates metabolic and mitochondrial dysregulation in reactive astrocytes.

Discussion

While brain organoid models have been useful for studying human neurodevelopment and neurological disorders, studies of astrocyte function in such models have remained limited. This is partly due to the late onset of gliogenesis in humans, which is recapitulated in cortical organoid models [7]. Prolonged culture of neural progenitor cells in media containing gliogenic factors [12,13] or repeated passaging [41,42] confers gliogenic competency but eliminates neurogenic potentials. In this study, we demonstrate that induction of a gliogenic switch by addition of a gliogenic factor PDGF-AA and astrocyte-supporting medium for three weeks successfully enables accelerated astrogliogenesis in a substantial portion of cells while retaining neurogenic potential for the majority of cells. In this context, our organoid model not only efficiently generates astrocytes in a time window comparable to previously reported 2D astrocyte differentiation protocols[10-13] but also gives rise to other brain cell types, including cortical excitatory neurons, inhibitory neurons, and OPCs (Supplementary Fig.1). Additionally, transcriptomic analysis revealed that astrocytes generated in our model exhibit enhanced maturation compared to those derived from cortical organoids [21] when transplanted into rodent cortices. Therefore, our organoid model provides an opportunity to study human astrocyte function in neurodevelopment and neurological diseases.

Human astrocytic complexity correlates with the increased functional competence of the adult human brain [29,31]. In the human brain, astrocytes display a remarkable morphological diversity according to cortical layers and form anatomically defined subclasses [29,31]. While neonatal engraftment of human glial progenitor cells has allowed the progressive expansion of human glial cells in the host brain [43-45], to the best of our knowledge, it is still limited in fully reproducing the morphological complexity observed in the human brain. Notably, our model is capable of producing hominid-specific varicose astrocytes, a feature that was not observed in previous models. Our study has also uncovered the diversification of layer-specific expression patterns in astrocytes by spatial transcriptome profiling. Pial interlaminar astrocytes within the transplants expressed many astrocyte markers, including GFAP, S100B, CD44, and AQP4, and showed increased expression of GFAP, AQP4, ID1, and ID3 compared to cortical astrocytes, resembling the expression profiles of subpial astrocytes observed in mice [46,47] and interlaminar astrocytes reported in humans [48,49]. In contrast, cortical protoplasmic astrocytes displayed an upregulation of genes involved in regulating cholesterol biosynthesis, synapse formation, and synaptic activity, while fibrous astrocytes expressed genes involved in initiation of myelination. These findings contribute to our understanding of the unique molecular processes governing the spatial organization of astrocytes within the cortical architecture. Of note, the NanoString GeoMx platform used in this study did not permit discrete identification of gene expression variations at single cell resolution. This lack of single cell resolution represents a notable

constraint in our analysis, where regions of interest, although enriched for SOX9, encompass various astrocytic types, thereby limiting our capacity to delineate transcriptional distinctions at a more refined morphological level.

Our model also provides a platform to study astrocyte function during neuroinflammation and disease progression. The previous notion of astrocyte reactivity being a uniform response to tissue damage has been challenged by accumulating evidence suggesting that astrocytes are a diverse population of cells [36,50]. Our findings show that transcriptional changes associated with acute astrocyte reactivity *in vivo* are highly heterogeneous among human astrocyte subpopulations. We also demonstrate that metabolic and mitochondrial stresses induced by inflammation can be alleviated through inhibiting cyclase/hydrolase activity of CD38, a major NADase expressed in a subset of astrocytes and upregulated in response to TNFα treatment. This model thus presents a platform to interrogate cellular function under physiological conditions that is otherwise difficult to investigate in other models and for drug discovery to treat human brain diseases.

Acknowledgments

We thank A.Mansour for providing the pCSC-CAG-GFP lentiviral labeled H9 ESC line, N. Hah for technical assistance with snRNA-seq, and R.Garg for assistance with EM segmentation. We also thank M.L. Gage for editorial comments, and A. Cao and T. Bartol for their help with 3DEM visualization. This work was supported by the American Heart Association and the Paul G. Allen Frontiers Group Grant #19PABHI34610000/TEAM LEADER: Fred H. Gage/2019, JPB Foundation, Annette C. Merle-Smith, Lynn and Edward Streim, the Milky Way Foundation, the Ray and Dagmar Dolby Family Fund, and NIH R37 AG072502-03, P30 AG062429-05, P30 AG068635-04, R01 AG070154-04, AG056306-07, P01 AG051449-08. This work was also supported by the NGS Core Facility, the GT3 Core Facility, the Razavi Newman Integrative Genomics and Bioinformatics Core Facility, and the Waitt Advanced Biophotonics Core Facility of the Salk Institute with funding from NIH-NCI CCSG: P30 014195, the Chapman Foundation, NINDS R24 Core Grant, and funding from NEI, and the Waitt Foundation. M.W. is supported by a NARSAD Young Investigator Grant from Brain & Behavior Research Foundation (BBRFNARSAD) and a Pioneer Fund Postdoctoral Scholar Award from the Salk Institute. Fig.2a, 2h, 4a, 5a, 6a and 6d were created with BioRender.com.

Author Contributions Statement

M.W., L.Z., and F.H.G. conceived the study and wrote the manuscript; M.W., L.Z., C.K.L. and S.F. performed cell culture and organoid differentiation; M.W., L.Z., C.K.L. and I.S.G. performed surgeries; S.L.P. assisted in surgeries; M.W. and I.S.G. performed single nucleus RNA-seq and single cell RNA-seq; M.W., C.Q., and E.M. performed NanoString GeoMx DSP; M.W., M.S., J.Y., and A.W. performed bioinformatics analyses; M.W. and L.Z. performed imaging analysis with assistance from L.L.X., C.K.L., S.C. and M.D.S.; L.Z., S.W.N. and L.A. performed sample processing for scanning electron microscopy; S.W.N. and L.A. performed electron microscopic image analysis under the supervision of M.W., L.Z. and U.M.; F.H.G. provided funding.

Competing interests Statement

The authors declare no competing interests.

Figure Legends

Figure 1. Enhanced astrogliogenesis in glia-enriched cortical organoids.

a. Differentiation protocol schematic: astrocyte medium (AstroM); fetal bovine serum (FBS). **b.** Immunostaining for glial progenitors (NFIA, magenta) and stem cells (SOX2, green). Scale bars, 20 μm. **c.** Quantification of $NFIA^+$ cells in forebrain (gray bars; Hues6 n=9; iPSC822 n=7) or glia-enriched cortical organoids (red bars; Hues6 n=7; iPSC822 n=6) from two batches of differentiation. Each dot represents one organoid. Mean ± s.e.m. Two-sided t-test with Welch's correction. ***$p < 0.001$. **d.** Immunostaining for astrocytes (GFAP, magenta) and progenitor cells (SOX2, green). Scale bars, 20 μm. **e.** $GFAP^+$ area quantified in forebrain (gray bars; Hues6 n=10; iPSC822 n= 9) and glia-enriched cortical organoids (red bars; Hues6 n=9; iPSC822 n= 8) from two batches of differentiation. Each dot represents one organoid. Mean ± s.e.m. Two-sided t-test with Welch's correction. ***$p < 0.001$, **$p < 0.01$. **f.** Immunostaining for astrocytes (HepaCAM, magenta; GFAP, green). Scale bars, 20 μm. **g.** $HepaCAM^+$ area quantified in forebrain (gray bars; Hues6 n=5; iPSC822 n= 6) and glia-enriched cortical organoids (red bars; Hues6 n=6; iPSC822 n= 7) from two batches of differentiation. Each dot represents one organoid. Mean ± s.e.m. Two-sided t-test with Welch's correction. **$p < 0.01$. **h.** UMAP plot displaying snRNA-seq data (n= 15,287 nuclei) from 10-week-old organoids from two lines after batch correction. APC (astrocyte progenitor cell), Ast (astrocyte), IPC (intermediate progenitor cell), In (inhibitory neuron), Cortical Ex (cortical excitatory neuron), and Ex (excitatory neuron). **i.** Dendrogram from WGCNA of astrocyte gene modules. **j.** UMAP plot of module hub gene expression score for astrocyte gene modules M12 and M14. **k.** Coexpression plots of the top 25 module genes for astrocyte gene modules M12 and M14. **l.** Confocal images of the GFAP::GFP AAV-transduced astrocytes and traces of processes. Top, three-month-old organoids. Bottom, five-month-old organoids. Scale bars, 20 μm. **m.** Sholl analysis of astrocytes (three-month-old, 33 astrocytes; five-month-old, 59 astrocytes). Mean ± s.e.m. **n.** Bar plots illustrating the number of primary processes, number of branches, and total process length (three-month-old, 33 astrocytes; five-month-old, 59 astrocytes). Mean ± s.e.m. Two-sided t-test with Welch's correction. ****$p < 0.0001$.

Figure 2. Human astrocytes form anatomically defined morphological subclasses *in vivo*.

a. Illustration depicting the experimental procedure. **b.** Immunostaining for H9-GFP-derived transplant (GFP, green) and nuclei (DAPI, blue). **c.** Immunostaining of six-month-old transplants: astrocytes (GFAP, green), human nuclear antigen (HuNu, magenta). Top inset, interlaminar astrocytes; Middle inset, protoplasmic astrocytes; Bottom inset, fibrous astrocytes. Scale bars, 100 μm (left panel), 50 μm (right panels). **d.** Immunostaining of GFAP::GFP AAV-transduced astrocytes: human nuclear antigen (HuNu, cyan), astrocytes (GFAP, magenta). Top, human astrocytes; Bottom, mouse astrocytes. Scale bars, 20 μm. **e.** Maximal diameter comparison of GFAP::GFP AAV-transduced human and mouse cortical astrocytes.

Mouse, n = 30 from three mice; human, n = 46 from three transplants. Mean ± s.e.m. Two-sided t-test with Welch's correction. ****$p < 0.0001$. **f.** Immunostaining for human [top; $hGFAP^+$ (magenta) and $GFAP^+$ (green)] and mouse astrocytes [bottom; $hGFAP^-$ (magenta) and $GFAP^+$ (green)] and blood vessels (Ly6C, cyan). Scale bars, 20 μm. **g.** GFAP::tdTomato lentivirus-labeled human astrocytes in transplants (tdTomato, magenta). Arrowheads: varicosities in astrocyte processes. Scale bars, 20 μm. **h.** Overview of the GeoMx Digital Spatial Profiler (DSP) workflow. **i.** Immunofluorescent staining image of one brain section with overlying selected Regions of Interest (ROIs). Scale bar, 750 μm. 38 ROIs (pial = 10, cortex = 16, WM = 12) from 4 sections were analyzed. **j.** Top: immunofluorescent staining: hGFAP (yellow), SOX9 (magenta), SYTO-13 (blue); bottom: cell segmentation of $SOX9^+$/$CYTO\text{-}13^+$ cells within ROI. Scale bar, 100 μm. **k.** PCA plot of GeoMx DSP gene expression data. Points: segmented $SOX9^+$/$CYTO\text{-}13^+$ cells per ROI, colored by location. **l.** Volcano plots of differentially expressed genes (DEGs) between astrocyte groups. Dashed lines: adjusted p value < 0.05 (linear mixed effect model with Benjamini-Hochberg multiple correction) and fold change (FC) >1.5. **m.** Box plots depicting the normalized expression levels of selected genes in each group (pial = 10, cortex = 16, WM = 12). Center line, median; box limits, upper and lower quartiles; whiskers, 1.5x interquartile range; points, outliers.

Figure 3. Human astrocytes form perivascular endfeet *in vivo*.

a. Confocal images comparing *in vitro* glia-enriched cortical organoids (top, six-month-old) and organoid transplants (bottom, six-month-old). Immunostaining for human astrocytes (hGFAP, green). Scale bars, 100 μm. **b.** Quantification of the number of $hGFAP^+$ cells per mm^2 in glia-enriched cortical organoids *in vitro* (left) and transplants *in vivo* (right). n = 6 organoids *in vitro* and n = 4 transplants (*in vivo*). Two-sided t-test with Welch's correction, *** $P < 0.001$. Bars, mean ± s.e.m. **c.** Confocal images comparing glia-enriched cortical organoids *in vitro* (left panels, six-month-old) and transplants *in vivo* (right panels, six-month-old). Immunostaining for human astrocytes (hGFAP, green) and water channel Aquaporin 4 (AQP4, magenta). Scale bars, 20 μm. **d.** Electron micrograph of the lumen of a blood vessel in an eight-month-old transplant captured using a scanning electron microscope. Top panel: endothelial cells (purple), basement membrane (blue), and intercellular leaflets (yellow). Bottom panel: enlarged view from the top panel. Scale bars, 4 μm. **e.** Electron micrograph of a capillary in the transplant. Boxes show astrocyte processes. Top right, arrowheads indicate glycogen granules. Bottom right, an arrowhead indicates glia filaments (GFAP). M, mitochondria. Scale bars, 1 μm. **f-g.** Electron micrograph of a capillary consists of endothelial cells (purple), tight junctions (yellow), pericytes (brown), and basement membrane (blue). The vessel was wrapped by astrocytic processes (green). Astrocyte soma (light green). 3D reconstruction of segmented data from serial section EM (**f**). Pseudocolored 2D image (**g**). Scale bars, 2 μm.

Figure 4. Advanced maturation of astrocytes in engrafted organoids revealed by snRNA-seq analyses. **a.** Schematic representation of snRNA-seq and related analyses. **b.** UMAP plot of snRNA-seq data (n= 65,743 nuclei) from five-month-old glia-enriched cortical organoids (5m_Org, n= 17,490 nuclei), 5-month-old transplants (5m_T, n= 15,936 nuclei), six-month-old transplants (6m_T, n= 15,607 nuclei), and eight-month-old transplants (8m_T, n= 16,710 nuclei) from two lines after batch correction. Ast, astrocyte; OPC, oligodendrocyte progenitor cell; In, inhibitory neuron; Immature, immature excitatory neuron; DL, deep layer cortical excitatory neuron; UL, upper layer cortical excitatory neuron. **c.** UMAP plots of snRNA-seq data separated by individual samples. **d.** Ridge plot of predicted nuclei ages separated by time point. Wilcoxon test (two-sided, ****, $p < 0.0001$; reference group, 5m_Org). **e.** Coexpression plot of top 25 module hub genes. **f.** UMAP plot of module hub gene expression score for astrocyte modules M5. **g.** Violin plot of harmonized module score of astrocyte module M5 in astrocytes across different time points. Wilcoxon test (two-sided, ****, $p < 0.0001$; reference group, 5m_Org). Center line, median; box limits, upper and lower quartiles; whiskers, 1.5x interquartile range; points, outliers. **h.** Module expression score of mature astrocyte genes curated from Zhang et al., 2016 in astrocytes separated by each time point. Each dot represents median value per cell line. Wilcoxon test (two-sided, ****, $p < 0.0001$; reference group, 5m_Org). **i.** Dot plot showing the expression of selected mature astrocyte genes reported in Zhang et al., 2016. **j.** UMAP dimensionality reduction of astrocytes from the integrated snRNA-seq. Each cell is colored by its pseudotime trajectory assignment. Pseudotime analysis separated by time point. One-sided Kolmogorov–Smirnov test (****, $p < 2.2e-16$; reference group, 5m_Org). **k.** Projection of cortical organoid transplants snRNA-seq nuclei (Revah et al., 2022 right) onto the reference of nuclei (8m_T, left). **l.** Heatmap of predicted cell type of cortical organoid transplants (Revah et al., 2022) on to the reference nuclei (8m_T). **m.** Ridge plot of predicted ages of astrocyte nuclei from eight-month-old glia-enriched cortical organoid transplants (8m_T) and cortical organoid transplants (Revah et al., 2022). Wilcoxon test (two-sided, ****, P value = 2.613246e-75).

Figure 5. Transcriptome profiling reveals rapid activation of proinflammatory pathways in a subpopulation of astrocytes *in vivo*.

a. Schematic representation of the experimental design. **b.** UMAP plot of scRNA-seq data from saline-treated transplants (n = 7404 cells) and TNFα-treated transplants (n = 5835 cells) after batch correction. **c.** UMAP plot displaying all Seurat clusters (left) and the number of cluster 2 astrocytes in each condition. UpSetR plots showing the upregulated DEGs (**d**) and downregulated DEGs (**e**) that are unique to or shared between astrocyte clusters 1-4. **f.** Violin plot illustrating the expression of selected genes in astrocyte clusters 1-4. **g.** GSEA comparing TNFα-treated and saline-treated cluster 2 astrocytes. Hallmark gene sets are shown. FDR, false discovery rate; NES, normalized enrichment score.

Figure 6. CD38 mediates inflammation-induced metabolic and mitochondrial stresses in human astrocytes.

a. Schematic representation of the experimental design. **b.** Confocal images of *in vitro* six-month-old glia-enriched cortical organoids at different time points (day 0, day 1, and day 2) post TNFα treatment. Immunostaining for astrocytes (GFAP, green) and monocyte chemoattractant protein-1 (CCL2, magenta). Scale bars, 200 μm. **c.** Quantification of the percentage of astrocytes with nuclear translocation of NF-κB (three organoids per group). Each dot represents one organoid. Bars, mean ± SD. Two-sided t-test, **$p < 0.01$, ****$p < 0.0001$. **d.** Schematic representation of astrocyte purification process from organoids. **e.** Dot plot showing the ratio of NAD^+ to NADH (n = 8 independent experiments per group). Each dot represents one independent experiment. Bars, mean ± SD. Two-sided t-test, ****$p < 0.0001$. **f.** Dot plot showing the ratio of GSSH to GSSG (n = 6 independent experiments per group). Each dot represents one independent experiment. Bars, mean ± SD. Two-sided t-test, ****$p < 0.0001$. **g.** Confocal images of astrocytes treated with saline, TNFα, and TNFα together with CD38 inhibitor 78c. Immunostaining for astrocytes (GFAP::tdTomato, magenta) and mitochondria (mitoGFP, green). Scale bars, 10 μm. **h.** Percentage of astrocytes with fragmented mitochondria (CTRL = 150 cells examined over three independent experiments; TNFα1d = 150 cells examined over three independent experiments; TNFα2d = 150 cells examined over three independent experiments; TNFα2d + CD38i = 200 cells examined over four independent experiments). Each dot represents one independent experiment. Bars, mean ± SD. Two-sided t-test, **$p < 0.01$, ****$p < 0.0001$.

References

1 Liddelow, S. A. *et al.* Neurotoxic reactive astrocytes are induced by activated microglia. *Nature* **541**, 481-487, doi:10.1038/nature21029 (2017).

2 Qian, X., Song, H. & Ming, G. L. Brain organoids: advances, applications and challenges. *Development* **146**, doi:10.1242/dev.166074 (2019).

3 Wang, M., Zhang, L. & Gage, F. H. Modeling neuropsychiatric disorders using human induced pluripotent stem cells. *Protein Cell* **11**, 45-59, doi:10.1007/s13238-019-0638-8 (2020).

4 Lancaster, M. A. *et al.* Cerebral organoids model human brain development and microcephaly. *Nature* **501**, 373-379, doi:10.1038/nature12517 (2013).

5 Kim, J., Koo, B. K. & Knoblich, J. A. Human organoids: model systems for human biology and medicine. *Nat Rev Mol Cell Biol* **21**, 571-584, doi:10.1038/s41580-020-0259-3 (2020).

6 Velasco, S. *et al.* Individual brain organoids reproducibly form cell diversity of the human cerebral cortex. *Nature* **570**, 523-527, doi:10.1038/s41586-019-1289-x (2019).

7 Sloan, S. A. *et al.* Human Astrocyte Maturation Captured in 3D Cerebral Cortical Spheroids Derived from Pluripotent Stem Cells. *Neuron* **95**, 779-790 e776, doi:10.1016/j.neuron.2017.07.035 (2017).

8 Qian, X. *et al.* Sliced Human Cortical Organoids for Modeling Distinct Cortical Layer Formation. *Cell Stem Cell* **26**, 766-781 e769, doi:10.1016/j.stem.2020.02.002 (2020).

9 Molofsky, A. V. *et al.* Astrocytes and disease: a neurodevelopmental perspective. *Genes Dev* **26**, 891-907, doi:10.1101/gad.188326.112 (2012).

10 Tchieu, J. *et al.* NFIA is a gliogenic switch enabling rapid derivation of functional human astrocytes from pluripotent stem cells. *Nat Biotechnol* **37**, 267-275, doi:10.1038/s41587-019-0035-0 (2019).

11 Canals, I. *et al.* Rapid and efficient induction of functional astrocytes from human pluripotent stem cells. *Nat Methods* **15**, 693-696, doi:10.1038/s41592-018-0103-2 (2018).

12 Santos, R. *et al.* Differentiation of Inflammation-Responsive Astrocytes from Glial Progenitors Generated from Human Induced Pluripotent Stem Cells. *Stem Cell Reports* **8**, 1757-1769, doi:10.1016/j.stemcr.2017.05.011 (2017).

13 Barbar, L. *et al.* CD49f Is a Novel Marker of Functional and Reactive Human iPSC-Derived Astrocytes. *Neuron* **107**, 436-453 e412, doi:10.1016/j.neuron.2020.05.014 (2020).

14 Zhang, J. & Liu, Q. Cholesterol metabolism and homeostasis in the brain. *Protein Cell* **6**, 254-264, doi:10.1007/s13238-014-0131-3 (2015).

15 Daneman, R. & Prat, A. The blood-brain barrier. *Cold Spring Harb Perspect Biol* **7**, a020412, doi:10.1101/cshperspect.a020412 (2015).

16 Mansour, A. A. *et al.* An in vivo model of functional and vascularized human brain organoids. *Nat Biotechnol* **36**, 432-441, doi:10.1038/nbt.4127 (2018).

17 Bao, Z. *et al.* Human Cerebral Organoid Implantation Alleviated the Neurological Deficits of Traumatic Brain Injury in Mice. *Oxid Med Cell Longev* **2021**, 6338722, doi:10.1155/2021/6338722 (2021).

18 Daviaud, N., Friedel, R. H. & Zou, H. Vascularization and Engraftment of Transplanted Human Cerebral Organoids in Mouse Cortex. *eNeuro* **5**, doi:10.1523/ENEURO.0219-18.2018 (2018).

19 Kitahara, T. *et al.* Axonal Extensions along Corticospinal Tracts from Transplanted Human Cerebral Organoids. *Stem Cell Reports* **15**, 467-481, doi:10.1016/j.stemcr.2020.06.016 (2020).

20 Shi, Y. *et al.* Vascularized human cortical organoids (vOrganoids) model cortical development in vivo. *PLoS Biol* **18**, e3000705, doi:10.1371/journal.pbio.3000705 (2020).

21 Revah, O. *et al.* Maturation and circuit integration of transplanted human cortical organoids. *Nature* **610**, 319-326, doi:10.1038/s41586-022-05277-w (2022).

22 Jgamadze, D. *et al.* Structural and functional integration of human forebrain organoids with the injured adult rat visual system. *Cell Stem Cell* **30**, 137-152 e137, doi:10.1016/j.stem.2023.01.004 (2023).

23 Qian, X. *et al.* Generation of human brain region-specific organoids using a miniaturized spinning bioreactor. *Nat Protoc* **13**, 565-580, doi:10.1038/nprot.2017.152 (2018).
24 Qian, X. *et al.* Brain-Region-Specific Organoids Using Mini-bioreactors for Modeling ZIKV Exposure. *Cell* **165**, 1238-1254, doi:10.1016/j.cell.2016.04.032 (2016).
25 Langfelder, P. & Horvath, S. WGCNA: an R package for weighted correlation network analysis. *BMC Bioinformatics* **9**, 559, doi:10.1186/1471-2105-9-559 (2008).
26 Morabito, S. *et al.* Single-nucleus chromatin accessibility and transcriptomic characterization of Alzheimer's disease. *Nat Genet* **53**, 1143-1155, doi:10.1038/s41588-021-00894-z (2021).
27 Allen, N. J. & Eroglu, C. Cell Biology of Astrocyte-Synapse Interactions. *Neuron* **96**, 697-708, doi:10.1016/j.neuron.2017.09.056 (2017).
28 Stogsdill, J. A. *et al.* Astrocytic neuroligins control astrocyte morphogenesis and synaptogenesis. *Nature* **551**, 192-197, doi:10.1038/nature24638 (2017).
29 Oberheim, N. A. *et al.* Uniquely hominid features of adult human astrocytes. *J Neurosci* **29**, 3276-3287, doi:10.1523/JNEUROSCI.4707-08.2009 (2009).
30 Zhang, Y. *et al.* Purification and Characterization of Progenitor and Mature Human Astrocytes Reveals Transcriptional and Functional Differences with Mouse. *Neuron* **89**, 37-53, doi:10.1016/j.neuron.2015.11.013 (2016).
31 Oberheim, N. A., Wang, X., Goldman, S. & Nedergaard, M. Astrocytic complexity distinguishes the human brain. *Trends Neurosci* **29**, 547-553, doi:10.1016/j.tins.2006.08.004 (2006).
32 Merritt, C. R. *et al.* Multiplex digital spatial profiling of proteins and RNA in fixed tissue. *Nat Biotechnol* **38**, 586-599, doi:10.1038/s41587-020-0472-9 (2020).
33 Li, Y. *et al.* Direct labeling and visualization of blood vessels with lipophilic carbocyanine dye DiI. *Nat Protoc* **3**, 1703-1708, doi:10.1038/nprot.2008.172 (2008).
34 Herring, C. A. *et al.* Human prefrontal cortex gene regulatory dynamics from gestation to adulthood at single-cell resolution. *Cell* **185**, 4428-4447 e4428, doi:10.1016/j.cell.2022.09.039 (2022).
35 Cao, J. *et al.* The single-cell transcriptional landscape of mammalian organogenesis. *Nature* **566**, 496-502, doi:10.1038/s41586-019-0969-x (2019).
36 Sofroniew, M. V. & Vinters, H. V. Astrocytes: biology and pathology. *Acta Neuropathol* **119**, 7-35, doi:10.1007/s00401-009-0619-8 (2010).
37 Zamanian, J. L. *et al.* Genomic analysis of reactive astrogliosis. *J Neurosci* **32**, 6391-6410, doi:10.1523/JNEUROSCI.6221-11.2012 (2012).
38 Anderson, M. A. *et al.* Astrocyte scar formation aids central nervous system axon regeneration. *Nature* **532**, 195-200, doi:10.1038/nature17623 (2016).
39 Tarrago, M. G. *et al.* A Potent and Specific CD38 Inhibitor Ameliorates Age-Related Metabolic Dysfunction by Reversing Tissue NAD(+) Decline. *Cell Metab* **27**, 1081-1095 e1010, doi:10.1016/j.cmet.2018.03.016 (2018).
40 Sprenger, H. G. & Langer, T. The Good and the Bad of Mitochondrial Breakups. *Trends Cell Biol* **29**, 888-900, doi:10.1016/j.tcb.2019.08.003 (2019).
41 Krencik, R. & Zhang, S. C. Directed differentiation of functional astroglial subtypes from human pluripotent stem cells. *Nat Protoc* **6**, 1710-1717, doi:10.1038/nprot.2011.405 (2011).
42 Palm, T. *et al.* Rapid and robust generation of long-term self-renewing human neural stem cells with the ability to generate mature astroglia. *Sci Rep* **5**, 16321, doi:10.1038/srep16321 (2015).
43 Han, X. *et al.* Forebrain engraftment by human glial progenitor cells enhances synaptic plasticity and learning in adult mice. *Cell Stem Cell* **12**, 342-353, doi:10.1016/j.stem.2012.12.015 (2013).
44 Windrem, M. S. *et al.* A competitive advantage by neonatally engrafted human glial progenitors yields mice whose brains are chimeric for human glia. *J Neurosci* **34**, 16153-16161, doi:10.1523/JNEUROSCI.1510-14.2014 (2014).
45 Mariani, J. N., Zou, L. & Goldman, S. A. Human Glial Chimeric Mice to Define the Role of Glial Pathology in Human Disease. *Methods Mol Biol* **1936**, 311-331, doi:10.1007/978-1-4939-9072-6_18 (2019).

46 Zeisel, A. *et al.* Brain structure. Cell types in the mouse cortex and hippocampus revealed by single-cell RNA-seq. *Science* **347**, 1138-1142, doi:10.1126/science.aaa1934 (2015).
47 Bayraktar, O. A. *et al.* Astrocyte layers in the mammalian cerebral cortex revealed by a single-cell in situ transcriptomic map. *Nat Neurosci* **23**, 500-509, doi:10.1038/s41593-020-0602-1 (2020).
48 Hodge, R. D. *et al.* Conserved cell types with divergent features in human versus mouse cortex. *Nature* **573**, 61-68, doi:10.1038/s41586-019-1506-7 (2019).
49 Jorstad, N. L. *et al.* Transcriptomic cytoarchitecture reveals principles of human neocortex organization. *Science* **382**, eadf6812, doi:10.1126/science.adf6812 (2023).
50 Burda, J. E. *et al.* Divergent transcriptional regulation of astrocyte reactivity across disorders. *Nature* **606**, 557-564, doi:10.1038/s41586-022-04739-5 (2022).

Methods

Human pluripotent stem cells

Human embryonic stem cells (hESCs) Hues6 (NIH approved ESC line, obtained from HSCI iPS Core) [51], H9 (Wisconsin International Stem Cell (WISC) bank, WiCell research Institute, WA09 cells) [52] and human induced pluripotent cells (hiPSCs) 822 were used in the current study. H9 cells were transduced with pCSC-CAG-GFP lentiviruses and GFP-expressing cells were FACS-sorted as previously described [16]. Protocols were previously approved by the Salk Institutional Review Board and informed consent was obtained from the subjects.

Mice

All animal experiments described in the current study were approved by the Institutional Animal Care and Use Committee (IACUC) at the Salk Institute for Biological Studies (12-00022) and were conducted in compliance with the National Institute of Health's Guide for the Care and Use of Laboratory Animals. Immune-deficient mice NOD.Cg-*Prkdc*^{scid} *Il2rg*^{tm1Wjl}/SzJ (Jackson Laboratory, stock number 005557) were generated in our lab by breeding and kept on a 12h light/dark cycle in a housing group of two to five mice in each cage. Male and female mice 6-12 weeks of age were randomly used in this study.

Human pluripotent stem cell culture

Human pluripotent stem cells (PSCs) were cultured as previously described [16,53]. PSC colonies were maintained on Matrigel-coated six-well plates (Matrigel, Corning, 354277, hESC-Qualified) using mTeSR Plus (Stemcell Technologies, 85850) and were incubated in a 5% CO_2 humidified atmosphere at 37°C. PSC colonies were passaged at a ratio of 1:6 every three to six days using ReLeSR (Stemcell technologies, 5872). All human PSCs were maintained in feeder-free culture condition for 20-40 generations and confirmed negative for mycoplasma. Cells were confirmed normal with karyotyping. All experiments involving cells from human subjects were performed in compliance with the institutional Embryonic Stem Cell Research Oversight (ESCRO) committee.

Generation of glia-enriched cortical organoids

To generate embryoid bodies (EBs), intact PSC colonies were treated with 1 mg/ml Collagenase type IV (Invitrogen, 17104-019) for 20-45 minutes at 37 °C and mechanically detached with a cell scraper. Dissociated colonies were maintained in an ultra-low-attachment dish (Nunc) under stationary conditions for two days and were fed with mTeSR Plus supplemented with 10mM ROCK inhibitor Y-27632 (Tocris, 1254). From day 1, cells were maintained in Astrocyte medium (AM) (ScienCell, 1800) supplemented with

Astrocyte Growth Supplement (AGS, Sciencell, 1800), 2% Fetal Bovine Serum, 500 ng/ml Noggin (R&D Systems, 6057-NG), 10 ng/mL PDGFAA (Proteintech, HZ-1215) and 1x 2-Mercaptoethanol (Gibco, 21985032) until day 14. On day 15, organoids (10-12 organoids in each well of six-well ultra-low-attachment plates) were transferred on to an orbital shaker (75 r.p.m.) and maintained in AM supplemented with AGS, 10 ng/ml PDGFAA, and 1x 2-Mercaptoethanol for an additional week. From day 22, organoids were maintained on orbital shaker (75 r.p.m.) in medium consisting of DMEM/F-12 with Glutamax (Thermo Fisher Scientific, 10565018), 1 x N2 supplement (Thermo Fisher Scientific, 17502-048), 1x B27 (without RA) (Thermo Fisher Scientific, 12587010), 1x MEM-NEAA (Thermo Fisher Scientific, 11140050), 10% Fetal Bovine Serum (Omega Scientific Cat#FB-01; Lot#991851), and 1x 2-Mercaptoethanol. Organoids cultured beyond day 60 were additionally supplemented with 20 ng/ml BDNF (R&D Systems, 248-BDB), 20 ng/ml GDNF (R&D Systems, 212-GD), 0.2 mM Ascorbic Acid (Stemcell Technologies, 72132), 0.5 mM cAMP (Tocris, 1141). All media changes were done every other day. All organoids for transplantation experiments were pre-selected for development of organized neuroepithelium budding and absence of cyst formation. In addition, organoids from the same culture batch were examined by immunostaining for verification of neuronal and glial differentiation.

Intracerebral implantation of glia-enriched cortical organoids

Organoid implantations were performed as previously described [16]. Glia-enriched organoids were cultured *in vitro* for 8 to 10 weeks prior to implantation. Mice were anesthetized with 3-5% isoflurane inhalation for induction and 1-2% isoflurane for maintenance. Each animal was fixed onto a stereotaxic frame for the duration of all surgical procedures with body temperatures maintained at 37 °C using a water-circulation heating pad (Gaymar Industries). Dexamethasone (2.5 mg/kg) was injected subcutaneously to minimize edema. Upon the removal of the skin above the scalp, a ~3mm diameter craniotomy was performed by drilling into the skull. The underlying dura mater was subsequently removed with forceps. A unilateral lesion was created in the region of the retrosplenial cortex through aspiration with a blunt-tip needle attached to a vacuum line. The brain tissue overlying the anterior colliculus was removed and the vascular bed of the choroidal fissure was exposed. Sterile saline and a piece of Gelfoam (Pfizer) were used to prevent excessive bleeding. The organoid transplant was placed on the pial vessels overlying the collicles caudal to the hippocampus. Upon transplantation, the organoid was sealed with a 5-mm glass coverslip using adhesive glue and the wound was secured with dental cement (Stoelting) [54]. Upon completion of the surgery, carprofen (5 mg/kg, i.p., 100 µl of 1 mg/ml) and Buprenorphine SR-Lab (1.0 mg/kg, subcutaneous) were administered to minimize inflammation and pain. The mice were then returned to their home cages for recovery on a heating pad.

Stereotaxic injection

Mice were anesthetized with 3-5% isoflurane via inhalation for induction and 1-2% isoflurane for maintenance. Each mouse was fixed onto a stereotaxic frame for the duration of all surgical procedures with body temperatures maintained at 37 °C using a water-circulation heating pad (Gaymar Industries). For direct TNFα injection into brain organoids, the preexisting dental cement and cranial window were removed first, followed by injection of 1µl of 250 ng of recombinant human TNFα (Sino Biological Inc, 10602-HNAE) or saline at a speed of 1µl per minute using a Hamilton syringe. The 1µl injection volume was split across two different Z locations. After the injection was completed, the needle was retracted at a rate of 0.2–0.5 mm per minute. A new cranial window was placed using adhesive glue and secured with dental cement (Stoelting). Buprenorphine SR-Lab (1.0 mg/kg, subcutaneous) was administered to minimize postoperative pain. The mice were immediately placed on a warm heating pad until recovery.

Virus transduction

pBOB-GFAP-tdTomato lentiviral vector was obtained from the lab of Dr. Inder Verma at the Salk Institute. Lentiviruses were produced by the virus core in Salk Institute. To transduce organoids, 1 µl of lentivirus (titer was10^12 GC/ml) was added in each well of a six-well plate containing 3 ml medium and four to six organoids. Virus-containing medium was completely changed after two days.

pAAV.GFAP.eGFP.WPRE.hGH AAV5 viral prep was a gift from James M. Wilson (Addgene viral prep # 105549-AAV5; RRID:Addgene_105549 with a titer of 10^13 GC/ml. AAV particles were injected into the mouse brain to visualize human and mouse astrocytes. Briefly, a mouse with organoid implant was anesthetized with isoflurane (5% for induction and 2% for maintenance). The mouse was fixed on the stereotaxic instrument and the glass coverslip covering the implant was drilled through. One µl AAV5 virus was slowly injected into the organoid transplant for a duration of 5 min. The mice were allowed to recover on a heating pad and returned to their home cages.

Histological processing

In vitro cultured organoids were fixed in 4% paraformaldehyde (PFA) for 45-60 minutes followed by three washings with PBS. Organoids were then transferred to 30% sucrose solution at 4°C overnight. Four to six organoids were transferred into blocks in tissue-freezing medium, frozen on dry ice, and stored at -80°C.

To obtain brain tissues containing organoid implants, the mice were first deeply anesthetized with Ketamine/xylazine (130 mg/kg, 15 mg/kg; i.p.) and then subjected to transcardial perfusion of 15ml ice saline followed by 15 ml 4% PFA. The brains were subsequently dissected out and transferred into 15-ml conical tubes containing 4% PFA for post-fixation overnight at 4°C. Brains were cryoprotected for 48-72

hr in 30% sucrose with 0.05% NaN3 at 4°C. Each brain was trimmed coronally and embedded in tissue-freezing medium (GeneralData).

All blocks were left to equilibrate to the temperature of the cryostat ~30 min prior to sectioning. Thirty 40-µm cryosections of organoids were obtained using a cryostat (Leica), mounted on Superfrost plus slides (Thermo Scientific, Menzel-Glaser), dried at RT for 30 min and stored at -20°C. For each section set, one section was collected onto a slide to obtain a total of 20 slides and this collection method was repeated until tissue was exhausted.

Immunohistochemistry and imaging acquisition

Immunofluorescence staining was performed with thawed slides, with the tissue area and slide edges outlined using a hydrophobic PAP pen. The slides were washed three times with PBS and blocked and permeabilized in blocking solution (5% normal donkey serum, 0.1% Triton X-100 in PBS) in a humidified chamber for 1h at RT. Organoid slides were incubated with primary antibodies diluted in the blocking solution at 4°C overnight. Primary antibodies used were anti-NFIA (rabbit, ab41851, Abcam; 1:250), anti-SOX2 (rat, 14-9811-82, clone#Btjce, Invitrogen; 1:400), anti-GFAP (rabbit, Z0334, Dako; 1:500), anti-GFAP (chicken, AB5541, EMD Millipore; 1:1000), anti-GFP (chicken, GFP-1020, Aves lab;1:1000), anti-hGFAP (mouse, Y40420, clone# not provided by vendor, TaKaRa; 1:500), anti-Human Nuclear Antigen (HuNu) (mouse, ab215755, clone#235-1, Abcam; 1:250), anti-NeuN (rabbit, ABN78, EMD Millipore; 1:250), anti-Ly6C (rat, ab15627,Clone# ER-MP20, Abcam; 1:500), anti-Aquaporin 4 (AQP4) (rabbit, AQP-004, Alomone Labs; 1:400), anti-Kir4.1 (rabbit, APC-035, Alomone Labs; 1:250), anti-glucose transporter GLUT1 (rabbit, ab115730, Abcam; 1:100), anti-tdTomato (rabbit, 600-401-379, Rockland; 1:500), anti-Laminin (rabbit, NB300-144SS, Novus a biotechne brand; 1:500), anti-hHepaCAM (mouse, MAB4108, clone#419305, R&D Systems; 1:400), anti-S100B (rabbit, ab52642, Abcam; 1:1000), anti-TBR2/Eomes (rabbit, ab275960, Abcam; 1:250), anti-CTIP2 (rat, ab18465, clone# 25B6, Abcam; 1:200), anti-SATB2 (rabbit, ab92446, Abcam;1:100), anti-HOPX (mouse, sc-398703, clone# E-1, Santa Cruz; 1:200), anti-NG2 (rabbit, AB5320, EMD Millipore; 1:200), anti-CD31 (goat, AF3628, R&D Systems; 1:500), anti-IBA1 (rabbit, 019-19741, Wako; 1:400), anti-IBA1 (goat, ab48004, Abcam; 1:400), anti-SV2 (mouse, SV2-c, clone# not provided by vendor, DSHB; 1:500), anti-PSD95 (rabbit, 51-6900, Invitrogen; 1:250), anti-Myelin Basic protein (MBP) (rabbit, ab218011, Abcam; 1:400), anti-CD44 (rat, MAB6127, clone # IM7.8.1R, R&D Systems; 1:500), anti-EAAT2 (mouse, sc-365634, clone# E-1, Santa Cruz; 1:250), anti-hSPARC-like 1 (HEVIN) (goat, AF2728, R&D Systems; 1:50), anti-PDGFRa (rabbit, ab203491, Abcam; 1:200), anti-hCD38 (mouse, MAB2404, clone# 240742, R&D Systems; 1:200), anti-CXCL10/IP10 (rabbit, MA5-32674, Invitrogen; 1:200), anti-CCL2/MCP-1 (rabbit, NBP1-07035, Novus a biotechne brand; 1:100), and anti-Connexin 43 (rabbit, 3512S, Cell Signaling Technology; 1:200). After

three washes with PBS, slides were incubated with the appropriate fluorochrome-conjugated secondary antibodies diluted in blocking solution at RT for 1h in the dark. Alexa Fluor secondary antibodies (Jackson ImmunoResearch) diluted in blocking solution at 1:250 were used. Finally, all slides were counterstained with DAPI (1 μg/ml, D9542; Sigma) for 5 min, rinsed three times in PBS before mounting with mounting solution (ProLong gold, Thermo Fisher Scientific) and left to dry for at least 48 hours at RT before imaging acquisition. Slides were stored at 4°C.

All images were acquired on a Zeiss LSM880 confocal microscope, Olympus VS-120 Virtual Slide Scanning Microscope (Olympus), or Revolve (ECHO), and processed with Zen software (Zeiss) and ImageJ software (NIH).

NanoString GeoMx Digital Spatial Profiler

Formalin-fixed paraffin-embedded (FFPE) tissue from a mouse brain with human organoid transplant was sectioned at 5μm and mounted onto positively charged slides with four sections per slide; subsequently it was profiled utilizing a NanoString GeoMx Digital Spatial Profiler (NanoString Technologies) as previously described[32]. The NanoString commercial Human Whole Transcriptome Atlas (GeoMx WTA) panel (>18,000 protein-coding genes) was selected. Tissue morphology was visualized using fluorescent-conjugated hGFAP Alexa-Fluor-594 (STEM123, TaKaRa, conjugated using Lightning-Link Rapid Alexa Fluor 594 Antibody Labeling Kit, 8μg/ml), SOX9 Alexa Fluor-647 (clone EPR14335, ab196184, abcam, 8μg/ml), and SYTO-13 to detect nucleic acids. The slide was scanned on a NanoString GeoMx DSP platform and individual regions of interest (ROIs) with a maximum diameter of 660μm were created. Once each ROI was compartmentalized, cell segmentation was performed to identify $SOX9^{+}$/$CYTO\text{-}13^{+}$ cells for subsequent ultraviolet-cleaved indexing oligonucleotides collection into a 96-well plate. Libraries were prepared according to the manufacturer's instructions (protocol MAN-10153-03). Samples were sequenced on the Illumina MiniSeq platform (MiniSeq High Output Kit PE 75 cycles) and reads were digitally quantified and normalized using GeoMx DSP Data Analysis Suite 3.0 (NanoString Technologies) following the manufacturer's instructions [32]. Target filtering was applied to retain gene targets with read counts above the limit of quantification [LOQ; defined as geomean (NegProbe) × geoSD $(\text{NegProbe})^2$ for each ROI] in at least 10% of ROIs. Q3 normalization was applied to the filtered ROIs and gene targets. The ROIs were categorized according to the spatial groups for subsequent analysis. Differential gene expression across groups was analyzed using a linear mixed effect model followed by the Benjamini-Hochberg multiple correction test. Differentially expressed genes (DEGs) were defined as fold-change > 1.5 or < -1.5, and adjusted $p < 0.05$. The parameters chosen for Gene Set Enrichment Analysis included a minimum coverage

of 20% of genes within the pathway and a pathway size between 15 and 500 genes, employing Reactome Version Build 78 + NCBI_08122021.

Cytokine Stimulation *in vitro*

Organoids or purified astrocytes were treated with 50 ng/mL recombinant human TNFα (Sino Biological Inc, 10602-HNAE) or PBS (vehicle) for 24 hours in maturation media. After washing with PBS, the samples were changed to fresh maturation media. To assess the effect of CD38 inhibition, samples were treated with 0.5 µM 78c (Tocris Bioscience, 6391) and 50 ng/mL TNFα for 24 hours in maturation media, followed by 0.5µM 78c for an additional 24 hours.

Mitochondrial Morphological Analysis

Purified astrocytes were transduced with a lentiviral vector encoding MitoEGFP under the CAG promoter. Cells were fixed in 4% paraformaldehyde for 10 minutes and washed for three times with PBS and subjected to immunohistochemistry and imaging acquisition. The EGFP signal (MitoEGFP) was used to analyze the mitochondrial shape in Image J (NIH).

Functional Assays

Reduced (GSH) and oxidized (GSSG) glutathione contents were assessed in astrocytes using the GSH/GSSG-Glo assay kit (Promega, V6611). The results are expressed as GSH/GSSG ratio. The NAD^+/NADH ratio was assessed in cultured astrocytes using the NAD-Glo assay kit (Promega, G9071).

Glutamate Uptake Assay

Astrocytes purified from three iPSC lines of five-month-old organoids and cultured neural progenitor cells (NPCs) were incubated in Hank's balanced salt solution (HBSS) buffer without calcium and magnesium (GIBCO) for 30 minutes, followed by incubation for 2 hours in HBSS containing calcium and magnesium (GIBCO) supplemented with 100 µM glutamate. After 2 hours, the media were collected and analyzed using a bioluminescent assay kit (Promega, Glutamate-Glo™ Assay, J7021) according to the manufacturer's instructions. Six to eight technical replicates per line were utilized.

Sholl analysis

GFAP::GFP AAV transduced astrocytes from three-month-old and five-month-old glia-enriched cortical organoids were stained with an antibody against GFP and imaged using a Zeiss LSM880 confocal microscope at 63x magnification with z-stack images. Images were opened in ImageJ and a maximum

intensity projection was performed. Astrocyte tracing was done manually using Simple Neurite Tracer tool [55]. Sholl analysis was carried out through Simple Neurite Tracer with radial intervals of 1.26732 µm.

Quantitative polymerase chain reaction

Total RNA was purified from organoids or astrocytes with a Direct-zol RNA Purification Kit (Zymo Research, R2061), according to the manufacturer's instructions. cDNA was synthesized using SuperScript III First-Strand Synthesis System (Invitrogen). Quantitative PCR was performed using SYBR Green PCR Master Mix (Applied Biosystems) on a BioRad CFX384 thermal cycler. The relative mRNA abundance of target genes was normalized to that of GAPDH mRNA obtained in the same sample. The primer sequences are shown in Supplementary Table 11.

Electron microscopy

A mouse with an implanted organoid was perfused and processed for electron microscopy as described elsewhere [56] with some modifications. The mouse was first anesthetized with ketamine/xylazine (130 mg/kg, 15 mg/kg; i.p.) and perfused with a 25 mL of warm oxygenated Ringers solution, followed by 15 mL of warm buffered fixative (2.5% glutaraldehyde, 2% paraformaldehyde, 3 mM $CaCl_2$, 0.15 M sodium cacodylate) with DiI added to the solution to fluorescently label vasculature as previously described [33]. The brain was carefully extracted from the skull and stored overnight at 4°C in fresh fixative solution. The following day, the brain was thoroughly rinsed with buffer (3 mM $CaCl_2$, 0.15 M sodium cacodylate) and 120-µm thick sections containing the organoid were collected using a vibrating blade microtome (Leica VT1000 S) with a bath of ice-cold buffer. Brain sections were serially rinsed with ice-cold buffer, followed by a rinse with ice-cold buffer containing 50 mM glycine. Sections were immersed in a shallow dish filled with ice-cold buffer and photographed using a dissecting microscope equipped with a camera (Olympus). Low resolution confocal imaging was performed for GFP and DiI. A small rectangle was microdissected from the center of the organoid for serial section scanning electron microscopy (S3EM). Sections used for scanning electron microscopy (SEM) were left intact for processing. Samples were processed for high contrast with heavy metals as described elsewhere [57]. Briefly, sections were immersed in buffered reduced osmium (1.5% osmium tetroxide, 1.5% potassium ferrocyanide, 3 mM $CaCl_2$, 0.15 M sodium cacodylate) for 45 minutes in the dark at RT. Samples were then serially rinsed with ice-cold distilled water before 30 minutes of treatment with filtered 1% aqueous thiocarbohydrazide that was prepared at 60°C for an hour before use. Samples were serially rinsed with ice-cold distilled water before amplifying staining with 1.5% aqueous osmium tetroxide for 45 minutes in the dark at RT. Sections to be imaged by SEM were set aside at this point for serial dehydration and critical point drying (Leica CPD300). The remaining microdissected samples were serially rinsed with ice-cold water before staining overnight with 1% uranyl acetate at 4°C.

The next day, samples were thoroughly rinsed with RT distilled water and stained with Walton's lead aspartate for 30 min at 60°C. Samples were rinsed again with RT distilled water and serially dehydrated in ice-cold ethanol. Samples were then rinsed three times in anhydrous ethanol prior to serial infiltration with Eponate 12 resin (hard formulation) over the course of two days and finally embedded in capsules (TAAB) for polymerization in a small oven for three days at 60°C.

A ribbon of approximately 100 serial ultrathin sections was collected, and each section of approximate dimensions of 150 µm-400 µm-70 nm (x-y-z) was collected onto a silicon chip using Diatome diamond knives mounted on a Leica UC7 ultramicrotome as described elsewhere [58]. The chip was mounted on an aluminum stub using carbon sticky tape and loaded into a Zeiss Sigma VP scanning EM equipped with a Gatan backscattered electron detector and both SmartSEM (Zeiss) and Atlas5 (Fibics) control software. A region of interest (ROI) near the center of the organoid implant was identified and images were acquired with an accelerating voltage of 1.5 kV, a 20-µm aperture, at a working distance of 9 mm. A multi-resolution map of a central section was acquired, identifying candidate blood vessels for further 3D analysis. Contiguous high-resolution images (8-8-70 nm/voxels x-y-z) of a representative ROI containing a blood vessel were assembled into a series of 8-bit tiff files. Serial images were aligned using AlignEM-SWiFT to form a continuous 3D representation of the tissue volume.

Endothelial cell processes, a pericyte, and astrocyte processes contacting the blood vessel as well as tight junctions and basement membrane were identified by their ultrastructural characteristics and annotated using VAST Lite software. Cells and nuclei were exported using the VAST Lite Matlab toolkit as .obj files, which were imported into Blender software equipped with GAMer and Neuromorph add-ons. Object meshes were processed with GAMer to optimize geometry for visualization, before superimposition with 3DEM data using Neuromorph. In this fashion, data were interrogated and rendered scenes and animations were produced using Blender. For video figures, rendered scenes were assembled into .avi files using ImageJ, post-processed using After Effects (Adobe), and compressed using Handbrake (https://handbrake.fr/).

Dissociation of brain organoids and single nucleus RNA-seq

Nuclei extraction from fresh dissected *in vivo* brain organoids was performed according to a demonstrated protocol CG000124 (Rev E, nuclei isolation from cell suspensions and tissues for single cell RNA sequencing) from 10x Genomics with minor modification. Briefly, freshly dissected *in vivo* brain organoids were pooled and lysed using a Dounce homogenizer in 1 ml of freshly prepared cold lysis buffer (TrisHCl pH 7.4 10 mM, NaCl 10 mM, $MgCl_2$ 3 mM, NP-40 0.1% in nucleus free water). Nuclei were centrifuged

at 500 g for 8 min and supernatant was discarded. Nuclei were then resuspended in freshly prepared cold nuclei wash & resuspension buffer (PBS, 1%BSA, Rnase inhibitor 0.2 U/µl) and filtered through a 35-µm strainer (Corning). Nuclei were centrifuged at 500 g for 5 minutes and resuspended again in nuclei wash and resuspension buffer for a total of two washes. After the second wash, nuclei were resuspended in ice-cold nuclei wash and resuspension buffer at a concentration of 800-1,200 cells/µl, and approximately 17,400 cells per channel (to give estimated recovery of 10,000 cells per channel) were loaded onto a Chromium Next GEM Chip G (10x Genomics) and processed through the Chromium controller to generate single-cell gel beads in emulsion (GEMs). snRNA-seq libraries were prepared with the Chromium NextGEM Single Cell 3′ GEM Library & Gel Bead Kit v.3.1 (10x Genomics) as per manufacturer’s instruction. Libraries from different samples were pooled and 20,000 reads per nucleus were sequenced on a NovaSeq6000 (Illumina) or a NextSeq (Illumina) with 28 bases for read 1, 91 bases for read 2 and 8 bases for index 1.

Dissociation of organoid transplants and single cell RNA-seq

Single cell dissociation from fresh dissected *in vivo* brain organoids was performed using Neural Tissue Dissociation Kit (Miltenyi Biotec, 130-092-628) as per manufacturer’s instruction. Red blood cells were lysed with Red Blood Cell Lysis Solution (Miltenyi Biotec, 130-094-183) for 3 min and washed with 0.1% BSA in 1× PBS and prepared for downstream applications. Cells were stained with PE anti GLAST antibody (Miltenyi Biotec, 130-118-483, 1:50) for 30–40 min in the dark on ice and washed with PBS and resuspended in 0.1% BSA in 1× PBS. Cells were incubated with DAPI prior to sorting. After sorting, cells were resuspended in ice-cold PBS at a concentration of 500-1,200 cells/µl and subjected to Single Cell Sequencing (10x Genomics) as described above.

Single-nucleus and Single-cell RNA-seq data analysis

The Cell Ranger 6.0.1 pipeline (10x Genomics) was used to align reads from RNA-seq to the 10x hg19 human reference genome v1.2.0 and 10x mm10 mouse reference genome v1.2.0 and produce the associated cell-by-gene count matrix for the organoid transplants. The Cell Ranger 6.0.1 pipeline (10x Genomics) was used to align reads from RNA-seq to the 10x hg19 human reference genome v1.2.0 and produce the associated cell-by-gene count matrix for the *in vitro* organoids. Default parameters were used, except for -include-introns argument for nuclei samples. Unique molecular identifier (UMI) counts were analyzed using the Seurat R package v.4.0.1[59]. Human cells or nuclei (defined as nuclei with >95% genes mapped to hg19) were kept for subsequent analysis. Nuclei with <1% of mitochondrial contamination and between 500 and 6,000 expressed genes were retained for further analysis. Cells with <20% of mitochondrial contamination and between 500 and 6,000 expressed genes were retained for further analysis. To prepare

for integration, SCTransform was performed, and the top 3000 features were used to find integration anchors. Integration was performed using the SCT normalized method. Principal component analysis (PCA) was performed on the scaled data for the variable genes and the top 30 principal components were implemented for the unsupervised clustering. Cells were clustered in PCA space using the FindNeighbors function (top 30 principal components) and FindClusters function. Variation in the cells was visualized by UMAP.

Differentially expressed genes (DEGs) were defined as genes significantly expressed (P adjusted for multiple comparisons < 0.05) in $\geqslant$25% of cell populations with >0.25-fold difference (log scale) between groups of nuclei. DEGs between clusters of astrocytes before and post TNFα treatment were identified as genes significantly expressed (P adjusted for multiple comparisons < 0.05) with >0.25-fold difference (log scale). Visualization of intersecting genes was plotted using UpSetR (v1.4.0)[60]. Gene Ontology (GO) terms of DEGs were represented using a maximum of 100 genes (Wilcoxon test, $p < 0.05$, logFC >0.25) using the Enrichr [61] database "GO_Biological_Process_2021".

Cluster correlation

For both eight-month-old organoid transplant and integrated snRNA-seq datasets, marker genes in each cluster were identified using FindAllMarkers() in Seurat, requiring to be detected in at least 25% of cells with log fold-change larger than 0.25. The top 50 marker genes from each cluster were selected by fold-change expression for the correlation analysis. The expression of top markers was averaged across cells within each cluster of our dataset and each annotated cell type in reference human brain dataset across six cortical areas from Allen Brain Atlas[48]. Pearson correlation coefficient between our dataset the reference was calculated across clusters and presented in heatmap.

Module expression analysis

To calculate differential expression of modules, the AddModuleScore function from Seurat was applied using the top 50 expressed genes from the upregulated mature astrocyte gene list curated from Zhang et al. 2016. Two-sided wilcoxon test was applied comparing the module scores in astrocytes from different time point, using the stats R package.

Weight gene coexpression network analysis

To learn patterns of coordinated gene regulation across the cells, we applied scWGCNA v0.0.0.9000 [26] to several dataset. We selected genes expressed in at least 5% of cells for downstream analysis. To construct metacell gene expression matrix, the K-Nearest Neighbors algorithm was used to identify groups of similar

cells, and then the average expression of these cells was computed using the MetacellsByGroups function. For 10-week-old organoids and eight-month-old transplants, during metacell computation, we pooled 50 cells within the same cell type per cell line to retain the metadata for scWGCNA. For the integrated datasets, we pooled 25 cells within the same cell type for each time point. We then set up the expression matrix for the cell type of interest. To pick an adequate power for each dataset, we used the TestSoftPowers function to test values from 1 to 30. We next constructed a co-expression network with the selected soft power. To compute the harmonized module eigengenes, ScaleData function was performed to regress variable features including "nFeature_RNA" and "percent.mt", and module eigengenes were calculated using the ModuleEigengenes function. Default parameter was used to compute module connectivity. To compute hub gene signature score, the top 25 hub genes by eigengene-based connectivity were used. GO terms of each module were analyzed using the top 100 hub genes using the Enrichr [61] database "GO_Biological_Process_2021".

Pseudotime analysis

To prepare cells for pseudotime analysis, the unknown cluster was first removed, and the samples were re-integrated using the SCT method in Seurat. PCA was then calculated, and the top 30 principal components was used for UMAP visualization. Pseudotime analysis was performed using the Monocle3 v.1.0.0 software package [35] with the default parameters. The cells were subset to contain an equal amount from different time points. A starting point for the trajectory was chosen manually by finding an endpoint for the earliest developmental cell type. To test cell distribution along the trajectory, a one-sided Kolmogorov–Smirnov test was applied comparing the distribution of pseudotime values of cells from different time point, using the stats R package.

Cell type and age prediction

Cell type prediction was carried out with Seurat package (v4.2.0), with the published integrated dataset as reference[59]. The reference dataset was projected onto our query data based on the anchors identified by the FindTransferAnchors function, and the label of the cell type was predicted using the TransferData function. Cells that were not assigned with any reference labels were defined as "Undetermined". The original annotation and prediction labels were presented in original UMAP space. The concordance between the original annotation and prediction was measured by calculating the assignment percentage of every type of annotated cells to the reference labels, which were then displayed in a heatmap.

For age prediction, our data were integrated with the reference age dataset [34] using CCA merge method in Seurat [59]. Within the integrated UMAP space, a KNN regression was carried out using the knn.reg function

from FNN R package (v1.1.3) with 10 nearest neighbors. Cell ages were estimated from the arcsinh transformation of the reference ages, taking the mean of its neighbors. The age distribution among different groups was compared using the Wilcoxon rank-sum test.

Enrichment analyses

Gene set enrichment analyses of Hallmark gene sets and GO terms were performed with WebGestaltR package (v0.4.4) with an FDR <0.05 as the significance threshold, protein coding genes as the reference list, a minimum number of genes in a category of 5, permutation time of 1000 [62]. To prepare the input ranked gene list for GSEA, differential expression analyses was performed between two conditions using the FindMarkers function from Seurat. Genes were scored and ordered by the resulting P values and fold changes.

Data availability

Single nucleus RNA-seq data is available in GEO under the accession number GSE185472. The following public datasets were used for snRNA-seq analysis: Allen Brain Institute human adult snRNA-seq data from multiple cortical areas (https://portal.brain-map.org/atlases-and-data/rnaseq/human-multiple-cortical-areas-smart-seq; accessed October 2022), snRNA-seq data from broad temporal coverage from fetal to adulthood stages of the Brodmann area 8, 9, 10, and 46 prefrontal cortex regions (Gene Expression Omnibus accession number GSE168408), and snRNA-seq from eight-month-old cortical organoid transplants (Gene Expression Omnibus accession number GSE190815). For single-nucleus analysis, we used hg19 human reference genome v1.2.0 and mm10 mouse reference genome v1.2.0 provided by 10X. The sequences and gene files used to build the references can be achieved at ftp://ftp.ensembl.org/pub/grch37/release-84/fasta/homo_sapiens/dna/ and ftp://ftp.ensembl.org/pub/grch37/release-84/gtf/homo_sapiens/ (for human hg19 genome); ftp://ftp.ensembl.org/pub/release-84/fasta/mus_musculus/dna/ and ftp://ftp.ensembl.org/pub/release-84/gtf/mus_musculus/ (for mouse mm10 genome). All other raw data used for plotting in the figures are provided as Source Data.

Statistics and Reproducibility

Statistical analyses were conducted using GraphPad Prism 9 and R (v4.1.2). The specific methods employed to determine significance are detailed in the figure legends. Exact statistical values are presented in the figures and the Source Data. The data presented from representative experiments were independently replicated at least three times with similar outcomes, unless explicitly indicated by the sample size noted in each figure or Method section. This includes all microscopy data and quantitative PCR data.

Methods-only References

16 Mansour, A. A. *et al.* An in vivo model of functional and vascularized human brain organoids. *Nat Biotechnol* **36**, 432-441, doi:10.1038/nbt.4127 (2018).

26 Morabito, S. *et al.* Single-nucleus chromatin accessibility and transcriptomic characterization of Alzheimer's disease. *Nat Genet* **53**, 1143-1155, doi:10.1038/s41588-021-00894-z (2021).

32 Merritt, C. R. *et al.* Multiplex digital spatial profiling of proteins and RNA in fixed tissue. *Nat Biotechnol* **38**, 586-599, doi:10.1038/s41587-020-0472-9 (2020).

33 Li, Y. *et al.* Direct labeling and visualization of blood vessels with lipophilic carbocyanine dye DiI. *Nat Protoc* **3**, 1703-1708, doi:10.1038/nprot.2008.172 (2008).

34 Herring, C. A. *et al.* Human prefrontal cortex gene regulatory dynamics from gestation to adulthood at single-cell resolution. *Cell* **185**, 4428-4447 e4428, doi:10.1016/j.cell.2022.09.039 (2022).

35 Cao, J. *et al.* The single-cell transcriptional landscape of mammalian organogenesis. *Nature* **566**, 496-502, doi:10.1038/s41586-019-0969-x (2019).

48 Hodge, R. D. *et al.* Conserved cell types with divergent features in human versus mouse cortex. *Nature* **573**, 61-68, doi:10.1038/s41586-019-1506-7 (2019).

51 Cowan, C. A. *et al.* Derivation of embryonic stem-cell lines from human blastocysts. *The New England journal of medicine* **350**, 1353-1356, doi:10.1056/NEJMsr040330 (2004).

52 Thomson, J. A. *et al.* Embryonic stem cell lines derived from human blastocysts. *Science* **282**, 1145-1147, doi:10.1126/science.282.5391.1145 (1998).

53 Mertens, J. *et al.* Differential responses to lithium in hyperexcitable neurons from patients with bipolar disorder. *Nature* **527**, 95-99, doi:10.1038/nature15526 (2015).

54 Goncalves, J. T. *et al.* In vivo imaging of dendritic pruning in dentate granule cells. *Nature neuroscience* **19**, 788-791, doi:10.1038/nn.4301 (2016).

55 Longair, M. H., Baker, D. A. & Armstrong, J. D. Simple Neurite Tracer: open source software for reconstruction, visualization and analysis of neuronal processes. *Bioinformatics* **27**, 2453-2454, doi:10.1093/bioinformatics/btr390 (2011).

56 Kuwajima, M., Mendenhall, J. M. & Harris, K. M. Large-volume reconstruction of brain tissue from high-resolution serial section images acquired by SEM-based scanning transmission electron microscopy. *Methods Mol Biol* **950**, 253-273, doi:10.1007/978-1-62703-137-0_15 (2013).

57 Deerinck, T. J., Bushong, E. A., Thor, A. & Ellisman, M. H. NCMIR methods for 3D EM: a new protocol for preparation of biological specimens for serial block face scanning electron microscopy. *Microscopy* **1**, 6-8 (2010).

58 Horstmann, H., Korber, C., Satzler, K., Aydin, D. & Kuner, T. Serial section scanning electron microscopy (S3EM) on silicon wafers for ultra-structural volume imaging of cells and tissues. *PLoS One* **7**, e35172, doi:10.1371/journal.pone.0035172 (2012).

59 Hao, Y. *et al.* Integrated analysis of multimodal single-cell data. *Cell* **184**, 3573-3587 e3529, doi:10.1016/j.cell.2021.04.048 (2021).

60 Conway, J. R., Lex, A. & Gehlenborg, N. UpSetR: an R package for the visualization of intersecting sets and their properties. *Bioinformatics* **33**, 2938-2940, doi:10.1093/bioinformatics/btx364 (2017).

61 Kuleshov, M. V. *et al.* Enrichr: a comprehensive gene set enrichment analysis web server 2016 update. *Nucleic Acids Res* **44**, W90-97, doi:10.1093/nar/gkw377 (2016).

62 Liao, Y., Wang, J., Jaehnig, E. J., Shi, Z. & Zhang, B. WebGestalt 2019: gene set analysis toolkit with revamped UIs and APIs. *Nucleic Acids Res* **47**, W199-W205, doi:10.1093/nar/gkz401 (2019).

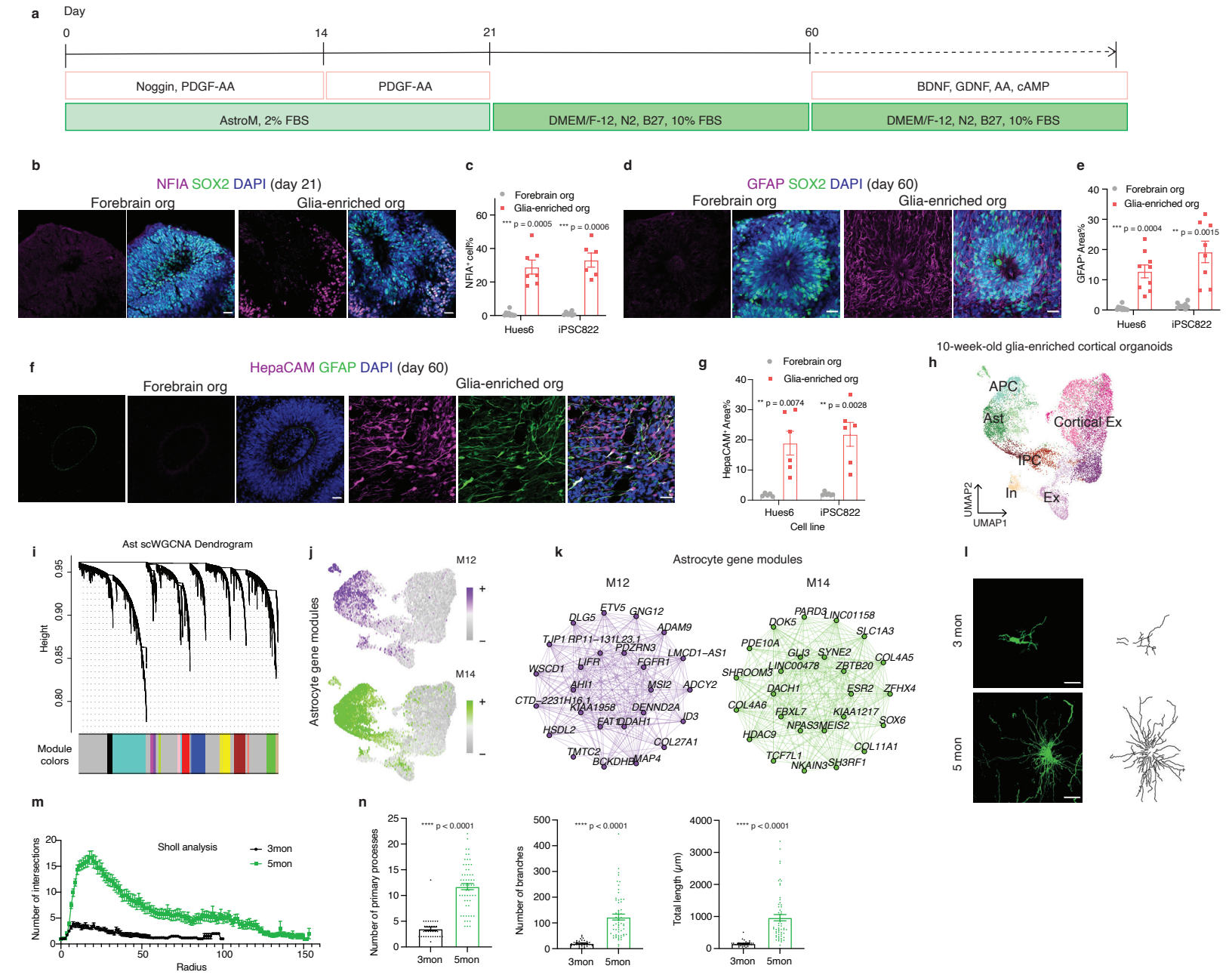
a
Day
0
14
21
60
Noggin, PDGF-AA
PDGF-AA
BDNF, GDNF, AA, cAMP
AstroM, 2% FBS
DMEM/F-12, N2, B27, 10% FBS
DMEM/F-12, N2, B27, 10% FBS
b
NFIA SOX2 DAPI (day 21)
Forebrain org
Glia-enriched org
c
Forebrain org
Glia-enriched org
*** p = 0.0005
*** p = 0.0006
NFIA+ cell%
Hues6
iPSC822
d
GFAP SOX2 DAPI (day 60)
Forebrain org
Glia-enriched org
e
Forebrain org
Glia-enriched org
*** p = 0.0004
** p = 0.0015
GFAP+ Area%
Hues6
iPSC822
f
HepaCAM GFAP DAPI (day 60)
Forebrain org
Glia-enriched org
g
Forebrain org
Glia-enriched org
** p = 0.0074
** p = 0.0028
HepaCAM+ Area%
Hues6
iPSC822
Cell line
10-week-old glia-enriched cortical organoids
h
APC
Ast
Cortical Ex
IPC
In
Ex
UMAP2
UMAP1
i
Ast scWGCNA Dendrogram
Height
Module colors
j
M12
M14
Astrocyte gene modules
k
Astrocyte gene modules
M12
M14
ETV5
GNG12
DLG5
ADAM9
TJP1
RP11-131L23.1
PDZRN3
LMCD1-AS1
LIFR
FGFR1
WSCD1
AHI1
MSI2
ADCY2
CTD-2231H16.1
KIAA1958
DENND2A
FAT1
DDAH1
ID3
HSDL2
COL27A1
TMTC2
BCKDHB
MAP4
PARD3
LINC01158
DOK5
SLC1A3
PDE10A
GLI3
SYNE2
COL4A5
LINC00478
ZBTB20
SHROOM3
DACH1
ESR2
ZFHX4
COL4A6
FBXL7
KIAA1217
NPAS3
MEIS2
SOX6
HDAC9
COL11A1
TCF7L1
NKAIN3
SH3RF1
l
3 mon
5 mon
m
Sholl analysis
3mon
5mon
Number of intersections
Radius
n
**** p < 0.0001
Number of primary processes
Number of branches
Total length (μm)
3mon
5mon

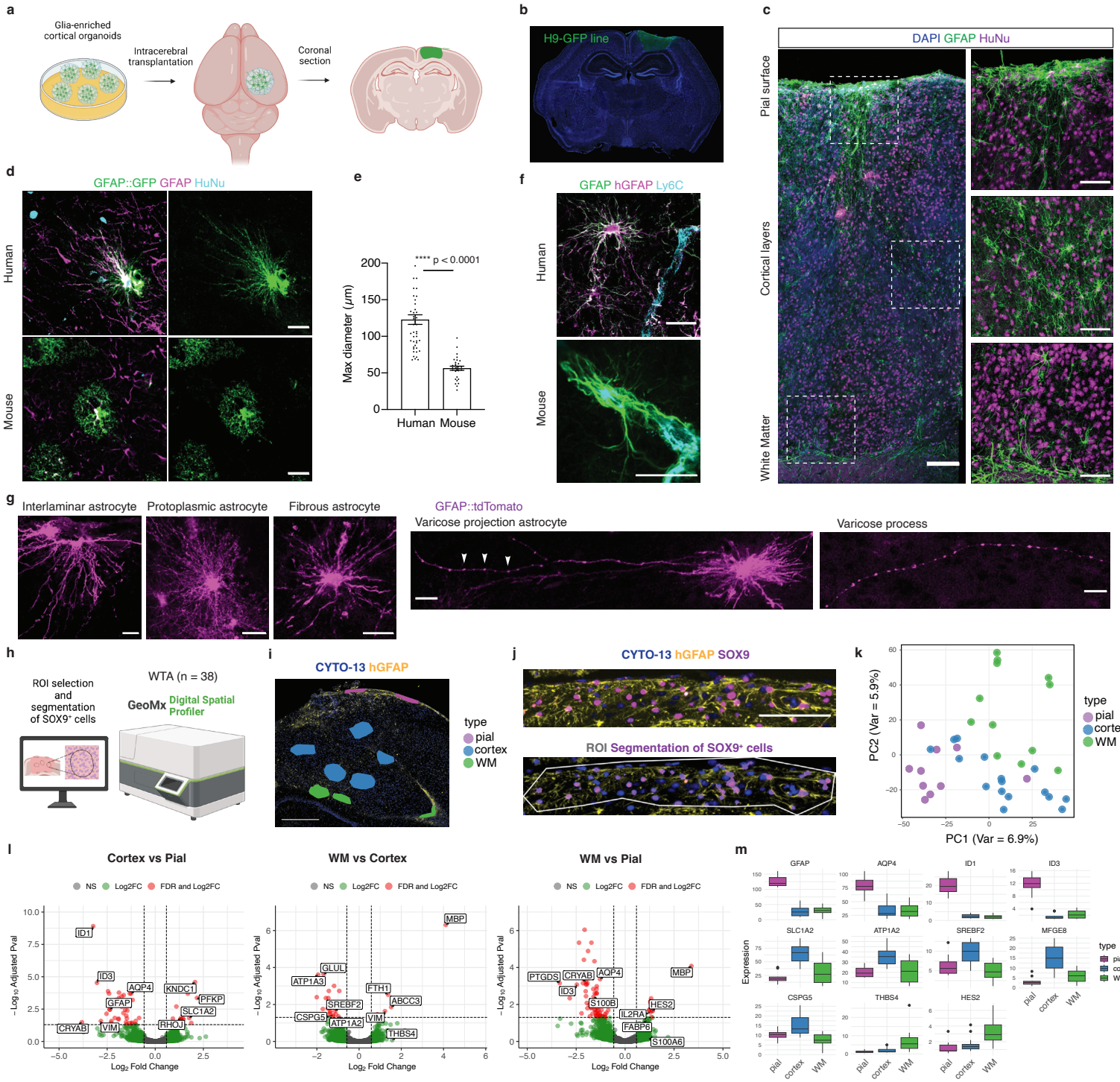
a
Glia-enriched cortical organoids
Intracerebral transplantation
Coronal section
b
H9-GFP line
c
DAPI GFAP HuNu
Pial surface
Cortical layers
White Matter
d
GFAP::GFP GFAP HuNu
Human
Mouse
e
**** p < 0.0001
Max diameter (μm)
200
150
100
50
0
Human Mouse
f
GFAP hGFAP Ly6C
Human
Mouse
g
Interlaminar astrocyte
Protoplasmic astrocyte
Fibrous astrocyte
GFAP::tdTomato
Varicose projection astrocyte
Varicose process
h
ROI selection and segmentation of SOX9⁺ cells
WTA (n = 38)
GeoMx Digital Spatial Profiler
i
CYTO-13 hGFAP
type
pial
cortex
WM
j
CYTO-13 hGFAP SOX9
ROI Segmentation of SOX9⁺ cells
k
PC2 (Var = 5.9%)
PC1 (Var = 6.9%)
type
pial
cortex
WM
l
Cortex vs Pial
WM vs Cortex
WM vs Pial
NS
Log2FC
FDR and Log2FC
−Log10 Adjusted Pval
Log2 Fold Change
ID1
ID3
AQP4
KNDC1
GFAP
PFKP
SLC1A2
CRYAB
VIM
RHOJ
MBP
GLUL
ATP1A3
FTH1
ABCC3
SREBF2
CSPG5
ATP1A2
THBS4
PTGDS
S100B
HES2
IL2RA
FABP6
S100A6
m
GFAP
AQP4
ID1
ID3
SLC1A2
ATP1A2
SREBF2
MFGE8
CSPG5
THBS4
HES2
Expression
pial
cortex
WM
type
pial
cortex
WM

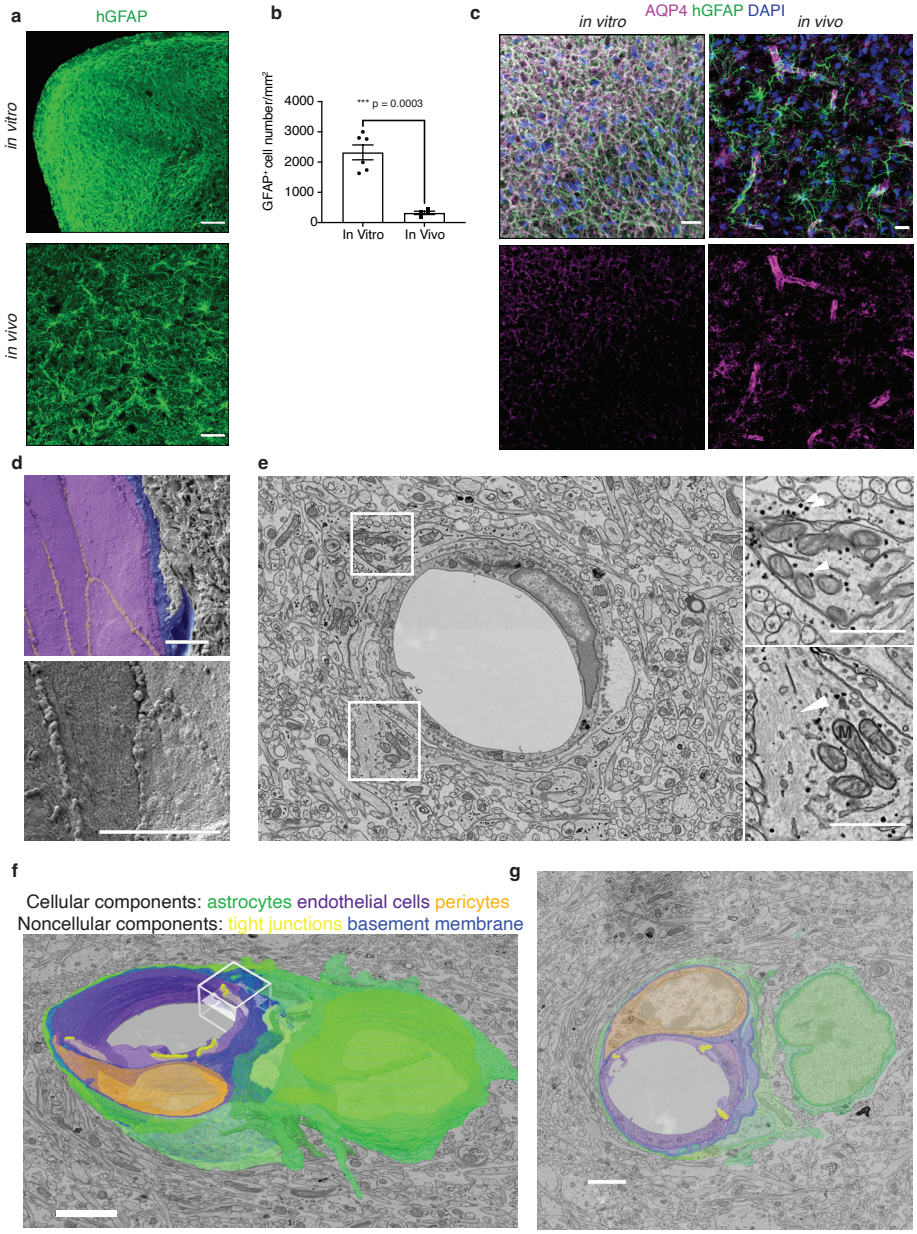
a
hGFAP
in vitro
in vivo
b
GFAP+ cell number/mm2
4000
3000
2000
1000
0
*** p = 0.0003
In Vitro
In Vivo
c
in vitro
AQP4 hGFAP DAPI
in vivo
d
e
M
f
Cellular components: astrocytes endothelial cells pericytes
Noncellular components: tight junctions basement membrane
g

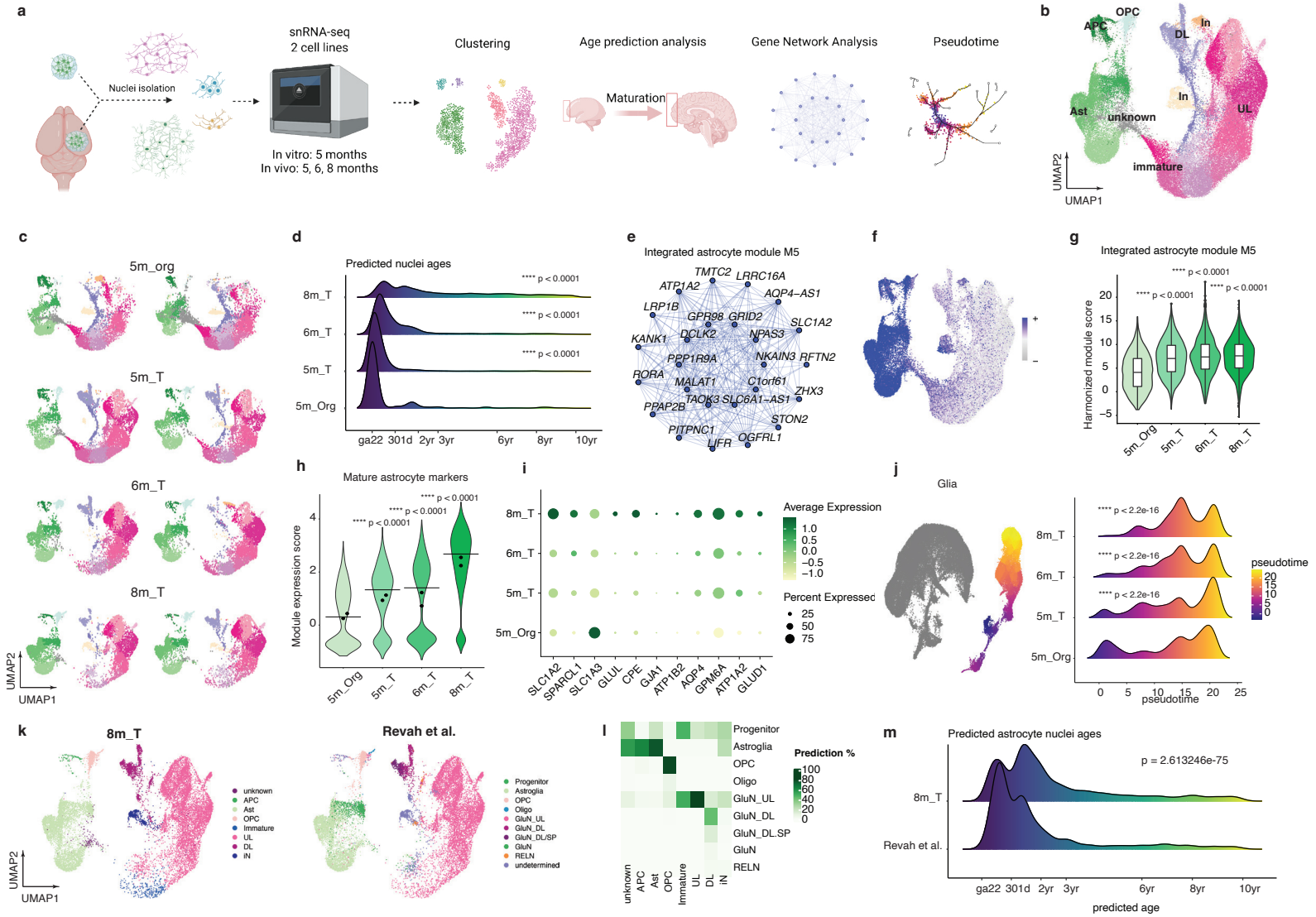
a
Nuclei isolation
snRNA-seq
2 cell lines
In vitro: 5 months
In vivo: 5, 6, 8 months
Clustering
Age prediction analysis
Maturation
Gene Network Analysis
Pseudotime
b
OPC
APC
In
DL
Ast
unknown
In
UL
immature
UMAP2
UMAP1
c
5m_org
5m_T
6m_T
8m_T
UMAP2
UMAP1
d
Predicted nuclei ages
8m_T
6m_T
5m_T
5m_Org
**** p < 0.0001
ga22 301d 2yr 3yr 6yr 8yr 10yr
e
Integrated astrocyte module M5
TMTC2
LRRC16A
ATP1A2
AQP4−AS1
LRP1B
GPR98
GRID2
SLC1A2
KANK1
DCLK2
NPAS3
PPP1R9A
NKAIN3
RFTN2
RORA
MALAT1
C1orf61
ZHX3
TAOK3
SLC6A1−AS1
PPAP2B
STON2
PITPNC1
OGFRL1
LIFR
f
+
−
g
Integrated astrocyte module M5
**** p < 0.0001
Harmonized module score
5m_Org
5m_T
6m_T
8m_T
h
Mature astrocyte markers
Module expression score
**** p < 0.0001
5m_Org
5m_T
6m_T
8m_T
i
Average Expression
1.0
0.5
0.0
−0.5
−1.0
Percent Expressed
25
50
75
8m_T
6m_T
5m_T
5m_Org
SLC1A2
SPARCL1
SLC1A3
GLUL
CPE
GJA1
ATP1B2
AQP4
GPM6A
ATP1A2
GLUD1
j
Glia
**** p < 2.2e-16
8m_T
6m_T
5m_T
5m_Org
pseudotime
k
8m_T
unknown
APC
Ast
OPC
Immature
UL
DL
iN
UMAP2
UMAP1
Revah et al.
Progenitor
Astroglia
OPC
Oligo
GluN_UL
GluN_DL
GluN_DL/SP
GluN
RELN
undetermined
l
Progenitor
Astroglia
OPC
Oligo
GluN_UL
GluN_DL
GluN_DL.SP
GluN
RELN
unknown
APC
Ast
OPC
Immature
UL
DL
iN
Prediction %
100
80
60
40
20
0
m
Predicted astrocyte nuclei ages
p = 2.613246e-75
8m_T
Revah et al.
ga22 301d 2yr 3yr 6yr 8yr 10yr
predicted age

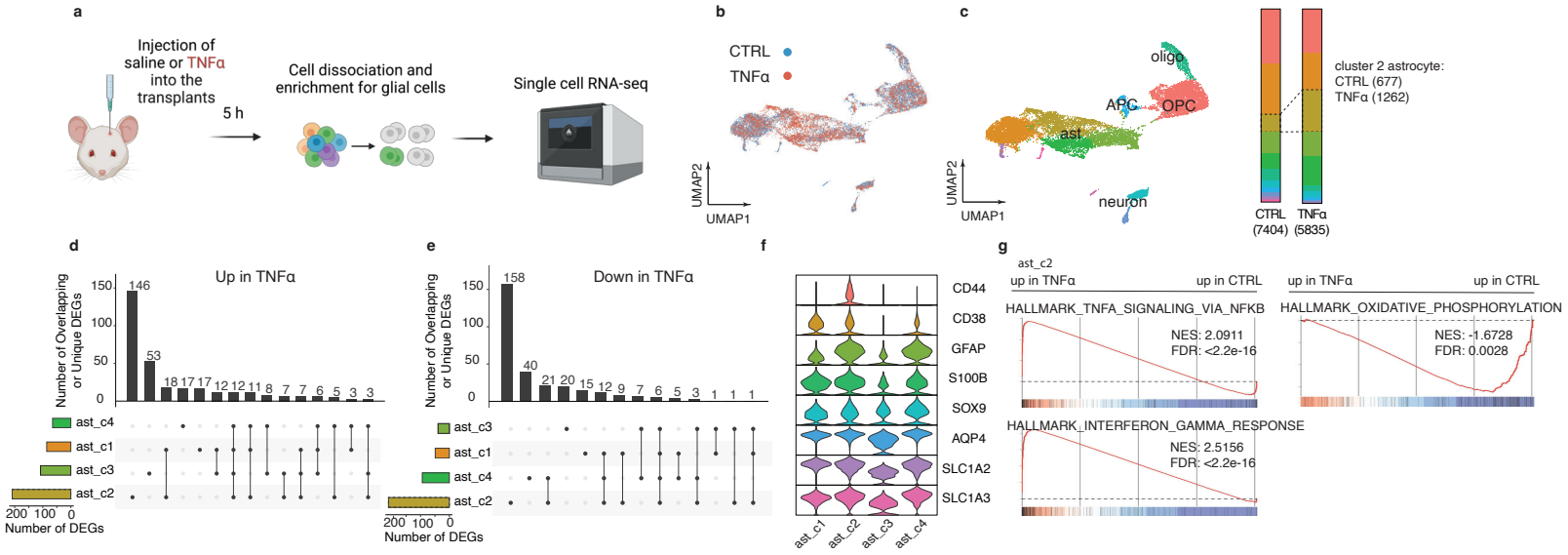
a
Injection of saline or TNFα into the transplants
5 h
Cell dissociation and enrichment for glial cells
Single cell RNA-seq
b
CTRL
TNFα
UMAP2
UMAP1
c
oligo
APC
OPC
ast
neuron
UMAP2
UMAP1
cluster 2 astrocyte:
CTRL (677)
TNFα (1262)
CTRL (7404)
TNFα (5835)
d
Up in TNFα
Number of Overlapping or Unique DEGs
146
53
18 17 17 12 12 11 8 7 7 6 5 3 3
ast_c4
ast_c1
ast_c3
ast_c2
200 100 0
Number of DEGs
e
Down in TNFα
Number of Overlapping or Unique DEGs
158
40
21 20 15 12 9 7 6 5 3 1 1 1
ast_c3
ast_c1
ast_c4
ast_c2
200 100 0
Number of DEGs
f
CD44
CD38
GFAP
S100B
SOX9
AQP4
SLC1A2
SLC1A3
ast_c1
ast_c2
ast_c3
ast_c4
g
ast_c2
up in TNFα
up in CTRL
HALLMARK_TNFA_SIGNALING_VIA_NFKB
NES: 2.0911
FDR: <2.2e-16
up in TNFα
up in CTRL
HALLMARK_OXIDATIVE_PHOSPHORYLATION
NES: -1.6728
FDR: 0.0028
HALLMARK_INTERFERON_GAMMA_RESPONSE
NES: 2.5156
FDR: <2.2e-16

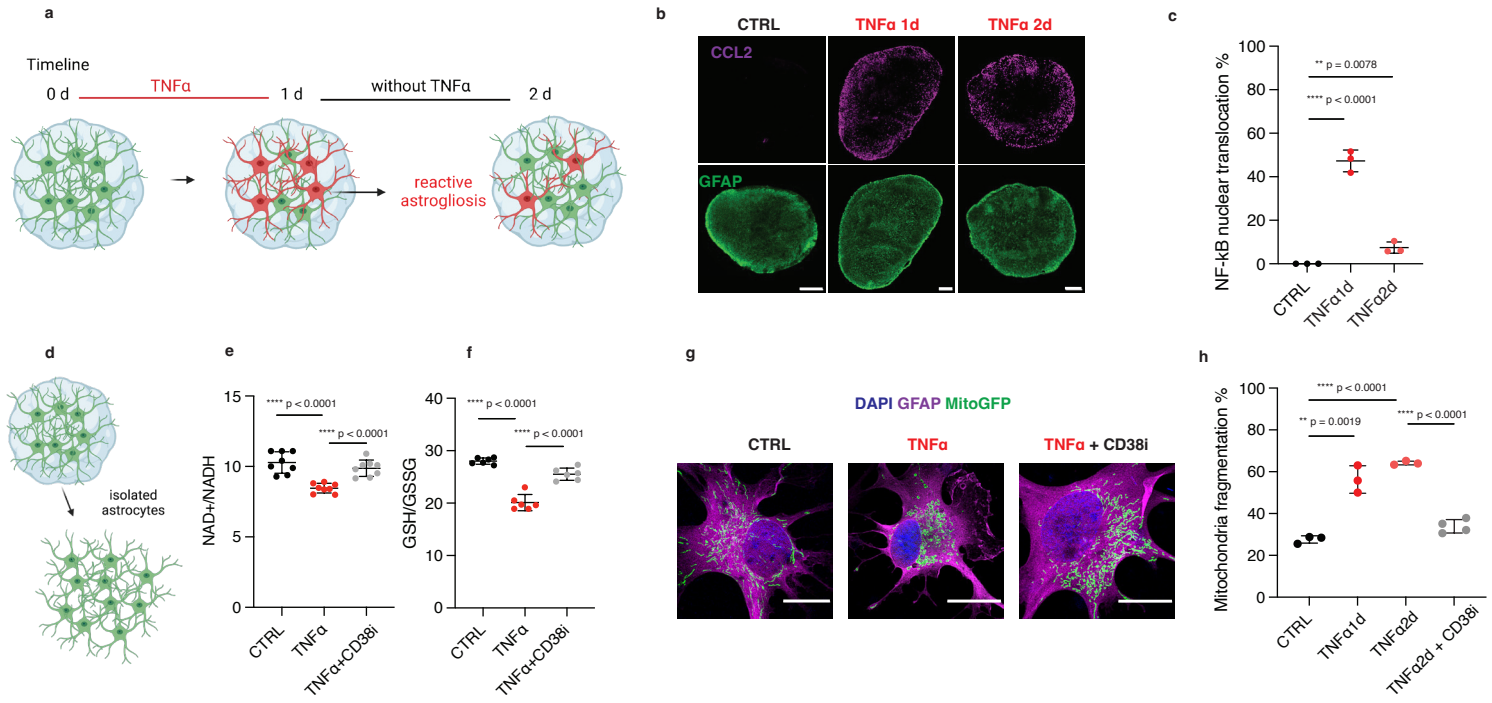
a
Timeline
0 d
TNFα
1 d
without TNFα
2 d
reactive astrogliosis
b
CTRL
TNFα 1d
TNFα 2d
CCL2
GFAP
c
NF-kB nuclear translocation %
** p = 0.0078
**** p < 0.0001
CTRL
TNFα1d
TNFα2d
d
isolated astrocytes
e
NAD+/NADH
**** p < 0.0001
**** p < 0.0001
CTRL
TNFα
TNFα+CD38i
f
GSH/GSSG
**** p < 0.0001
**** p < 0.0001
CTRL
TNFα
TNFα+CD38i
g
DAPI GFAP MitoGFP
CTRL
TNFα
TNFα + CD38i
h
Mitochondria fragmentation %
**** p < 0.0001
** p = 0.0019
**** p < 0.0001
CTRL
TNFα1d
TNFα2d
TNFα2d + CD38i

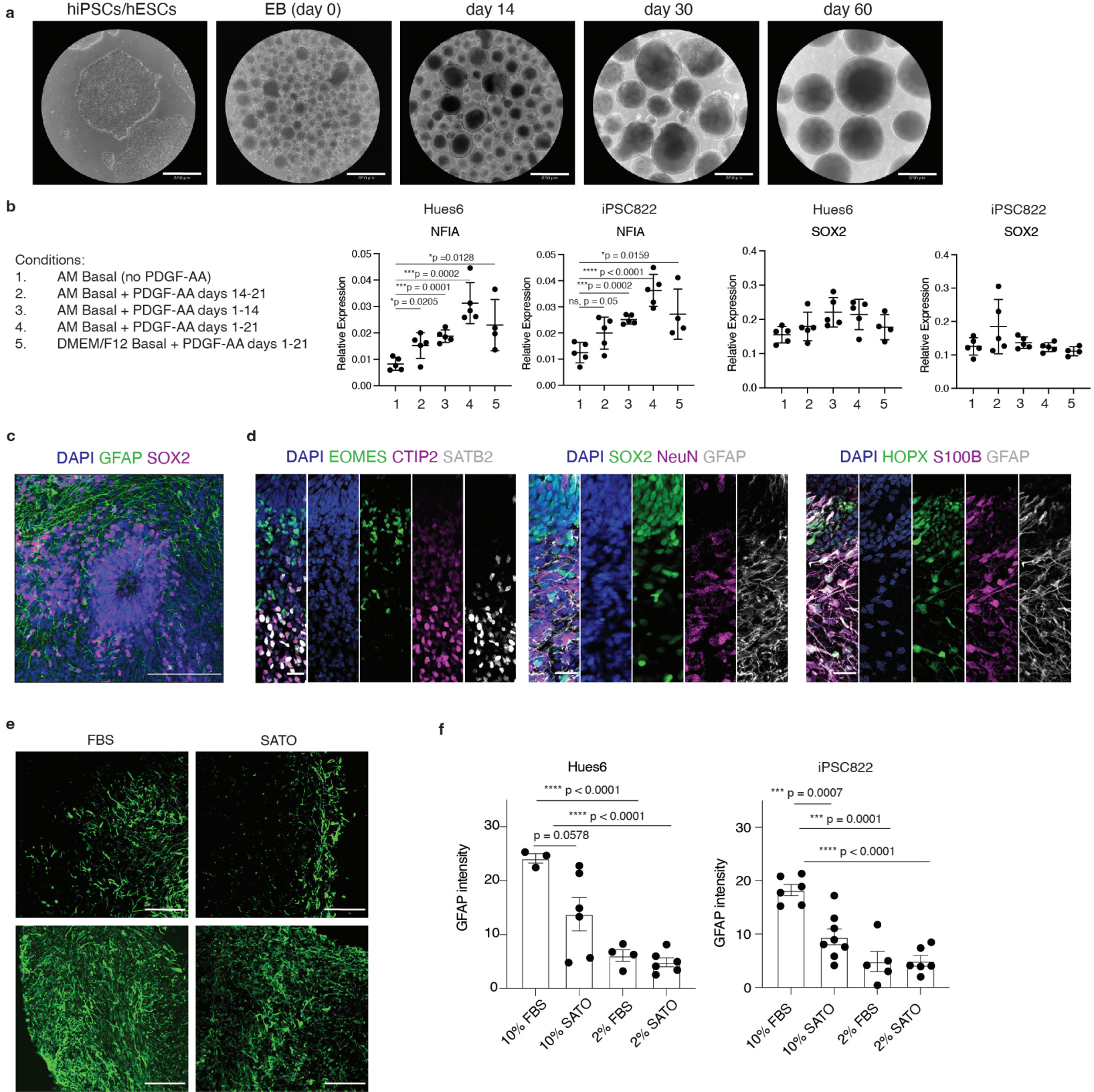
a
hiPSCs/hESCs
EB (day 0)
day 14
day 30
day 60
b
Conditions:
1. AM Basal (no PDGF-AA)
2. AM Basal + PDGF-AA days 14-21
3. AM Basal + PDGF-AA days 1-14
4. AM Basal + PDGF-AA days 1-21
5. DMEM/F12 Basal + PDGF-AA days 1-21
Hues6
NFIA
iPSC822
NFIA
Hues6
SOX2
iPSC822
SOX2
Relative Expression
*p =0.0128
***p = 0.0002
***p = 0.0001
*p = 0.0205
*p = 0.0159
**** p < 0.0001
***p = 0.0002
ns, p = 0.05
c
DAPI GFAP SOX2
d
DAPI EOMES CTIP2 SATB2
DAPI SOX2 NeuN GFAP
DAPI HOPX S100B GFAP
e
FBS
SATO
2%
10%
f
Hues6
iPSC822
GFAP intensity
**** p < 0.0001
**** p < 0.0001
p = 0.0578
*** p = 0.0007
*** p = 0.0001
**** p < 0.0001
10% FBS
10% SATO
2% FBS
2% SATO

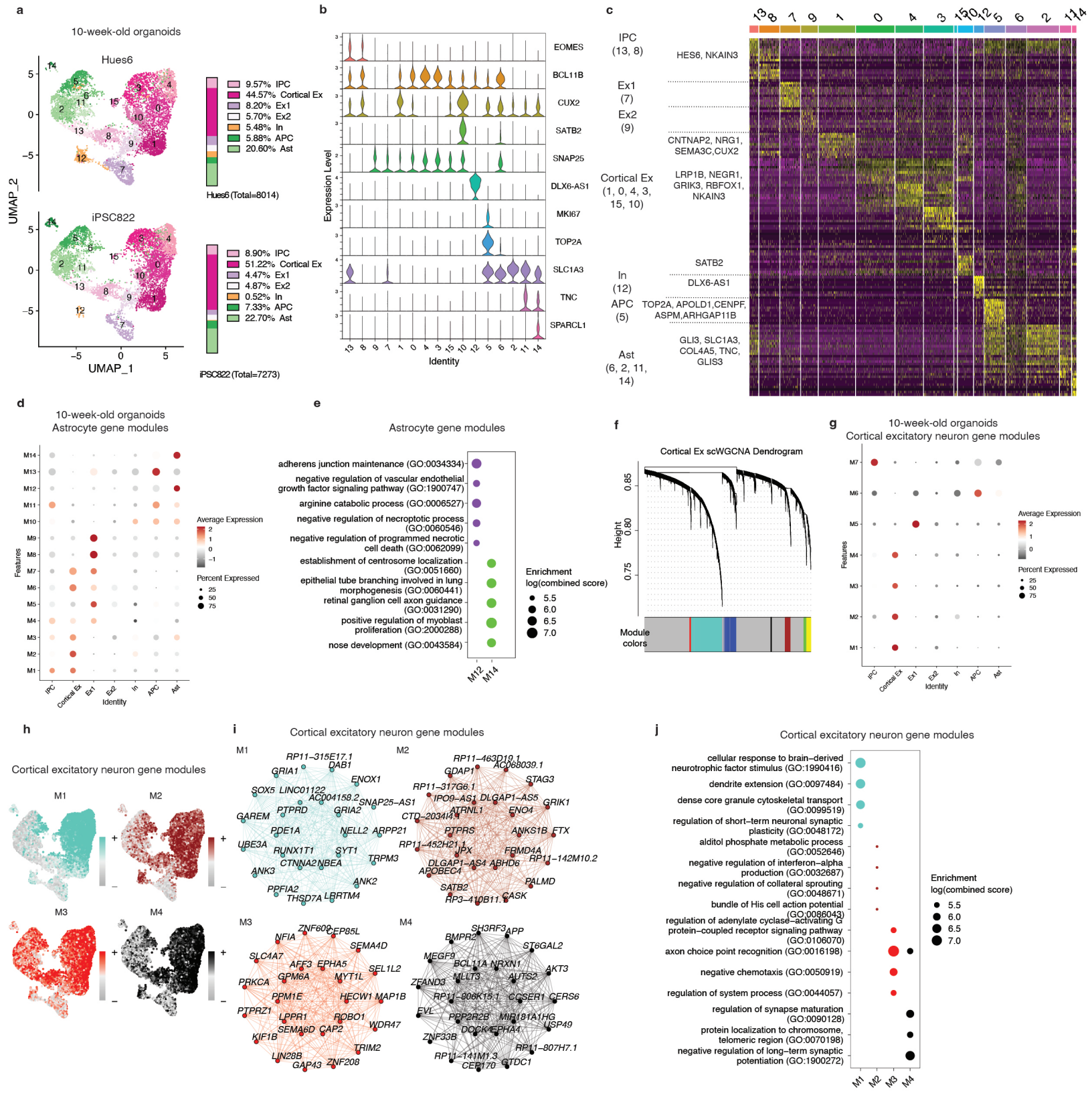
a
10-week-old organoids
Hues6
iPSC822
UMAP_1
UMAP_2
9.57% IPC
44.57% Cortical Ex
8.20% Ex1
5.70% Ex2
5.48% In
5.88% APC
20.60% Ast
Hues6 (Total=8014)
8.90% IPC
51.22% Cortical Ex
4.47% Ex1
4.87% Ex2
0.52% In
7.33% APC
22.70% Ast
iPSC822 (Total=7273)
b
EOMES
BCL11B
CUX2
SATB2
SNAP25
DLX6-AS1
MKI67
TOP2A
SLC1A3
TNC
SPARCL1
Expression Level
Identity
c
IPC (13, 8)
Ex1 (7)
Ex2 (9)
Cortical Ex (1, 0, 4, 3, 15, 10)
In (12)
APC (5)
Ast (6, 2, 11, 14)
HES6, NKAIN3
CNTNAP2, NRG1, SEMA3C,CUX2
LRP1B, NEGR1, GRIK3, RBFOX1, NKAIN3
SATB2
DLX6-AS1
TOP2A, APOLD1,CENPF, ASPM,ARHGAP11B
GLI3, SLC1A3, COL4A5, TNC, GLIS3
d
10-week-old organoids
Astrocyte gene modules
Average Expression
Percent Expressed
Features
Identity
e
Astrocyte gene modules
adherens junction maintenance (GO:0034334)
negative regulation of vascular endothelial growth factor signaling pathway (GO:1900747)
arginine catabolic process (GO:0006527)
negative regulation of necroptotic process (GO:0060546)
negative regulation of programmed necrotic cell death (GO:0062099)
establishment of centrosome localization (GO:0051660)
epithelial tube branching involved in lung morphogenesis (GO:0060441)
retinal ganglion cell axon guidance (GO:0031290)
positive regulation of myoblast proliferation (GO:2000288)
nose development (GO:0043584)
Enrichment log(combined score)
f
Cortical Ex scWGCNA Dendrogram
Height
Module colors
g
10-week-old organoids
Cortical excitatory neuron gene modules
Average Expression
Percent Expressed
Features
Identity
h
Cortical excitatory neuron gene modules
M1
M2
M3
M4
i
Cortical excitatory neuron gene modules
M1
M2
M3
M4
j
Cortical excitatory neuron gene modules
cellular response to brain-derived neurotrophic factor stimulus (GO:1990416)
dendrite extension (GO:0097484)
dense core granule cytoskeletal transport (GO:0099519)
regulation of short-term neuronal synaptic plasticity (GO:0048172)
alditol phosphate metabolic process (GO:0052646)
negative regulation of interferon-alpha production (GO:0032687)
negative regulation of collateral sprouting (GO:0048671)
bundle of His cell action potential (GO:0086043)
regulation of adenylate cyclase-activating G protein-coupled receptor signaling pathway (GO:0106070)
axon choice point recognition (GO:0016198)
negative chemotaxis (GO:0050919)
regulation of system process (GO:0044057)
regulation of synapse maturation (GO:0090128)
protein localization to chromosome, telomeric region (GO:0070198)
negative regulation of long-term synaptic potentiation (GO:1900272)
Enrichment log(combined score)

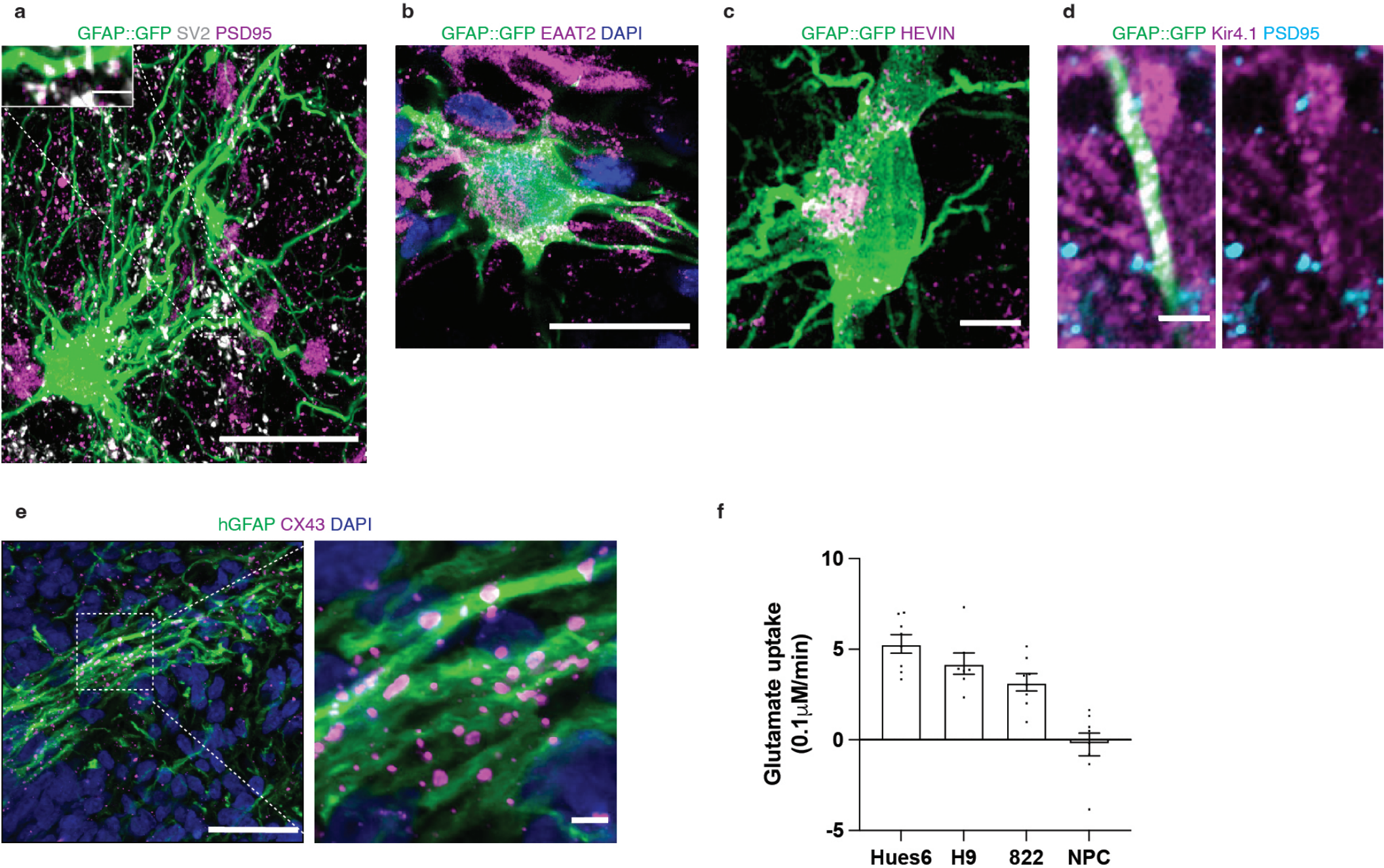
a
GFAP::GFP SV2 PSD95
b
GFAP::GFP EAAT2 DAPI
c
GFAP::GFP HEVIN
d
GFAP::GFP Kir4.1 PSD95
e
hGFAP CX43 DAPI
f
Glutamate uptake (0.1μM/min)
10
5
0
-5
Hues6
H9
822
NPC

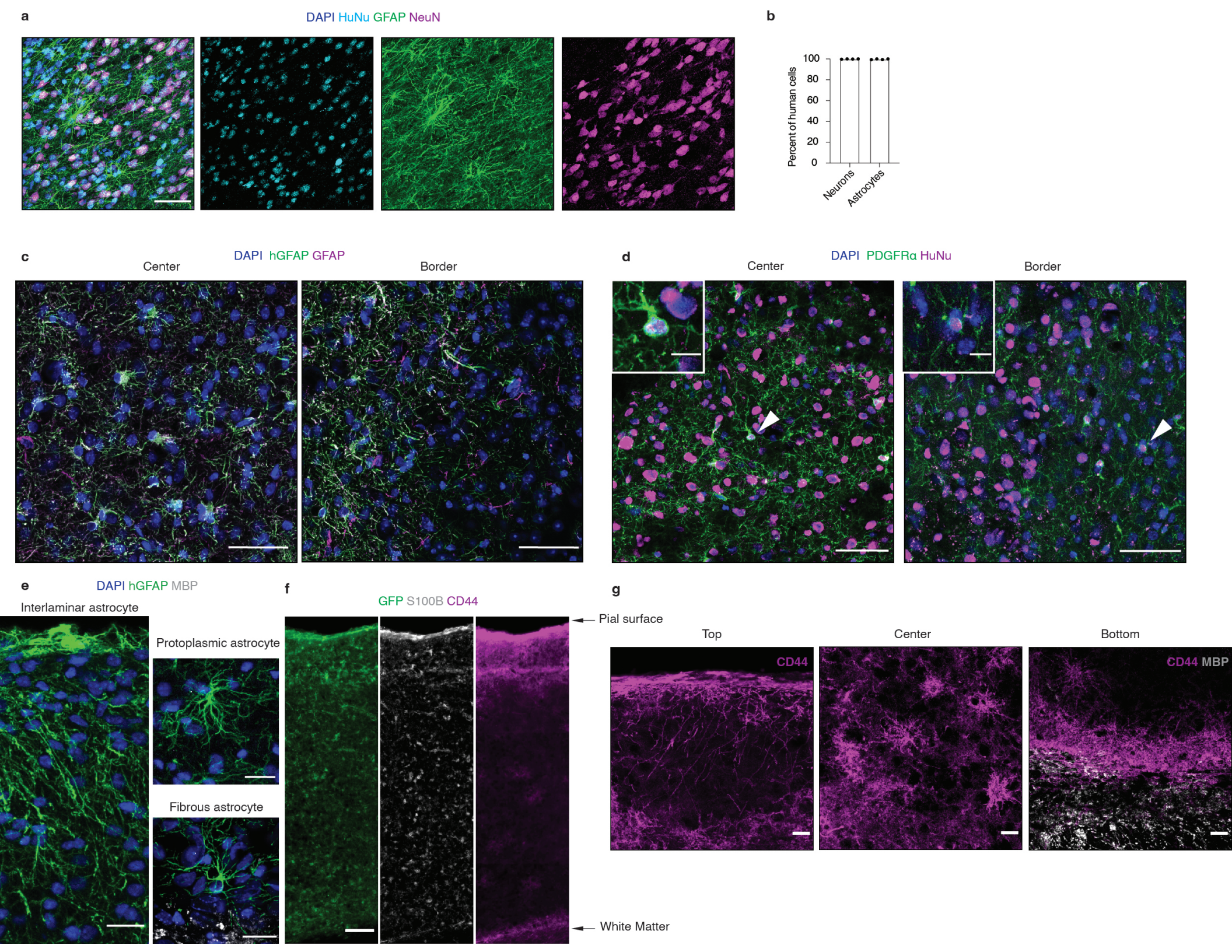
a
DAPI HuNu GFAP NeuN
b
Percent of human cells
100
80
60
40
20
0
Neurons
Astrocytes
c
DAPI hGFAP GFAP
Center
Border
d
DAPI PDGFRα HuNu
Center
Border
e
DAPI hGFAP MBP
Interlaminar astrocyte
Protoplasmic astrocyte
Fibrous astrocyte
f
GFP S100B CD44
Pial surface
White Matter
g
Top
Center
Bottom
CD44
CD44 MBP

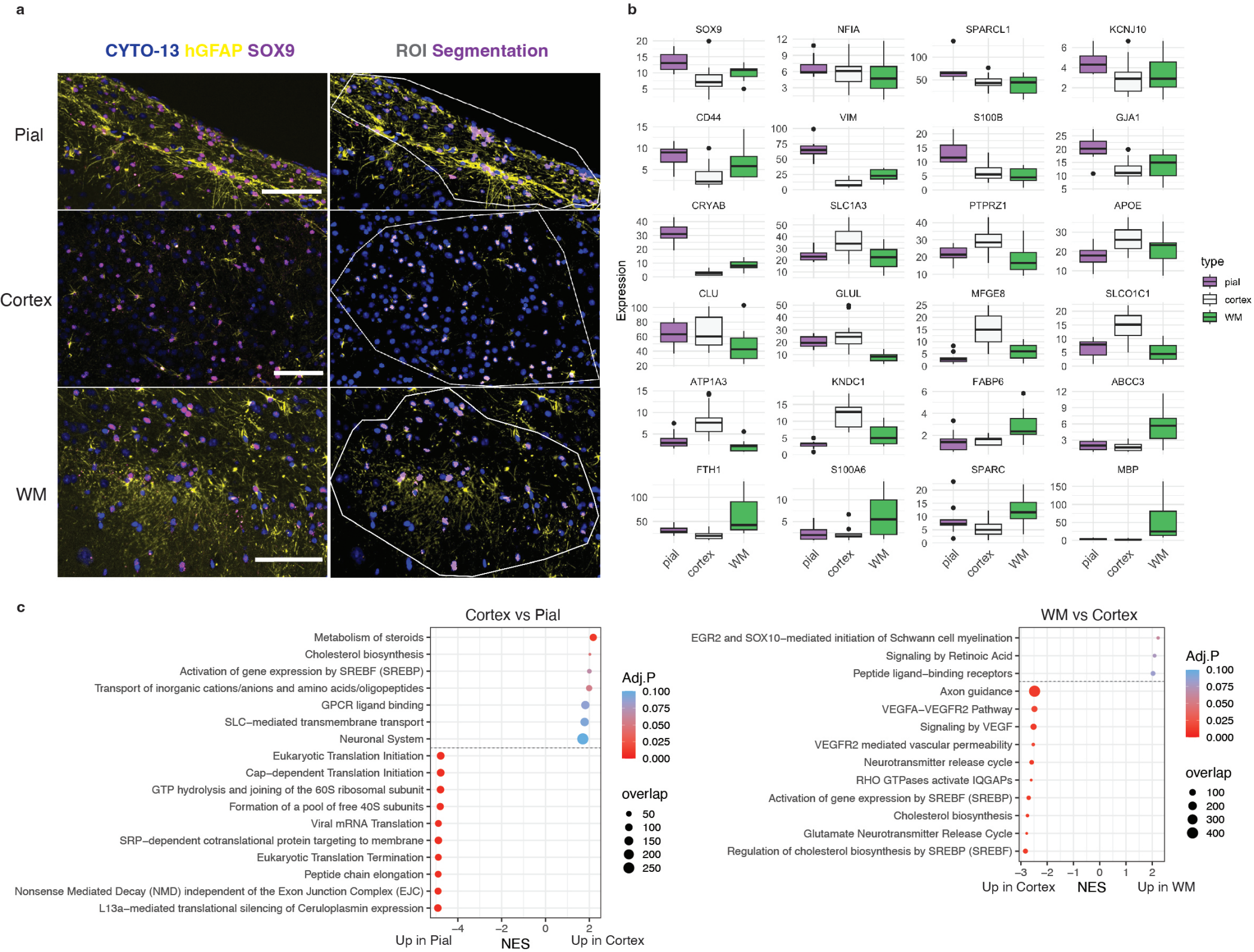
a
CYTO-13 hGFAP SOX9
ROI Segmentation
Pial
Cortex
WM
b
SOX9
NFIA
SPARCL1
KCNJ10
CD44
VIM
S100B
GJA1
CRYAB
SLC1A3
PTPRZ1
APOE
CLU
GLUL
MFGE8
SLCO1C1
ATP1A3
KNDC1
FABP6
ABCC3
FTH1
S100A6
SPARC
MBP
Expression
pial
cortex
WM
type
c
Cortex vs Pial
Metabolism of steroids
Cholesterol biosynthesis
Activation of gene expression by SREBF (SREBP)
Transport of inorganic cations/anions and amino acids/oligopeptides
GPCR ligand binding
SLC–mediated transmembrane transport
Neuronal System
Eukaryotic Translation Initiation
Cap–dependent Translation Initiation
GTP hydrolysis and joining of the 60S ribosomal subunit
Formation of a pool of free 40S subunits
Viral mRNA Translation
SRP–dependent cotranslational protein targeting to membrane
Eukaryotic Translation Termination
Peptide chain elongation
Nonsense Mediated Decay (NMD) independent of the Exon Junction Complex (EJC)
L13a–mediated translational silencing of Ceruloplasmin expression
Up in Pial
NES
Up in Cortex
Adj.P
overlap
WM vs Cortex
EGR2 and SOX10–mediated initiation of Schwann cell myelination
Signaling by Retinoic Acid
Peptide ligand–binding receptors
Axon guidance
VEGFA–VEGFR2 Pathway
Signaling by VEGF
VEGFR2 mediated vascular permeability
Neurotransmitter release cycle
RHO GTPases activate IQGAPs
Activation of gene expression by SREBF (SREBP)
Cholesterol biosynthesis
Glutamate Neurotransmitter Release Cycle
Regulation of cholesterol biosynthesis by SREBP (SREBP)
Up in Cortex
NES
Up in WM
Adj.P
overlap

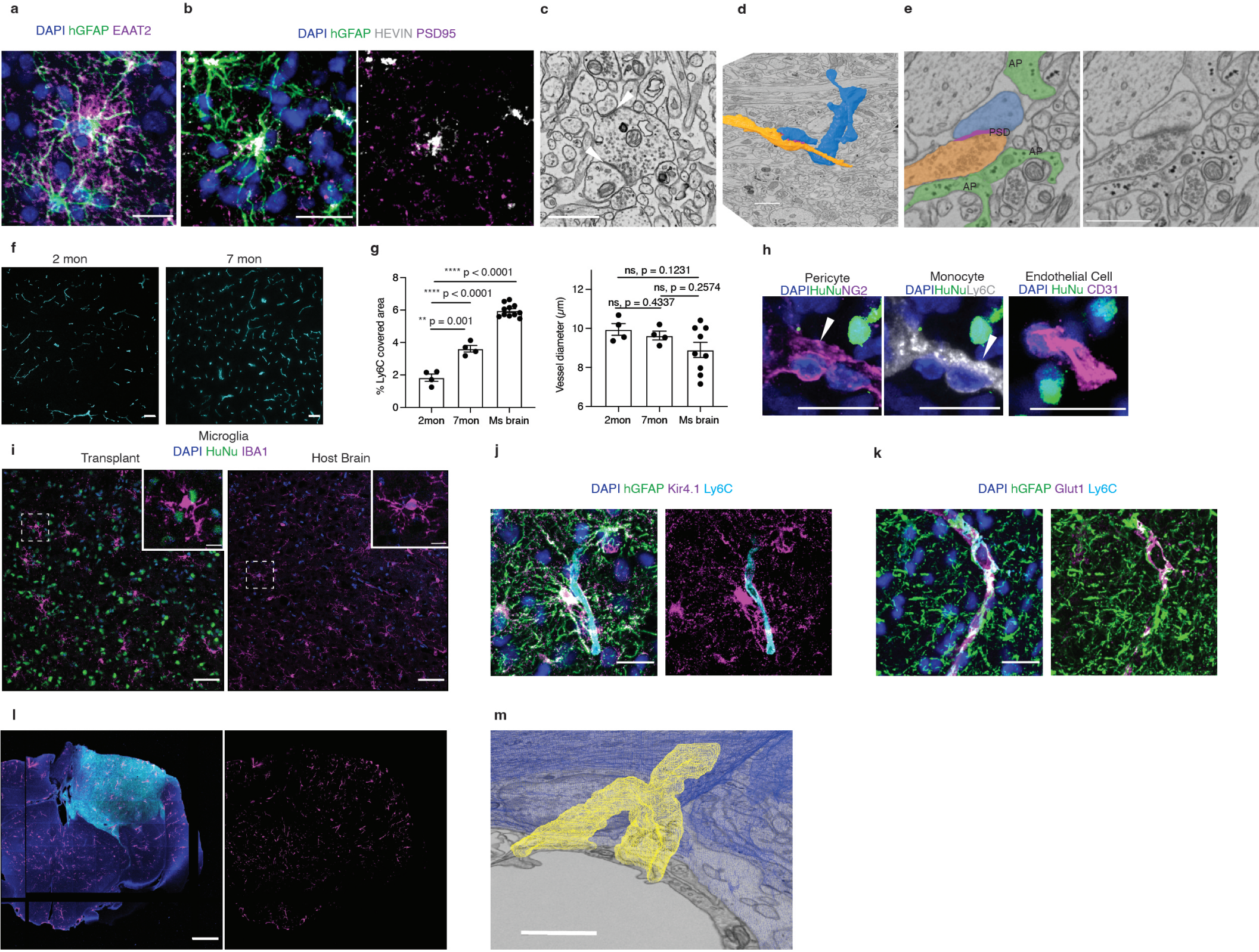
a
DAPI hGFAP EAAT2
b
DAPI hGFAP HEVIN PSD95
c
d
e
AP
PSD
AP
AP
f
2 mon
7 mon
g
% Ly6C covered area
**** p < 0.0001
**** p < 0.0001
** p = 0.001
2mon
7mon
Ms brain
Vessel diameter (μm)
ns, p = 0.1231
ns, p = 0.2574
ns, p = 0.4337
2mon
7mon
Ms brain
h
Pericyte
DAPIHuNuNG2
Monocyte
DAPIHuNuLy6C
Endothelial Cell
DAPI HuNu CD31
i
Transplant
Microglia
DAPI HuNu IBA1
Host Brain
j
DAPI hGFAP Kir4.1 Ly6C
k
DAPI hGFAP Glut1 Ly6C
l
m

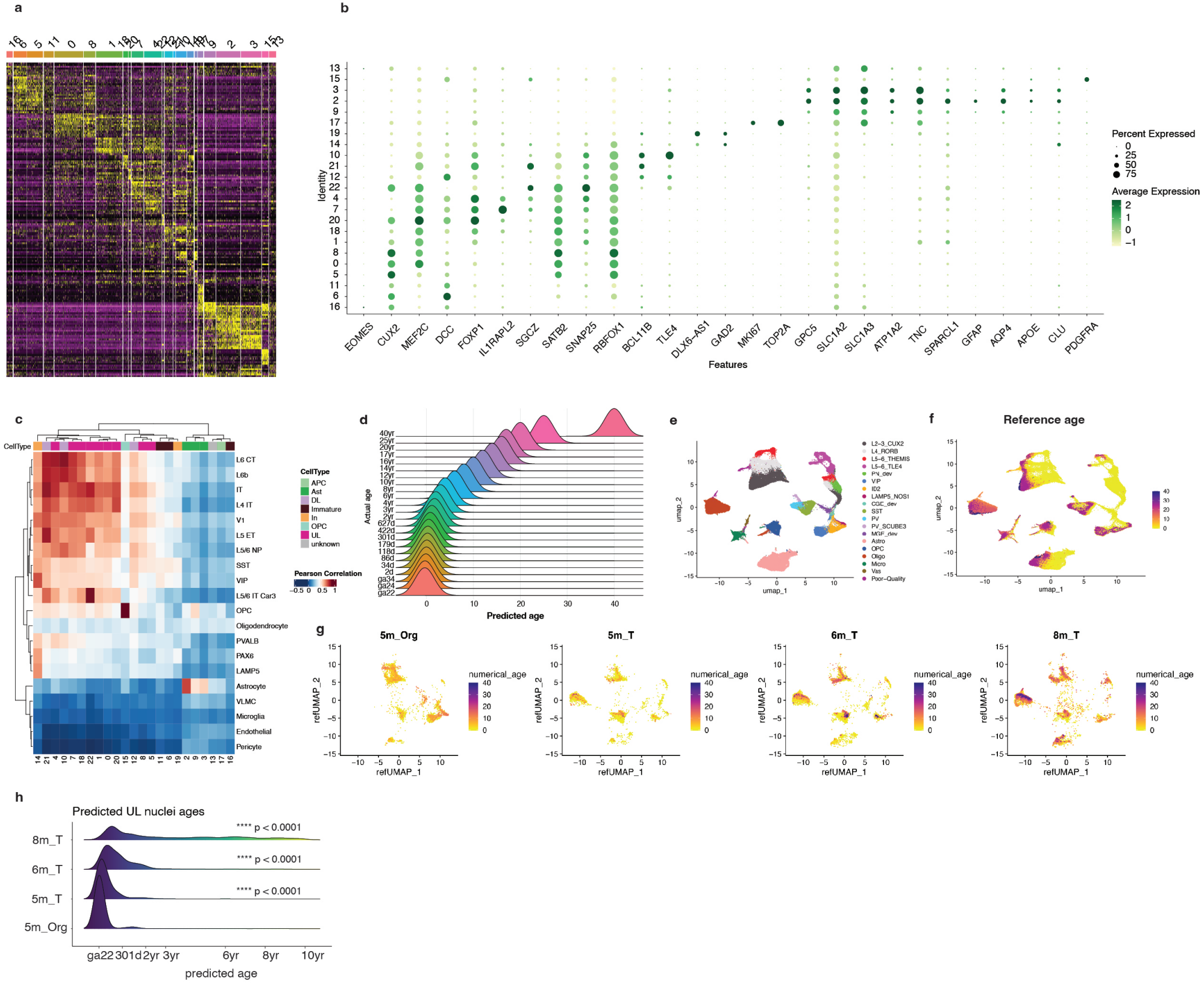
a
b
Identity
Features
EOMES
CUX2
MEF2C
DCC
FOXP1
IL1RAPL2
SGCZ
SATB2
SNAP25
RBFOX1
BCL11B
TLE4
DLX6-AS1
GAD2
MKI67
TOP2A
GPC5
SLC1A2
SLC1A3
ATP1A2
TNC
SPARCL1
GFAP
AQP4
APOE
CLU
PDGFRA
Percent Expressed
Average Expression
c
CellType
L6 CT
L6b
IT
L4 IT
V1
L5 ET
L5/6 NP
SST
VIP
L5/6 IT Car3
OPC
Oligodendrocyte
PVALB
PAX6
LAMP5
Astrocyte
VLMC
Microglia
Endothelial
Pericyte
Pearson Correlation
d
Actual age
Predicted age
e
umap_1
umap_2
f
Reference age
g
5m_Org
5m_T
6m_T
8m_T
refUMAP_1
refUMAP_2
numerical_age
h
Predicted UL nuclei ages
8m_T
6m_T
5m_T
5m_Org
**** p < 0.0001
predicted age

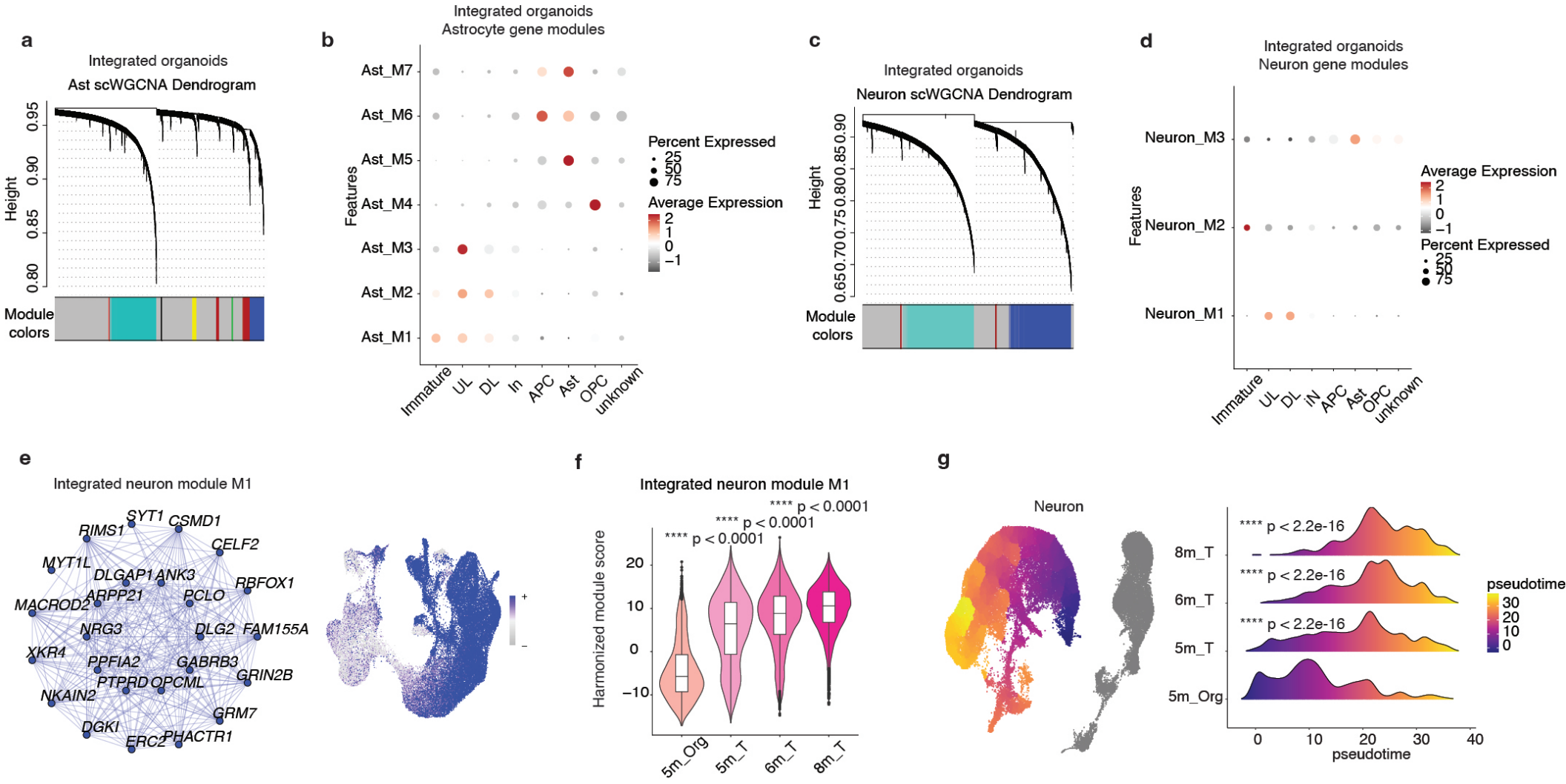
a
Integrated organoids
Ast scWGCNA Dendrogram
Height
0.95
0.90
0.85
0.80
Module colors
b
Integrated organoids
Astrocyte gene modules
Features
Ast_M7
Ast_M6
Ast_M5
Ast_M4
Ast_M3
Ast_M2
Ast_M1
Immature
UL
DL
In
APC
Ast
OPC
unknown
Percent Expressed
25
50
75
Average Expression
2
1
0
−1
c
Integrated organoids
Neuron scWGCNA Dendrogram
Height
0.90
0.85
0.80
0.75
0.70
0.65
Module colors
d
Integrated organoids
Neuron gene modules
Features
Neuron_M3
Neuron_M2
Neuron_M1
Immature
UL
DL
iN
APC
Ast
OPC
unknown
Average Expression
2
1
0
−1
Percent Expressed
25
50
75
e
Integrated neuron module M1
SYT1
CSMD1
RIMS1
CELF2
MYT1L
DLGAP1
ANK3
RBFOX1
ARPP21
PCLO
MACROD2
NRG3
DLG2
FAM155A
XKR4
PPFIA2
GABRB3
PTPRD
OPCML
GRIN2B
NKAIN2
GRM7
DGKI
ERC2
PHACTR1
f
Integrated neuron module M1
Harmonized module score
20
10
0
−10
**** p < 0.0001
**** p < 0.0001
**** p < 0.0001
5m_Org
5m_T
6m_T
8m_T
g
Neuron
8m_T
6m_T
5m_T
5m_Org
**** p < 2.2e-16
**** p < 2.2e-16
**** p < 2.2e-16
pseudotime
30
20
10
0
0
10
20
30
40
pseudotime

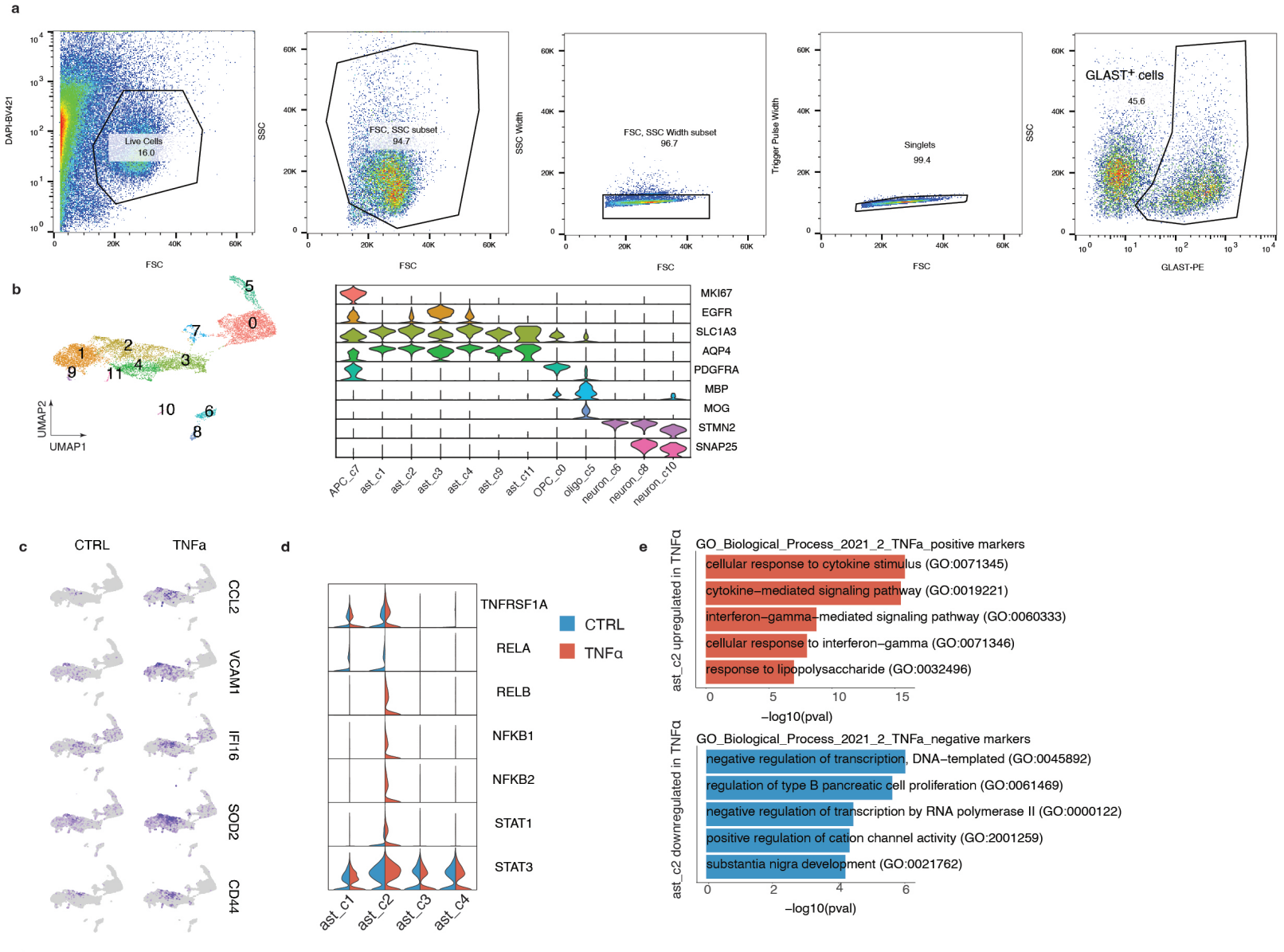
a
DAPI-BV421
SSC
Live Cells
16.0
FSC
FSC, SSC subset
94.7
SSC Width
FSC, SSC Width subset
96.7
Trigger Pulse Width
Singlets
99.4
GLAST+ cells
45.6
GLAST-PE
b
UMAP2
UMAP1
MKI67
EGFR
SLC1A3
AQP4
PDGFRA
MBP
MOG
STMN2
SNAP25
APC_c7
ast_c1
ast_c2
ast_c3
ast_c4
ast_c9
ast_c11
OPC_c0
oligo_c5
neuron_c6
neuron_c8
neuron_c10
c
CTRL
TNFa
CCL2
VCAM1
IFI16
SOD2
CD44
d
TNFRSF1A
RELA
RELB
NFKB1
NFKB2
STAT1
STAT3
CTRL
TNFα
ast_c1
ast_c2
ast_c3
ast_c4
e
GO_Biological_Process_2021_2_TNFa_positive markers
ast_c2 upregulated in TNFα
cellular response to cytokine stimulus (GO:0071345)
cytokine–mediated signaling pathway (GO:0019221)
interferon–gamma–mediated signaling pathway (GO:0060333)
cellular response to interferon–gamma (GO:0071346)
response to lipopolysaccharide (GO:0032496)
–log10(pval)
GO_Biological_Process_2021_2_TNFa_negative markers
ast_c2 downregulated in TNFα
negative regulation of transcription, DNA–templated (GO:0045892)
regulation of type B pancreatic cell proliferation (GO:0061469)
negative regulation of transcription by RNA polymerase II (GO:0000122)
positive regulation of cation channel activity (GO:2001259)
substantia nigra development (GO:0021762)
–log10(pval)
f
ast_c2
up in TNFα
up in CTRL
NADH dehydrogenase complex assembly
NES: -1.6021
FDR = 0.13
mitochondrial respiratory chain complex assembly
NES: -1.6157
FDR = 0.12

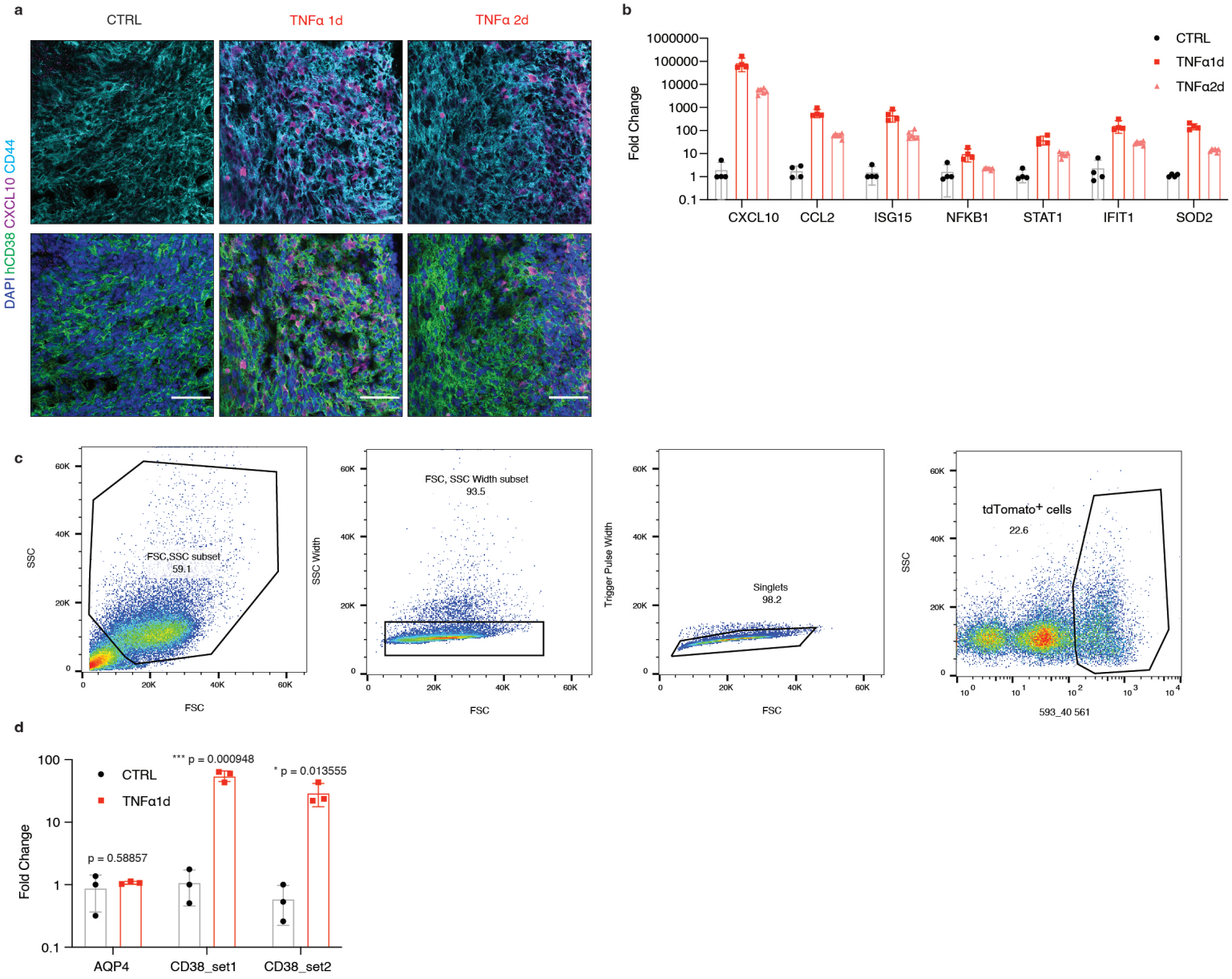
a
CTRL
TNFα 1d
TNFα 2d
DAPI hCD38 CXCL10 CD44
b
CTRL
TNFα1d
TNFα2d
Fold Change
1000000
100000
10000
1000
100
10
1
0.1
CXCL10
CCL2
ISG15
NFKB1
STAT1
IFIT1
SOD2
c
SSC
FSC
FSC,SSC subset
59.1
SSC Width
FSC, SSC Width subset
93.5
Trigger Pulse Width
Singlets
98.2
tdTomato+ cells
22.6
593_40 561
d
Fold Change
CTRL
TNFα1d
p = 0.58857
*** p = 0.000948
* p = 0.013555
AQP4
CD38_set1
CD38_set2